Design, Characterisation and Modelling of a High Current DC Arc Plasma Source for Silicon and Silicon Carbide Processing at Low Pressure

THÈSE N^{O} 4238 (2008)

PRÉSENTÉE LE 12 DÉCEMBRE 2008
À LA FACULTÉ SCIENCES DE BASE
CRPP ASSOCIATION EURATOM
PROGRAMME DOCTORAL EN PHYSIQUE

ÉCOLE POLYTECHNIQUE FÉDÉRALE DE LAUSANNE

POUR L'OBTENTION DU GRADE DE DOCTEUR ÈS SCIENCES

PAR

Lukas DERENDINGER

acceptée sur proposition du jury:

Prof. R. Schaller, président du jury
Dr C. Hollenstein, directeur de thèse
Dr U. Kroll, rapporteur
Prof. Ph. R. von Rohr, rapporteur
Prof. J. Winter, rapporteur

ÉCOLE POLYTECHNIQUE
FÉDÉRALE DE LAUSANNE
Suisse
2008

To my parents, Franz and Renata,
and my sister and brother, Anna and Benjamin.

Abstract

In the frame of this thesis, two similar high current DC arc (HCDCA) plasma sources were investigated in a low gas pressure regime (10^{-3}–10^{-2} mbar). One of them was initially designed for the epitaxial growth of silicon and silicon germanium (LEP), the other for the industrial deposition of diamond (BAI).

The LEP source was analysed using pure argon plasmas. Measurements of the ion saturation current were performed with a custom-built multi-Langmuir probe to analyse plasma density homogeneity. Plasma instabilities at 50 Hz were observed and studied by different means. One source of the instability is the AC current used for the filament heating, whereas lower frequency instabilities are due to the use of a ring shaped anode. A sensitive Hall sensor was used to measure the magnetic field induced by the discharge current. It was found that depending on the plasma parameters gas pressure and external magnetic field the current tends to attach at different points on the anode, leading to a complete loss of reactor symmetry. The installation of an additional cusp field around the reactor chamber lead to an increase of the overall homogeneity of the plasma density, but it could not resolve the problems of current attachment. In the following the ring anode was replaced by a point anode and the maximum external magnetic field strength was increased by a factor of ten.

With a novel multi-Hall probe the current density of the now columnar shaped plasma was measured, showing a strongly peaked current density profile, when an external magnetic field is applied. Together with ion saturation current measurements made with a Langmuir probe, the electron temperature inside the plasma column was estimated to be about 4 eV.

In earlier works made on the BAI reactor the high dissociation efficiency of the HCDCA plasma source has already been shown. Optical emission spectra were compared between RF plasmas, low pressure (1.5 mbar) HCDCA plasmas and our very low pressure (10^{-3}–10^{-2} mbar) HCDCA plasmas. The dominating species found in RF plasma spectra are molecular, the spectra of low pressure HCDCA plasmas are dominated by atomic species and the spectra of very low pressure HCDCA plasmas are dominated by ions, emphasising the high dissociation efficiency of this system.

Silane and Methane was used as precursor gases in the BAI reactor for the deposition of silicon carbide films. Promising high deposition rates up to 9 nm/s were found, but FTIR spectroscopy showed high hydrogen and oxygen concentrations in the porous films, making the not optimised deposited material useless for the application of wear-resistant coatings.

Microcrystalline hydrogenated silicon (μc-Si:H) is viewed as a cost- and energy-effective alternative to crystalline silicon for the production of solar cells. A detailed analysis of the deposition rate and the Raman crystallinity of μc-Si:H films deposited in the BAI reactor showed deposition rates up to 6.5 nm/s and a wide range of crystallinity from 0–80 %. Film thickness inhomogeneity in silicon solar cells has to be less than 5 %. To meet this standard a first substantial improvement was achieved with the installation of a linear gas injection along the plasma column. Tests on large surface glasses ($47 \times 37\,\mathrm{cm}^2$) revealed strong diffusive effects, which could be reproduced with a simple gas diffusion model. The model showed the necessity to reduce the dead volume around the plasma and to set the substrates as close as possible to the plasma column in order to minimise film thickness inhomogeneity due to diffusion. Deposition rate measurements made in these conditions assured the results of the model.

The development of a method to estimate the dissociation efficiency of the plasma by simple pressure measurements showed also an important increase of the silane dissociation from 75–92 % when the plasma is confined in a smaller volume. Therefore, compared to the reactor with a large dead volume, only a third of the initial silane is lost to the pumps.

KEYWORDS

high current DC arc discharge, current density measurements using the Hall effect,
plasma enhanced chemical vapor deposition of thin films, microcrystalline silicon,
photovoltaic solar cells

Version abrégée

Dans le cadre de ce travail de thèse, nous avons étudié le fonctionnement à très basse pression (10^{-3}–10^{-2} mbar) de deux types de sources plasma à arc à haut courant (HCDCA). La première de ces sources (LEP) était fondamentalement conçue pour la croissance épitaxiale de couches de silicium et de silicium-germanium, tandis que la seconde (BAI) était destinée aux procédés industriels de déposition de diamant.

Seuls des plasmas d'argon ont été produits pour l'étude du fonctionnement de la source LEP. L'analyse de l'uniformité de la densité plasma a été réalisée par le biais de mesures du courant de saturation ionique d'une multi-sonde de Langmuir spécialement développée à cet effet. Des instabilités plasma à 50 Hz ont été observées et étudiées par différents moyens. Une partie de ces instabilités prend son origine dans le courant alternatif (AC) utilisé pour le chauffage du filament de la source, tandis qu'une autre contribution à plus basse fréquence est due à la forme annulaire de l'anode. En utilisant une sonde de Hall pour mesurer le champ magnétique induit par le courant dans la décharge, nous avons montré que celui-ci s'attache à différents points de l'anode en fonction des paramètres plasma (pression et champ magnétique), de sorte que la symétrie du réacteur s'en trouve complètement brisée. L'addition d'un champ multipolaire autour de la chambre du réacteur permet d'augmenter l'uniformité globale de la densité plasma, sans pour autant résoudre le problème du point d'attachement du courant. Par la suite, l'anode annulaire à été remplacée par une anode en pointe et l'intensité du champ magnétique appliqué à été augmentée d'un facteur dix.

La densité de courant dans la colonne de plasma ainsi obtenue a été mesurée par l'intermédiaire d'une multi-sonde de Hall innovante, et est apparue comme étant fortement piquée sur l'axe de la décharge, en présence d'un champ magnétique. Par ailleurs, ces mesures ont permis, en combinaison avec celles du courant de saturation ionique, d'estimer à 4 eV la température électronique dans la colonne de plasma.

Des études antérieures portant sur le réacteur BAI ont déjà mis en évidence la grande efficacité de la source HCDCA en termes de taux de dissociation. Les spectres d'émission optique de plasmas RF, de plasmas HCDCA à basses pressions (1.5 mbar) et de plasmas HCDCA à très basses pressions (10^{-3}–10^{-2} mbar) ont été comparés. Si les espèces dominantes dans le cas des décharges RF sont moléculaires, les plasmas obtenus par la source HCDCA sont quant à eux dominés par les atomes, à basse pression, voire par les ions à très basse pression, ce qui met bien en évidence le grand pouvoir de dissociation de ces décharges.

Pour les dépôts de films de carbure de silicium dans le réacteur BAI nous avons utilisé en guise de précurseurs un mélange de méthane et de silane. Des taux de dépôt prometteurs de l'ordre de 9 nm/s ont été obtenus, mais les couches se sont révélées poreuses et leur analyse par spectroscopie infrarouge (FTIR) a mis en évidence de hautes concentrations en hydrogène et oxygène. Ainsi, le matériau déposé, sans optimisation, apparaît de faible intérêt pour les applications liées à la protection contre les attaques extérieures come la corrosion et l'usure.

Le silicium microcristallin hydrogéné (μc-Si:H) est considéré comme une alternative intéressante au silicium cristallin, tant du point de vue du coût que du rendement énergétique, pour la production de cellules solaires. Une étude détaillée des dépôts de μc-Si:H réalisés dans le réacteur BAI a été effectuée et des taux de dépôt de 6.5 nm/s ont été obtenus avec des cristallinités Raman variant de 0 à 80 %. La non-uniformité des dépôts, en termes d'épaisseur, dans les cellules solaires à base de silicium doit être inférieure à 5 %. Pour remplir cette exigence, une première amélioration a été obtenue par l'installation d'un système linéaire d'injection des précurseurs le long de la colonne de plasma. Des tests réalisés sur de larges substrats de verre ($47 \times 37\,\mathrm{cm}^2$) ont mis en évidence de forts effets imputables à des phénomènes diffusifs. Ces derniers ont pu être expliqués dans le cadre d'un modèle simple de diffusion des gaz. Il en découle que, pour diminuer les inhomogénéités de dépôt liées à la diffusion des espèces, le volume mort entourant le plasma doit être minimisé et les substrats doivent être positionnés au plus proche de la colonne de plasma. Les mesures de taux de dépôt obtenus sur des plaques de verre dans ces conditions confirment les prédictions du modèle.

L'impact de la réduction du volume mort autour de la décharge sur le taux de dissociation des espèces a également été observé par de simples mesures des variations de pression engendrées par la dissociation. Une augmentation de 75 à 92 % du taux de dissociation du silane a été observée quand la décharge est confinée dans un volume réduit, ramenant à 30 % le taux de silane directement perdu dans les pompes.

MOTS CLÉS

décharge à arc à haut courant continu, mesures de densité de courant utilisant l'effet de Hall, déposition de couches minces assistée par plasma, silicium microcristallin, cellule solaire photovoltaïque

Contents

Introduction

The use of plasmas for technical applications goes back to the 19th century. At this time scientists observed thin films on the glass tubes they used in different kinds of discharges, produced by the evaporation of the carbon electrodes. Edison was the first to patent a method for the deposition of gold films on cylinders used for his first phonographs invented in 1877 [1].

But what exactly is a plasma? A plasma is an ionised gas, with a certain proportion of free electrons and it is called the fourth state of matter. Plasmas are the dominating state in which matter exists in our universe. About 99 % of it is in the plasma state, namely in the stars and in the interstellar matter. However, on our planet earth plasmas are seldom found naturally, two examples are lightning and the aurora seen at the earths poles. The most common plasma on earth has served mankind over thousands of years to protect them, to warm them and to lead to technical progresses maybe as important as the wheel: fire.

To understand the three general properties of a plasma, one needs to know the notion of the Debye-length λ_D. The Debye-length is the distance over which the mobile charge carriers in the plasma (e.g. electrons) screen out electric fields. Therefore a charged conductor can only be seen by the plasma inside a sphere with radius $r = \lambda_\mathrm{D}$, the so-called Debye-sphere. λ_D is calculated as

$$\lambda_\mathrm{D} = \sqrt{\frac{\varepsilon_0\, k_\mathrm{B}\, T_\mathrm{e}}{n_\mathrm{e}\, e^2}},$$

with T_e the electron temperature in Kelvin and n_e the electron density in m^{-3}. For an ionised gas to be called a plasma, it has to fulfil the following three conditions:

1. The Debye-length is small compared to the dimension of the plasma
2. The number of particles in a Debye-sphere is high, so electrostatic interactions dominate over the processes of ordinary gas kinetics and the plasma shows collective behaviour
3. The collision frequency is low compared to the plasma frequency ω_p.

A counterexample is the low-temperature top part of a candle flame, where the electron density is too low to meet condition 1. A very rough classification of different kinds of plasmas are the thermalised and non-thermalised plasmas. In a thermalised plasma the electron temperature T_e and the ion temperature T_i are equal, whereas in a non-thermalised plasma $T_\mathrm{e} > T_\mathrm{i}$, typical for cold low pressure plasmas.

The first plasmas created by scientist were sparks in electrostatic machines developed in the 18th century, but they were unable to analyse the rapid process of these discharges. Only when the first batteries were invented by Volta in 1800, the research of stabilised plasma arcs could begin. For a more profound understanding of what plasmas really are, it took another hundred years until Thompson discovered the electron in 1897 and Bohr postulated the classical atom model in 1913. Langmuir was the first, in 1928, to use the term *plasma* for an ionised gas, composed of positive and rarely negative ions and free electrons [2]. Langmuir introduced this name because the properties reminded him of the blood plasma. The basis for that connection is unclear, either it was the similarity in carrying particles or it comes from the ancient Greek word ”plastos”, meaning ”formed” or ”moulded”, since the plasma usually moulded itself into the shape of the recipient [3].

Since the first technical application invented by Edison, a wide range of techniques to use plasmas in many different domains were developed: Thin film deposition in large area RF reactors [4] or by plasma spraying [5], material etching, ion implantation [1], micromachining with electrical discharges [6], power systems based on plasma thrusters [7] or even the treatment of hazardous waste [8]. Most of these techniques are used in the production of all sort of daily life articles: Microelectronic parts in consumer electronics and informatics (e.g. microchips, flat screen TV sets and digital cameras), solar cells, medical instruments, optical tools (e.g. glasses and lenses), textiles and many more.

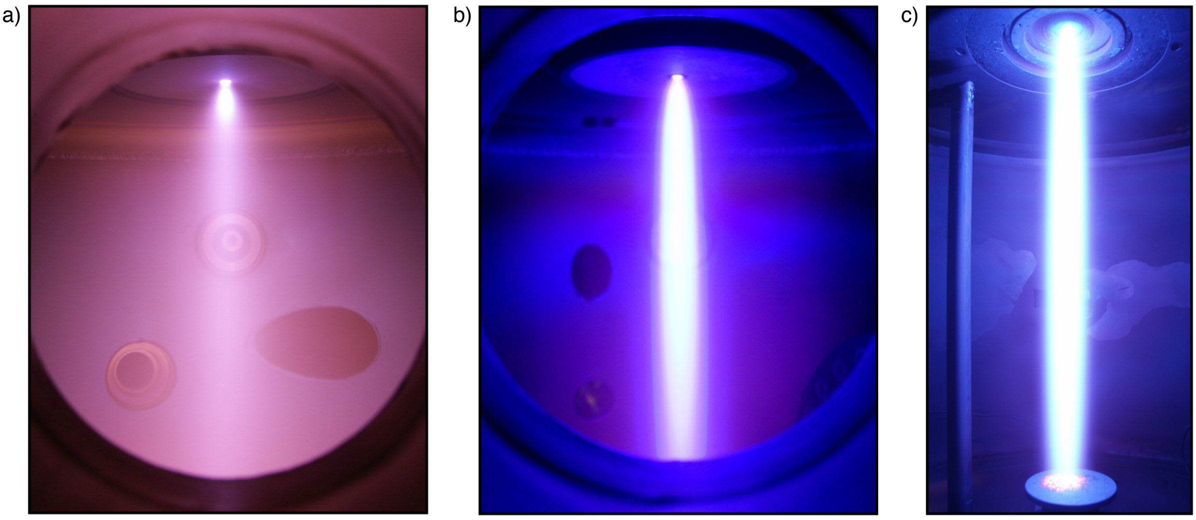

Figure 1: Argon plasmas in different configurations: a) Radical dominated plasma in the LEP reactor with a weak external magnetic field; b) Ion dominated plasma in the LEP reactor with a stronger magnetic field; c) Ion dominated plasma in the BAI reactor with a higher discharge current.

One possible way to produce a plasma is the high current DC arc (HCDCA) discharge. In figure 1 three different argon plasmas are shown, typically used for this thesis. The argon plasmas shown in a) and b) are found in the LEP reactor, whereas c) is found in the BAI reactor (cf. chapter 1). In contrast to generally invisible gases, plasmas emit light of characteristic wavelengths depending on the type of gas in use and induced by the recombination process of ions or the de-excitation of radicals. Plasma a) is radical dominated, whereas plasmas b) and c) are ion dominated, thus the change in colour.

In the next section the evolution of a HCDCA system and its various applications in the domain of plasma-enhanced chemical vapour deposition (PECVD) will be presented.

History of the reactor and its applications

In a HCDCA discharge the gas is ionised by fast electrons emitted by a heated filament. The filament is placed in an ionisation chamber, which is separated from the reactor by a plate with a small central hole. The electrons are accelerated in an electric field induced by a potential difference between the filament and an anode placed in the lower part of the reactor. Helmholtz coils produce a variable magnetic field in order to confine the fast electrons and therewith to increase the electron density inside the plasma column.

In 1992 M. Pedrazzini *et al.* [9], in collaboration with *Balzers AG* in Lichtenstein, started the first studies of a HCDCA reactor for the deposition of diamond as a wear-protection coating of cutting tools. They found that this type of non-thermalised plasmas, with a typical gas pressure of 1.5 mbar and a discharge current of 170 A, is a very efficient source of atomic hydrogen and therefore extremely well suited for diamond synthesis. A prototype of the so called BAI reactor is presented in figure 2a, showing mainly the vacuum chamber, the Helmholtz coils and on top, the ionisation source with the filament connections.

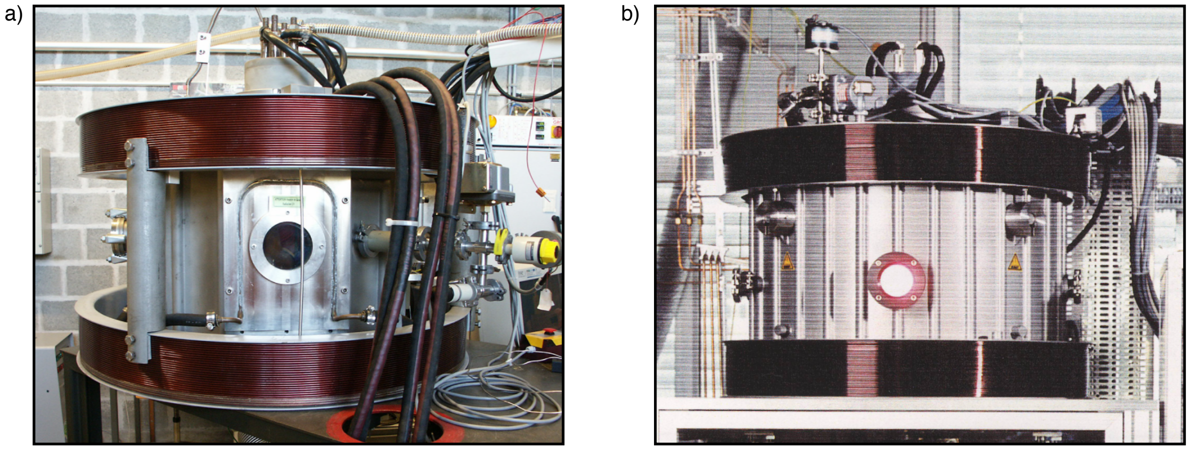

Figure 2: a) Prototype of the BAI reactor developed by M. Pedrazzini; b) BAI 730 D, the first industrial system produced by Balzers AG for the deposition of diamond coatings.

In 1997 Balzers AG introduced the first industrial diamond coating system (cf. figure 2b), depositing their patented BALINIT® DIAMOND hard layers. One of the major challenges in the development of a commercial system was the cooling of the chamber and of the conical anode. Therefore cooling water tubes are installed all around the vacuum chamber, as can be seen in figure 2b.

Already in 1995 the research was expanded to other types of wear-resistant coatings. D. Franz *et al.* [10] investigated the deposition process of boron nitride using the same prototype reactor as M. Pedrazzini. In the same work the capacity of the reactor for a deposition of μc-Si:H films was studied. A maximum deposition rate of 10 nm/s was found for a film containing 3–5 % of hydrogen. A further application of the HCDCA plasma was analysed by T. Delachaux [1], starting in 1999. For the watch industry the nitriding and carbiding of tetragonal zirconia was studied. The plasma treated zirconia changes its colour from white to either gold or silver, respectively by nitriding or carbiding of the ceramic. Together with a high scratching resistance this process was of high interest for the industry for the production of gold and silver imitating ceramic watch bracelets.

In 1998 the BAI system underwent a fundamental evolution, when it was used the first time at pressures two orders of magnitude lower and with a discharge on a circular anode. With this step, Rosenblad *et al.* [11] showed the first time the reactors potential of silicon germanium (SiGe) epitaxy by low energy plasma-enhanced chemical vapour deposition (LEPECVD). In 2000 Unaxis, the parent company of Balzers, started the development project LEPP 300 (low energy plasma processing) for the epitaxial deposition of silicon and silicon germanium on 300 mm wafers and in 2004 the collaboration with the CRPP for a detailed study of the LEP system started. Figure 3a shows the LEP reactor installed at CRPP, used in the framework of this thesis for pure argon plasma analysis. In figure 3b the laboratory version of the BAI 730 D is shown, used for the deposition of silicon and silicon carbide films.

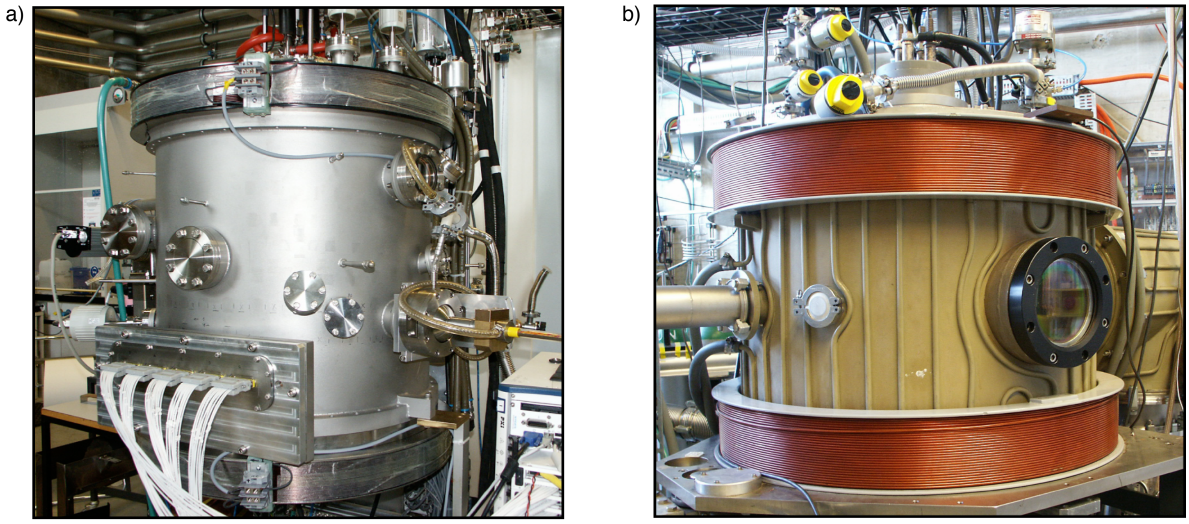

Figure 3: a) Industrial LEP reactor adapted for laboratory use; b) Laboratory version of the BAI 730 D reactor.

Purpose and structure of this thesis

In this thesis the results of investigations on a HCDCA plasma in a low pressure (10^{-2} mbar) regime and the characterisation of silicon and silicon carbide films are presented.

The first part of the work presented in this thesis was performed in collaboration with Unaxis Semiconductors and partially funded by CTI (Commission of Technique and

Innovation) project n° 6816.1. It was concerned about the better understanding of the low energy plasma, used for epitaxial growth of silicon layers. The second part of the work was performed as a mandate of Oerlikon Solar to investigate the deposition process for microcrystalline silicon films. A further study was made for Oerlikon Balzers on silicon carbide films for wear-resistant coatings.

The thesis has the following structure: In chapter 1 the two different plasma reactors used for this work are presented. Chapter 2 introduces the diagnostics used for plasma observation and film characterisation, whereof two were custom-built for this work: A multi-Langmuir probe and a multi-Hall probe. In chapter 3 the problems with instabilities and non-uniformities in the LEP reactor containing a circular anode are discussed. The solution was to take a step back and install a conical anode and larger Helmholtz coils, comparable to the older BAI reactor. The properties of the columnar plasmas found in the modified LEP reactor as well as in the BAI reactor are presented in chapter 4. Finally the characterisation of the deposition process in the BAI reactor and the resulting Si and SiC films are presented in chapter 5, before concluding this work.

Chapter 1

The HCDCA reactors

In this chapter two different *High Current DC Arc* reactor systems are presented: The *Balzers BAI 730 D* coating system and the *LEPECVD*[1] *module*. Both were adapted for laboratory use and underwent several important changes during the studies. The BAI system was originally used for diamond coatings. The LEP module was part of a cluster with up to six modules either used for high-rate deposition or for low temperature pre-epi cleaning in a hydrogen plasma [12]. It was originally used for epitaxial film growth and was produced by *OC Oerlikon* (Former Unaxis). For experimental studies the LEP module has been set up to work independently of the cluster system.

1.1 The LEP module

Rosenblad et al. [11, 13, 14, 15] have shown that the low energy plasma (LEP) technique can be used for epitaxy of strained Si and SiGe. This process, dissociating SiH_4 and GeH_4 in a high current DC arc plasma and depositing Si or SiGe layers aligned with an underlying substrate, is of great importance for the semiconductor industry as it provides high quality films for microelectronic devices.

The 300 mm single wafer module is shown schematically in figure 1.1. It consists of a double-wall (3) water cooled all metal-sealed ultra high vacuum (UHV) process chamber which is pumped by a dry pumping system (4). The inner dimensions of the chamber are $r = 29\,\text{cm}$ and $h = 56.5\,\text{cm}$. A slit valve connects the module with a loadlock (8). In industrial use the wafers are transferred from the loadlock to substrate pins and a susceptor lifts the wafer into process position (7) with the help of a lift mechanism (9). For the studies presented here no depositions were made on wafers and therefore the complete lift mechanism was not installed.

An ionisation source is attached to the top of the chamber, containing a tantalum or tungsten filament (1) heated by 150 A AC current. The source is separated from the reactor by a separation plate containing in its center a 2 mm diameter hole for the current passage. A DC power source generates a low voltage high current DC discharge (5) of typically 50–70 A and a voltage of 20–30 V (cf. figure 1.2). The module is called *Low*

---

[1] Low Energy Plasma-Enhanced Chemical Vapour Deposition

Energy Plasma module because the energy of the ions produced in this discharge can be low as 15 eV, a necessary condition for successful epitaxial growth. The gas used is argon, which is fed directly into the ionisation source. To initiate the discharge, the filament is heated and a voltage between filament and anode (6) is applied. The plasma is confined by two magnetic coils (2) in a near Helmholtz configuration.

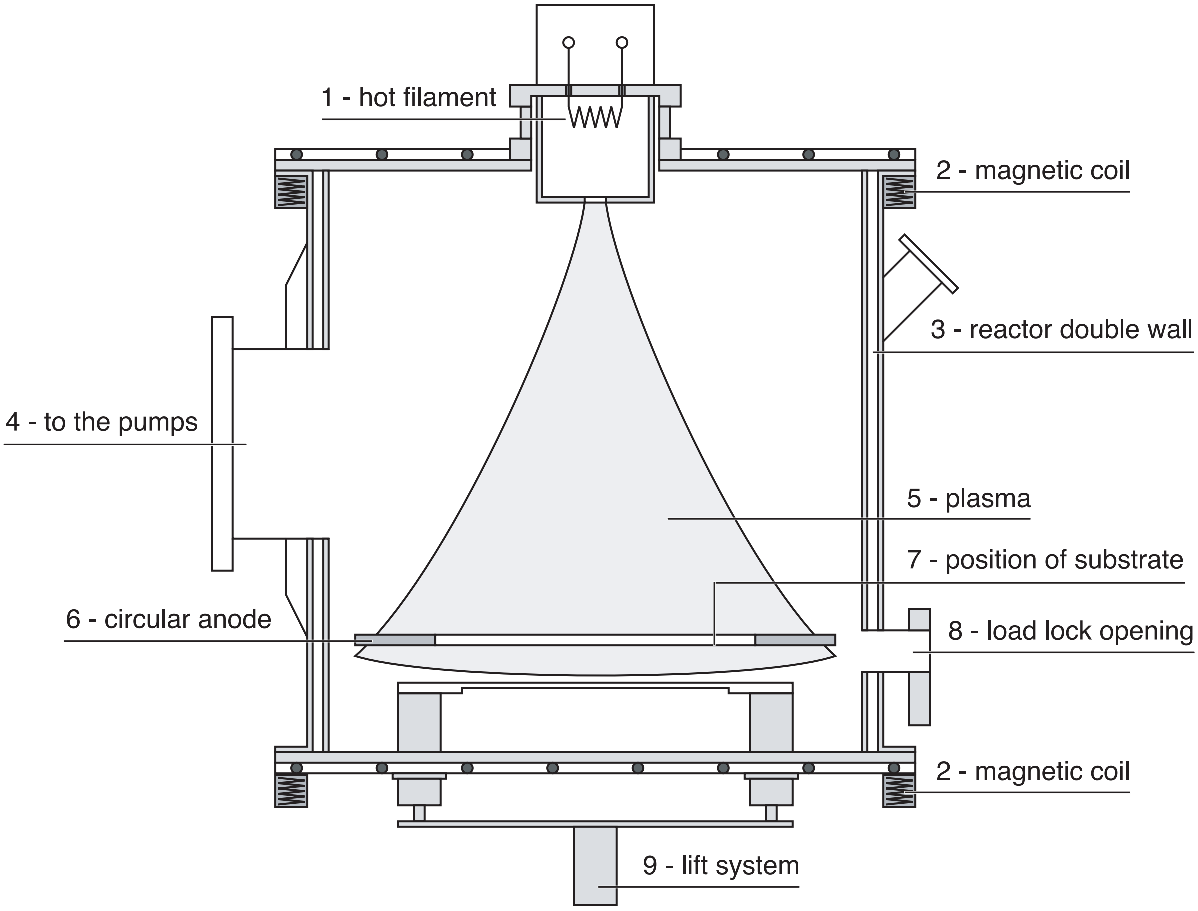

Figure 1.1: Schematic view of the LEP module used for the plasma studies

Ionisation source and plasma sources

The ionisation source consists of a small cylindrical box made of graphite, with a radius of $r = 8.5\,\mathrm{cm}$ and a height of $h = 16\,\mathrm{cm}$. Three electrical vacuum feedthroughs are installed in the top cover for the electrical connection of two tantalum or tungsten heating filaments. The thermionic production of fast electrons used for the ignition of the plasma arc is typically achieved with an AC heating current of 150 A in the filament and an applied voltage V_{fil} of about 10 V. This heating current is obtained from a transformer connected to the mains circuit with 400 V AC voltage. The DC plasma source is a Fronius DPS 400, connected to the anode (+) and the center of one of the transformer coils (−). The applied DC voltage accelerates the electrons towards the anode, ionising the gas in the module chamber. The complete electrical circuit of the LEP module is given in figure 1.2.

As the distance between anode and filament is about 60 cm, it can be difficult to ignite the plasma only with the applied DC voltage. Therefore a 22 Ω resistance can be connected to the electron source for plasma ignition support. It acts as a temporary second anode, closer to the filament, and is disconnected again after the ignition took place.

Once the plasma is stable the current in the filament could be stopped, but filament lifetime consideration has shown that it is strongly favourable to maintain a current in the filament, since the point attachment of the plasma current on the filament could lead to a melting of the filament.

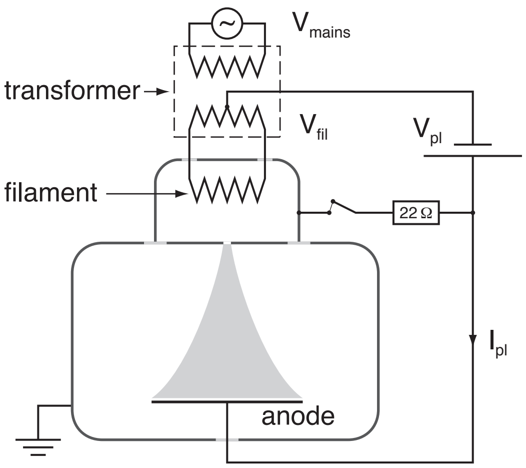

Figure 1.2: Electrical circuit of the LEP module power sources connections. The filament is connected via a transformer to an AC source. The DC plasma discharge is driven by a DC source connected to the anode and to the center of one of the transformer coils. The 22 Ω resistance supports the plasma ignition.

Pumping system

A dry pumping system (Edwards iH600) pumps down the process module via a bypass connection from atmosphere to a rough vacuum of 0.2 mbar. The iH600 pump has a gas ballast system which is suitable for use in harsh processes, such as PECVD.

A turbopump (type STP-A2203C) evacuates the vacuum chamber of the process module to UHV. This pump is also especially designed for harsh applications. The corrosion resistant pump has a nitrogen purge facility to minimise corrosive attack of the pump motor and sensor coils. In absence of leaks the base pressure obtained with the turbo pump is lower than 10^{-6} mbar.

Different magnetic fields used

The standard confining magnetic field coming from the Helmholtz coils (B_c) is measured as 5.4 G on the axis with the maximum current of 10 A applied. In industrial applications, in order to have the best homogeneity possible, the coils are not set to the maximum but the top coil is at 5 A and the bottom coil is not used at all. This leads to an axial field of less than 1 G above the substrate position.

Only in industry a second type of magnetic field is used: a dynamic field (B_w) produced by four compact solenoids or ”wobblers” with 3200 windings and an impedance of 15 Ohm. They are placed on the chamber side wall at every ninety degrees with their axes pointing horizontally to the reactor axis. By applying an oscillating current with a frequency of

4 Hz and an appropriate phase shift, a horizontal field rotating around the reactor axis is obtained. This field shifts the plasma towards the wall and forces the high density part of the plasma to wobble over the substrate. With this method a homogeneity in film thickness of less than 5 % was achieved.

Process configuration, laboratory version

In figure 1.3 the laboratory version of the *Low Energy Plasma Process* (LEPP) system is presented. It is a simplified version of the industrial LEPP 300 system. The complete LEPP 300 cluster consists of a transfer chamber with vacuum robot and, connected to the transfer chamber, two types of process modules: The LEPC module, for plasma-enhanced low temperature cleaning in a hydrogen atmosphere as preparation for the epitaxial growth, and the LEPECVD module for the deposition.

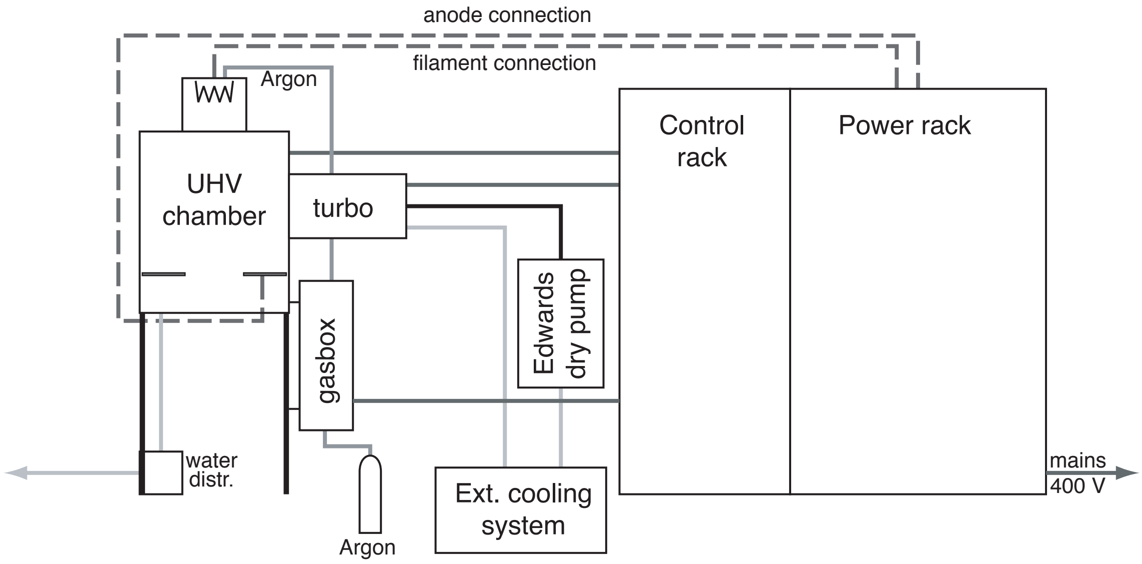

Figure 1.3: Schematic view of the modified reactor system for laboratory research.

The laboratory version consists of one UHV chamber, its dedicated pumping system, one control and one power rack, a gas line for argon and two water cooling systems. The power rack contains the DC current sources for the plasma current. In these *Fronius DPS 400* power supplies a low pass filter is installed to reduce the noise on the output (cf. chapter 3.1.1). After a detailed study on plasma instabilities the power supply has been exchanged by a high quality DC power supply from Hewlett-Packard (cf. chapter 3.1.2). The control rack is used for the miscellaneous controllers for the turbo pump or the pressure gauges and for the main control of the system via a custom control computer (SEAL S5703N).

Cooling water circuit

The complete system is cooled by two independent water cooling systems. A stand-alone air cooled system is responsible for the cooling of the dry pump system and the turbo pump. The in-house water cooling system, using deionised water, is used to cool the reactor chamber, the ionisation source, the electrical feedthrough of the circular anode and the complete conical point anode (cf. chapter 1.1.1).

Computer control system

The computer control system used originally by Unaxis was based on a proprietary software. It was built for industrial enduser necessities and controlled every single part of the system. This would have made it inflexible and unadapted for research use. Therefore an easy to handle SEAL S5703 control system was installed. It handles 16 analog input and 8 analog output channels as well as 16 digital in- and output channels. The programming is done graphically, comparable to LabVIEW from National Instruments. The system controls the gas pressure, the DC plasma current, the magnetic field and security issues like the cooling water flow or various valves.

1.1.1 Modifications to the LEP module

Since different problems were encountered with the circular anode configuration (cf. chapter 3), the decision was taken to substantially modify the LEP module. The ring anode was replaced with a conical anode placed at the lower centre of the reactor. Also the Helmholtz coils for the confining magnetic field were replaced by larger coils producing a field approximately ten times higher. This new configuration (cf. figure 1.4) is yet very similar to the BAI 730 D reactor from Balzers. In the next chapters the new configured reactor is referred to as the linear LEP reactor compared to the original LEP reactor with a circular anode.

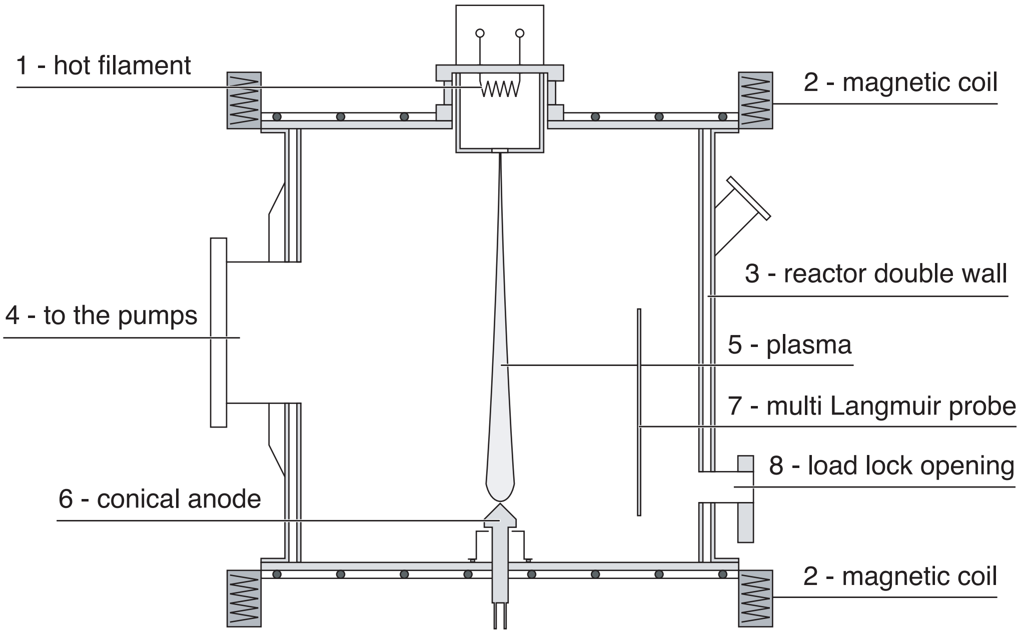

Figure 1.4: Schematic view of the modified LEP module with conical anode and columnar plasma

From circular anode to point anode

The new anode has a conical shape, according to studies for an optimal shaped anode in a DC discharge made previously by Balzers. The cooled anode is made of copper and is surrounded by an electrically floating protection which avoids parasitic plasmas between the anode and the grounded reactor wall.

Confining magnetic field

The original coils are replaced by two coils with 276 turns and a resistance of 1.9 Ω. The radius of the coils is $R = 340\,\mathrm{mm}$ and the distance between the coils is $d = 685\,\mathrm{mm}$. The maximum current in the coils, 10 A, is the same as before, but the resulting maximum magnetic field on the reactor axis is $B_\mathrm{c} = 45\,\mathrm{G}$. This is approximately the same field as the one used in the BAI reactor, leading to a plasma with a columnar shape.

1.1.2 Different probe positions

To analyse the different properties of the plasma in the reactor, several probes have been used. Figure 1.5 shows the different positions used for these probes in a side and in a top view. In the following chapters these positions will be referenced to the given numbers and letters. Numbers 1, 2 and 3 represent the positions of linear probes whereas a and b represent the positions of a 2D multi-Langmuir probe.

At positions 1 and 2 probes are installed with rotatable vacuum feedthroughs along one, preferably the vertical, axis. If not specified in the text, the probe is positioned at 0°, corresponding to the line indicated in the top view in figure 1.5.

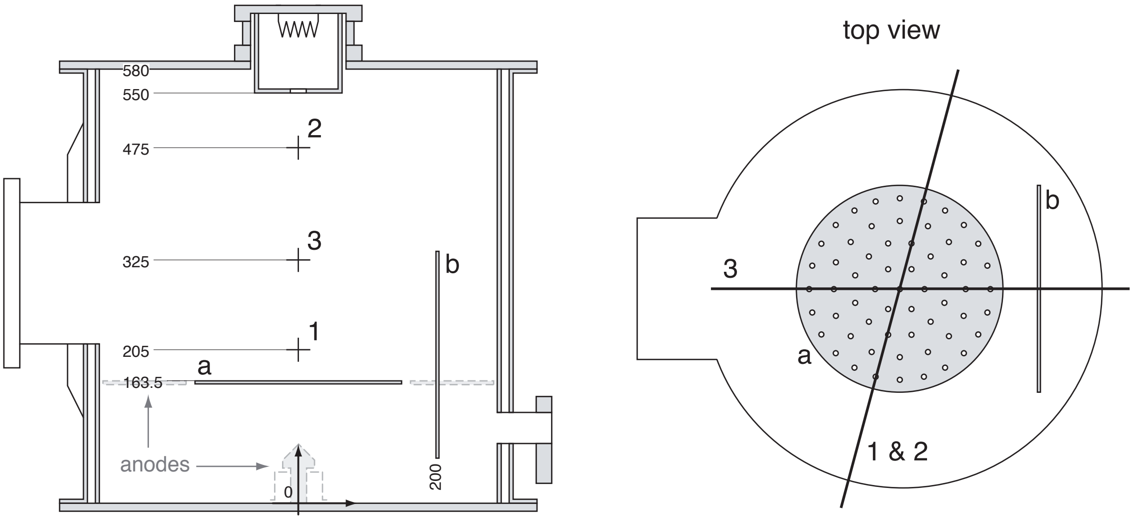

Figure 1.5: Schematic of different probe positions. 1–3: linear probes; a, b: 2D multi-Langmuir probe. Distances are given in millimeter and measured from the bottom center of the reactor.

1.2 The BAI 730 D reactor

The BAI 730 D reactor is the forerunner type of plasma reactors produced by Balzers (cf. figure 1.6). In principle it is similar to the modified LEP module: A DC discharge of typically 120 A and a practical upper limit of 180 A is initiated with a hot tungsten filament (1) in an ionisation chamber and drawn to a conical copper anode (6) placed in the lower part of the reactor chamber. The electrical circuit of the system is exactly the same as for the LEP module (cf. figure 1.2). The parameters defining the shape of the plasma (5) and therefore the type of deposition are all similar to the modified linear LEP module: a conical anode in the bottom of the reactor, a process pressure regime in the range of $10^{-3} - 10^{-2}$ mbar and a magnetic field of 50 G, produced by two coils (2) in a Helmholtz configuration with $R = 400$ mm and $d = 470$ mm. The plasma has a columnar shape producing a radial diffusive flux of ions and radicals used for the deposition.

However, there are several important differences between these two reactors. First of all the BAI is non-UHV and it is equipped to be used with different non-toxic and toxic gases such as argon, nitrogen, methane, silane or hydrogen. As such, it has been used for different types of experiments and depositions. Therefore the inner walls are contaminated with all kinds of materials despite several mechanical and plasma chemical cleanings. So the produced layers presented in chapter 5 do not meet the standard of layers used in industrial applications. Nevertheless, the films were analysed to improve the quality of the deposition and to increase the understanding of the process.

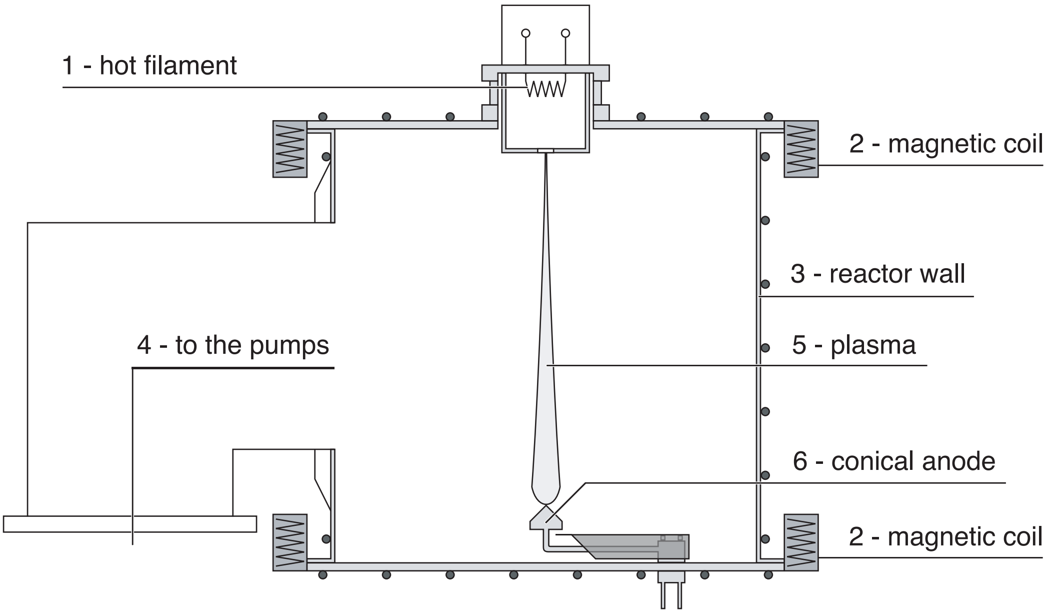

Figure 1.6: Schematic view of the BAI reactor adapted for low pressure plasmas.

Pumping system

A rotary vane pump (DUO 060) together with a roots pump (WKP 500) form the system to pump down the process module via a bypass connection from atmosphere to rough vacuum of 0.2 mbar. This is the original pumping system for different processes in the millibar range performed in this reactor, such as hard coatings or nitruration [1]. These pumps are well adapted for harsh processes with significant quantities of powder passing through the pumps, but they do not fulfill the requirements for clean conditions in modern PECVD.

A turbo pump (Leybold MAG 1600) is connected to a 90°-angle valve (4) installed at the side of the module. With this pump a base pressure of about 10^{-6} mbar is obtained, which is comparable to the one in the LEP module. As the reactor is non-UHV several leak-tests and optimisations of the sealing had to be performed in order to achieve such a low base pressure. The leak rate was found to be less than 0.02 sccm and for an optimal outgassing the reactor and substrates were heated with an argon plasma over a period of two hours.

Process configuration, laboratory version

The process configuration differs in one major way from the LEP configuration: The use of toxic and non-toxic process gases (cf. figure 1.7). This makes it necessary to pass the gas mixture exhaust from the pumping line through a gas reactive column (Edwards GRC). For the plasma discharge a GL 73 DC power supply from *Oerlikon Bührle* is used, principally dedicated for welding tools. The control of the complete system is done manually on the control rack.

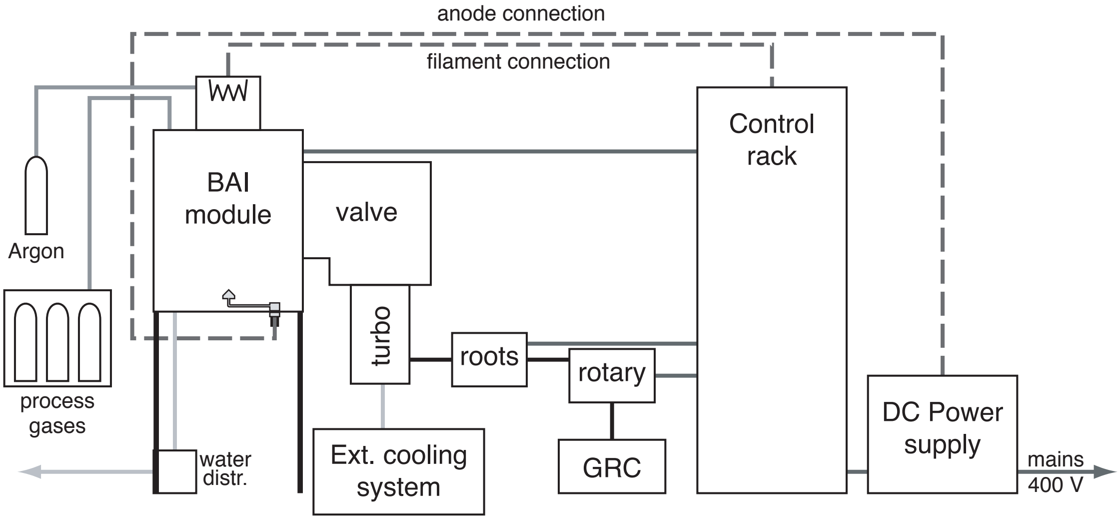

Figure 1.7: Schematic view of the complete process configuration for the BAI reactor.

1.2.1 Different substrate positions

For the experiments presented in chapter 5 thin films were deposited on silicon wafer and glass substrates, exposed vertically to the plasma at various heights and distances to the plasma. Figure 1.8 gives a schematic overview of the different substrate positions and fixation facilities. Silicon wafer pieces ($3 \times 3\,\mathrm{cm}^2$) and small glass samples ($5 \times 5\,\mathrm{cm}^2$) were fixed on floating substrate holders, typically at about 7 cm from the reactor axis. The substrate holders could be fixed at variable height to one of three floating bars (1–3). In general the substrates were positioned in front of the pumping line, fixed at bar 1. Another type of substrates used were large surface glasses ($47 \times 37\,\mathrm{cm}^2$), originally used in large surface RF reactors. They were installed either between the pumping line and the plasma (position a) or in pairs on both sides of the plasma (position b). At position a the glass was installed edgewise, set on the reactor floor and fixed to bar 1. At position b the two glasses were installed lengthwise about 12 cm above the floor, fixed to all three bars and exposed to the plasma on the complete height.

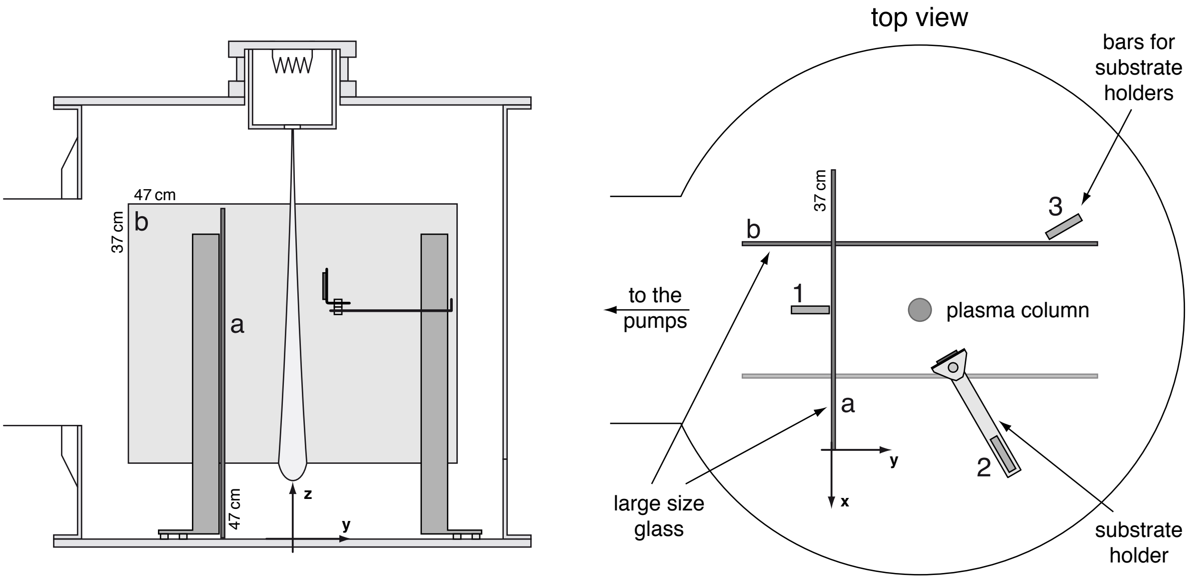

Figure 1.8: Schematic of different substrate positions and fixation facilities. 1–3: floating bars to fix the substrate holders; a, b: Positions of the large surface glasses, set edgewise (a) or lengthwise (b).

Chapter 2

Plasma diagnostics and material characterisation

In this chapter the different plasma diagnostics and film characterisation techniques are presented. Section 2.1 is dedicated to the classical plasma diagnostics like Langmuir probes and optical emission spectroscopy as well as to two new custom-built diagnostics: A multi-Langmuir probe and a multi-Hall probe. Sections 2.2 and 2.3 present the in-situ and ex-situ measurement techniques for the analysis of the silicon and silicon carbide films deposited in the BAI reactor.

2.1 Plasma diagnostics

2.1.1 Single Langmuir probe and double probe

A very easy plasma diagnostic is the measurement of the current-to-voltage characteristics of a conductor, immersed in the plasma. This type of probes was first introduced by Langmuir in 1926 [16]. The advantages of such a Langmuir probe is the simple handling and the minor local perturbations of the plasma due to its small size. The probe can be used to measure the ion and electron density and the electron temperature. In contrast to its simple experimental requirements, the analysis of the I-V characteristic can be quite complicated.

In this work two kinds of Langmuir probes have been used: a) a single pin Langmuir probe, where on small tungsten pin is exposed to the plasma and biased against the grounded reactor wall and b) a double pin Langmuir probe, where two electrically floating pins are biased against each other. A typical I-V characteristic and a schematic of the single pin Langmuir probe is presented in figure 2.1. At a bias voltage of $V = V_\mathrm{p}$, the probe has the same voltage as the plasma and the current flowing is mainly due to the more mobile electrons. Above this plasma potential, the current saturates, but a small increase is possible due to an increasing probe surface thus an increasing effective current collection area. With $V < V_\mathrm{p}$ the current decreases to zero at the floating potential V_f. It is known under this name as this voltage is found when an insulated, thus floating probe is immersed. When the bias potential is further decreased the probe attracts more and more positive charged ions, producing a negative current from the probe to the plasma, which saturates for sufficiently negative bias potential.

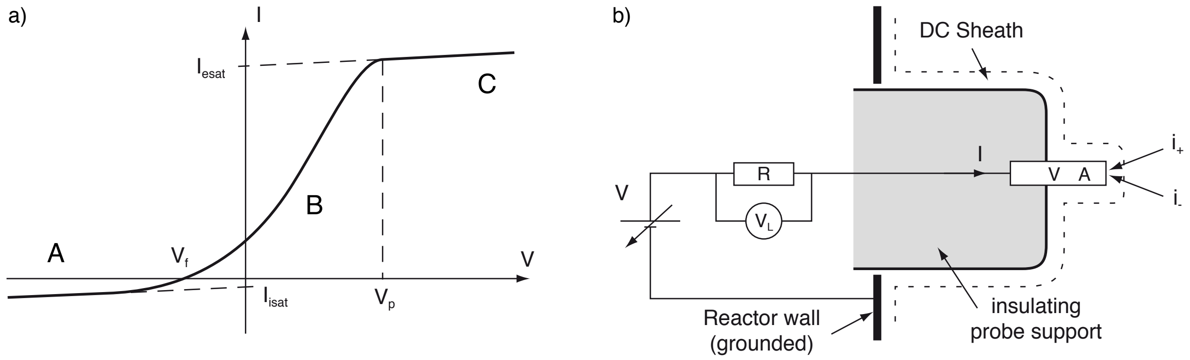

Figure 2.1: a) Typical single pin Langmuir probe I-V characteristic with A) the ion saturation region, B) the transition region and C) the electron saturation region; b) Schematic of the electric connections of the Langmuir probe.

Typically the measuring resistance is set between 0.2–10 kΩ, leading to a current maximum of about 1 mA. The pin of the Langmuir probe used had the following geometrical parameters: a cylindrical form with a radius of $r = 0.51\,\mathrm{mm}$ and a height of $h = 4\,\mathrm{mm}$, leading to a total surface of $A = 1.3635 \times 10^{-5}\,\mathrm{m}^2$. This surface is needed for the calculation of the ion saturation current density j_{isat}. With j_{isat} the electron density n_{e} can be calculated as

$$n_{\mathrm{e}} = 1.64 \frac{j_{\mathrm{isat}}}{e\sqrt{\frac{e\,T_{\mathrm{e}}}{m_{\mathrm{Ar}}}}}, \tag{2.1}$$

with T_{e} the electron temperature and m_{Ar} the argon mass. The electron temperature T_{e} is found straightforward by plotting the transition region of the I-V characteristics on a semilog scale. The electron temperature is found as the inverse of the linear fit of the characteristics as

$$\ln\left(\frac{I_{\mathrm{e}}}{I_{\mathrm{esat}}}\right) = \ln\left(\frac{I - I_{\mathrm{i}}}{I_{\mathrm{esat}}}\right) = \frac{V - V_{\mathrm{p}}}{T_{\mathrm{e}}},$$

with I_{e} and I_{i} the electron and ion current to the probe, respectively, and I_{esat} the electron saturation current. The ion current I_{i} can be approximated by the ion saturation current I_{isat}.

A typical I-V characteristic and a schematic of a double probe is shown in figure 2.2. As both pins are floating, the current flow between the to pins is non-zero only if $V \neq 0$. An advantage of the double probe is that the net current is always limited to the ion saturation current, which minimises the perturbation of the plasma. The major disadvantage of the probe is, that the pins collect only the high-energy tail of the electron distribution. These are not necessarily representative for the total energy distribution, especially when measuring in the DC plasma column, dominated by highly energetic primary electrons from the source. Therefore the electron temperature measurement with the double pin probe can be higher than the one found with the single pin probe.

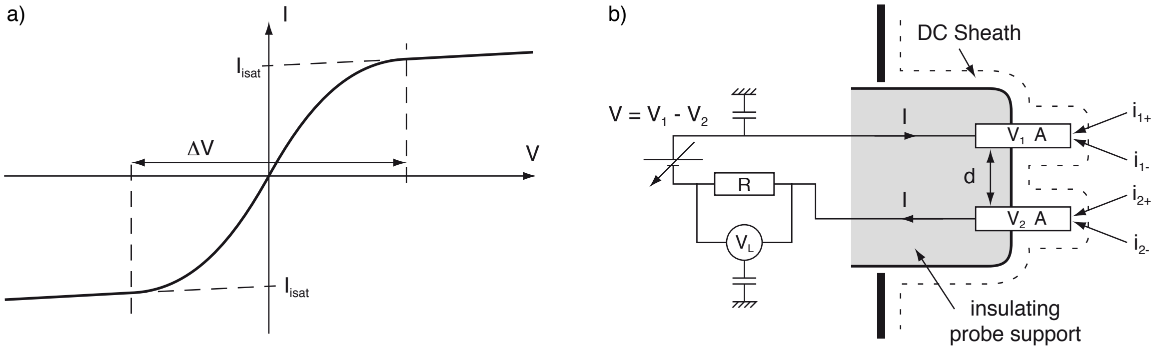

Figure 2.2: a) Typical double pin Langmuir probe I-V characteristic; b) Schematic of the electric connections of the floating Langmuir probe.

Assuming a bias voltage negative enough on one pin to collect only ions ($i_{2-} = 0$) and two pin surfaces of equal size, the I-V characteristic is given by

$$I = I_{\text{isat}} \tanh\left(\frac{e\,V}{2\,k_{\text{B}}\,T_{\text{e}}}\right),$$

with e the electron charge and k_{B} the Boltzmann constant. So with a straightforward fit of the measured I-V characteristic, the electron temperature T_{e} and the ion saturation current I_{isat} is found, and with equation 2.1 also the electron density n_{e} can be calculated [16, 9].

2.1.2 Multi-Langmuir probe

Two of the key parameters in deposition techniques are the homogeneity of layer thickness and the reproducibility, thus the stability, of the process. To analyse the effect of parameter variations and geometry changes a multi-Langmuir probe was developed, consisting of 59 single Langmuir surface probes. This multi probe is used in the LEP module with the ring anode as well as with the conical anode. In the case of the ring anode it is placed at the substrate position in the centre of the anode (cf. figure 2.3). In the case of the conical anode it is installed vertically with the lower part of the probe at the same level as the anode and with a distance of 200 mm from the reactor axis (cf. figure 1.5), which is approximately twice the distance of the substrates used in radial diffusion deposition.

The probe is primarily used to measure the ion saturation current to find the ion density at the substrate position. Therefore the probes are polarised to −30 V, which is sufficient for measurements with the ring anode and a weak magnetic field as well as for the measurements outside the hot plasma column in the linear configuration. The 59 signals are read out with a NI PXI 8176 multiplexer system from National Instruments. A block and circuit diagram of the probe is given in figure 2.4. The multiplexer consists of 4 input slots, each with 48 channels. As every Langmuir probe has its own ground connection, two channels are used for each probe. The digital multi meter (DMM) measures one by one the current passing through each of the probes but can also be used to measure the floating potential V_{f} when the 30 V floating power source is omitted and the DMM is

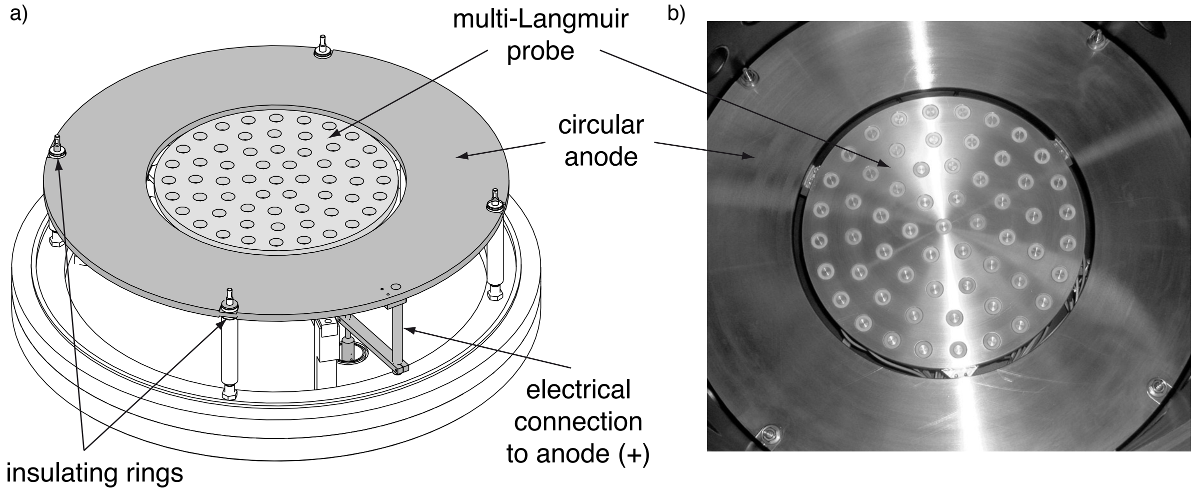

Figure 2.3: Schematic view (a) and photo (b) of the multi-Langmuir probe with its 59 sensors and the circular steel anode. The multi probe is level with the circular anode. The anode is placed on insulating rings held by four supporting bars.

configured for voltage measurement. The data acquisition from the DMM measurements is performed with a modified version of the LabVIEW program *DMM Switch Handshaking LV6.vi*.

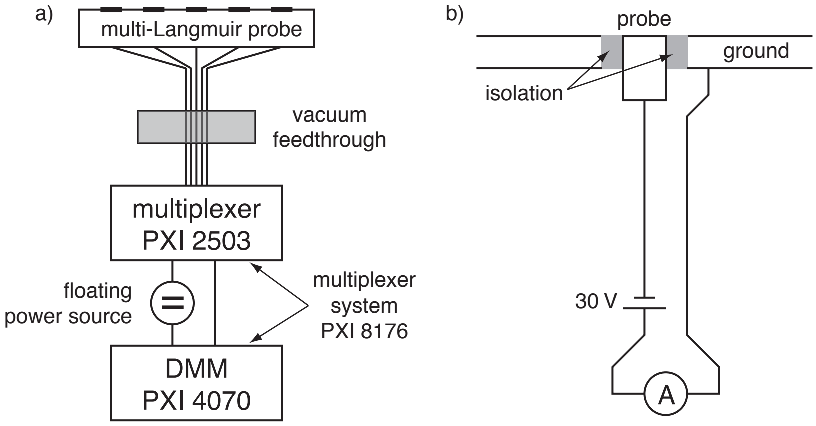

Figure 2.4: Schematic for the saturation current measurement. a) Block diagram of the multi-Langmuir probe; b) Circuit diagram of one Langmuir probe for measurements of I_{sat}. To measure V_{f} the 30 V floating power source is omitted and the DMM is configured for voltage measurement.

2.1.3 Multi-Hall probe for 2D plasma current profiles

Current density profiles in fusion devices have been intensely studied for more than thirty years and they are still of interest in fusion physics, especially with the ongoing developments for ITER. A large number of techniques have been developed: longitudinal or tangential Thompson scattering [17,18], discrete Alfvén wave spectrum [19], FIR polarimetry [20] and others [21]. Another field of application for current density measurements is related to space plasmas [22].

In this section a novel technique to measure the current density and direction in a low pressure, low energy plasma, as used for industrial applications, is presented. It consists mainly of an array of small Hall sensors measuring the magnetic field induced by the plasma current.

Single Hall probe prototype

In a first step a prototype of the Hall probe was developed. It consists of only one single Hall sensor (type CSA-1V from Sentron) fixed on one end of a hollow teflon rod. Inside the rod passed the cables for voltage supply and signal acquisition and cooling with compressed air. The whole probe is placed in a glass tube mounted on a fixed vacuum feedthrough. The direction of sensibility of the sensor is along the tube, referenced as the longitudinal direction. The readout of the signal is done with an oscilloscope.

The multi-Hall probe

The final multi-Hall probe consists of five main parts: (a) 24 Hall sensors brazed on four printed circuit boards (PCB) with the connections for the supply voltage and the signal acquisition as well as a noise filtering capacitor of 100 nF, (b) a glass tube closed on one end and passing through a vacuum feedthrough movable in one direction, (c) a mechanical support for the PCBs in the form of a steel half tube and containing a small tube for the air cooling, (d) a stabilised current generator as power supply for the sensors (GW PSM-3004) and (e) a data acquisition system[1] for the readout of the 24 signals (cf. figure 2.5a). With the 16 longitudinal and 8 transversal Hall sensors and the rotatable vacuum feed through, a 2D profile of the current density distribution can be established.

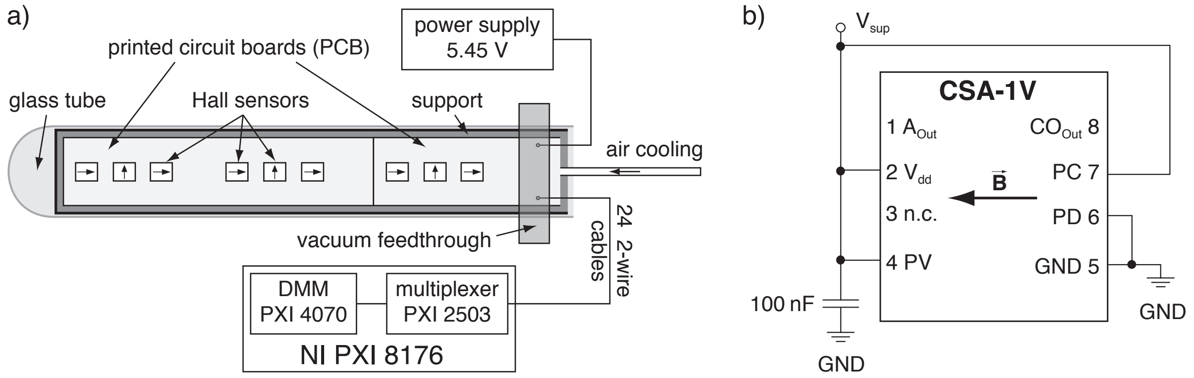

Figure 2.5: a) Schematic view of the complete multi-Hall probe system; b) Connection diagram of the CSA-1V sensor. **B** indicates the direction of a positive magnetic field.

---

[1] The same as used before with the multi-Langmuir probe

The CSA-1V is a single-axis integrated magnetic field sensor based on the Hall effect. The circuit is fabricated using a conventional CMOS technology with an additional ferromagnetic layer. The ferromagnetic layer is used as a magnetic flux concentrator providing a high magnetic gain. Therefore, the circuit features very high magnetic sensitivity, low offset, and low noise [23]. For reliable operation within the specifications the sensor is connected as shown in figure 2.5b. The differential signal is measured over $\mathrm{A_{Out}}$ and $\mathrm{CO_{Out}}$. The sensor is originally used to measure the current in a conductor on a PCB and placed under the sensor (cf. figure 2.6a).

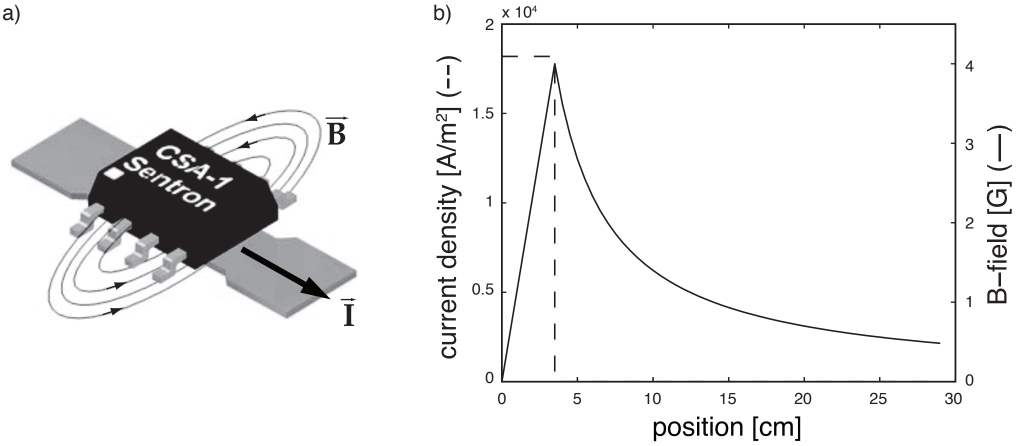

Figure 2.6: a) Typical use of the CSA-1V sensor: measurement of the current in a conductor on a PCB; b) Estimation of the magnetic field induced by a uniform plasma arc with 70 A and a radius of 3.5 cm.

Measurement accuracy

For our purpose the Hall probes need to be highly sensitive to the magnetic field. Estimating the field induced by a plasma arc of 70 A and an estimated radius of 3.5 cm gives a maximum field value of $B \approx 4\,\mathrm{G}$ (cf. figure 2.6b). In the case of a less contracted column or especially when using the circular anode, with only 50 A discharge current, the maximum magnetic field is still weaker. In the data sheet of the Hall sensor a typical sensitivity is given as $300\,\mathrm{VT^{-1}} = 30\,\mathrm{mVG^{-1}}$ [23]. A calibration with a gaussmeter (Bell 610 Gaussmeter) gives a proportion factor of $286\,\mathrm{VT^{-1}}$. Therefore for our application the signal is expected to be in the millivolt range.

The magnetic field measurements are typically averaged by performing several acquisitions. The frequency response of the sensor is measured from 0.1–1000 Hz, as presented in figure 2.7. This frequency response is sufficient, as will be seen in the next section, the interesting range of frequency in our case is between 10–100 Hz.

The maximum supply voltage for the sensors is 5.5 V. The graph in figure 2.8a shows a lower slope for higher voltages, justifying the choice of 5.45 V for the measurements. At this value $\Delta B/\Delta V \approx 3\,\mathrm{GV^{-1}}$ and the accuracy of the power supply is about 15 mV. This leads to a measurement accuracy of about 45 mG.

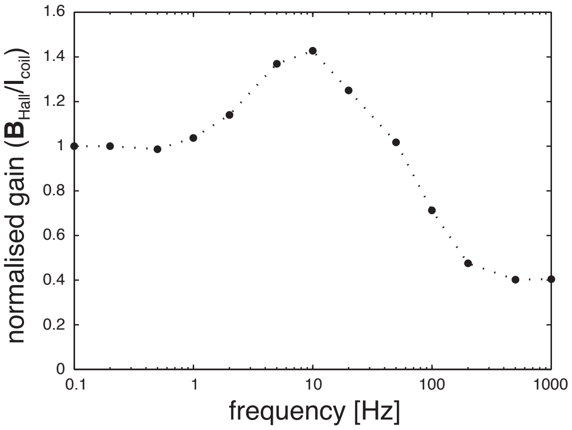

Figure 2.7: Normalised frequency response characteristics of the CSA-1V Hall sensor from 0.1–1000 Hz.

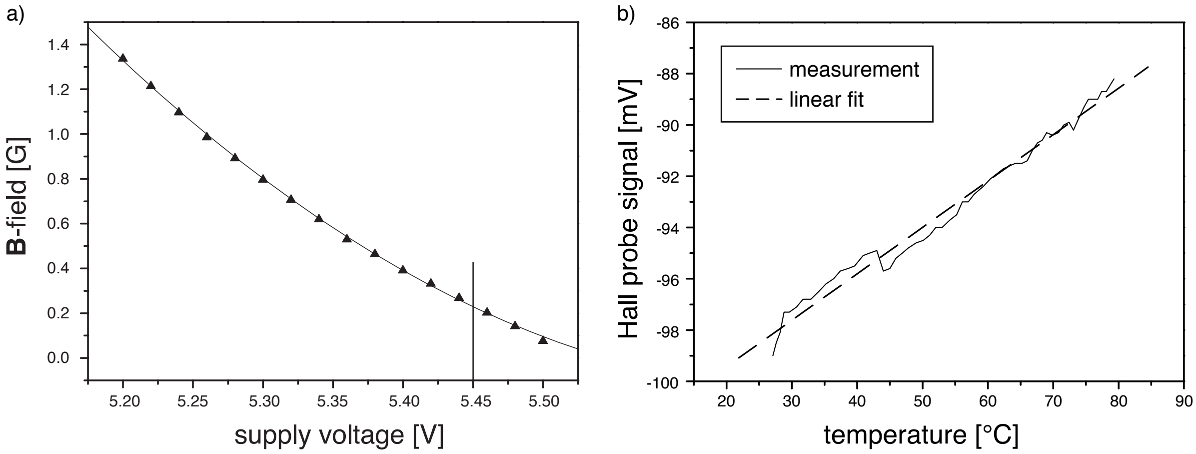

Figure 2.8: a) Stability analysis of the Hall probe measurements depending on the voltage supply of the sensor; b) Temperature drift measurement with a single Hall sensor. The linear fit gives a temperature drift of 0.181 mV/°C.

A further error source is the temperature drift. The guaranteed values given in the data sheet of the sensor are −0.2 to 0.2 mV/°C. A measurement of the temperature drift with the prototype probe gave a value of 0.181 mV/°C (cf. figure 2.8b). For moving the prototype probe across the glass tube, a time of about 10 min is needed to measure the complete profile at 25 points and the temperature in the probe varies between 40°–60°C.[2] This leads to a maximum error of 3.6 mV corresponding to a magnetic field of about 125 mG. So to stay below an error of 20 mG the measurement has to be done in a narrow temperature range of about 3°C. This, and the given temperature maximum for the sensor of 150°C, made it necessary to develop a multi sensor Hall probe with internal cooling that measures the complete profile within a few seconds. A convenient secondary effect of this multi-probe is the reduced time for the measurements.

---

[2] Without air cooling of the probe the increase in temperature in the same time is approximately five times higher, from 30°–130°C.

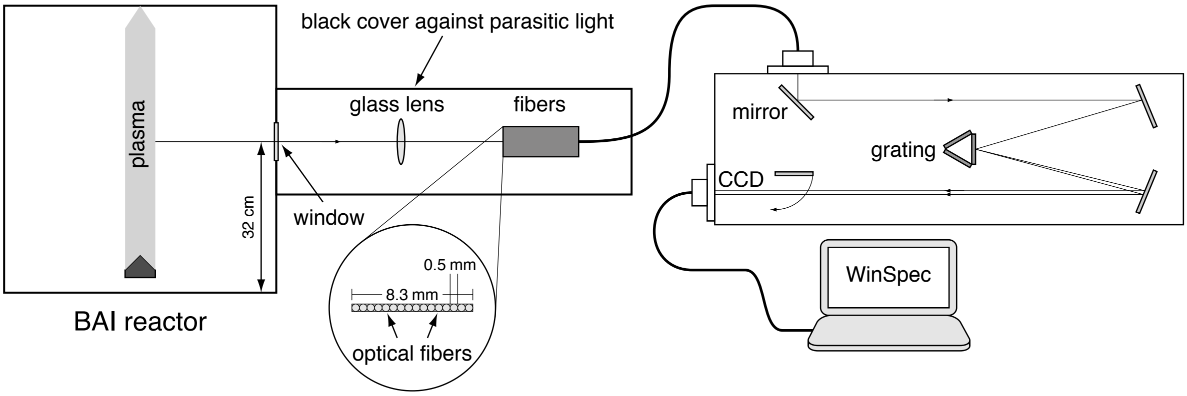

Figure 2.9: Schematic of the optical emission spectroscopy (OES) measurement installation.

2.1.4 Optical emission spectroscopy

For plasma species analysis a *SpectraPro-750i* imaging spectrograph from *Acton Research Corporation* was used. In figure 2.9 a schematic of the used system is given. The light, emitted by the plasma and passing through a quartz window (32 cm above reactor floor), is focused on 16 quartz fibers with a quartz lens (spectral transmission: 320–1200 nm, focal length: 200 mm). The fibers are oriented horizontally and the optical system allows to observe a zone of 4 cm of the plasma column. The column is centered between fibers 13 and 14 in order to measure the species inside and outside the plasma column, having a radius of about 2 cm. The fibers guide the beam towards the monochromator with a focal length of 0.75 m. It is equipped with mirrors to correct astigmatism, a diffraction grating with 150 lines/mm and a resolution of 0.18 nm. A CCD camera (*Spec-10:400B* from Princeton Instruments), with liquid nitrogen cooling, a 16 bit brightness resolution and a spatial resolution of 1340 × 400 pixels, captures simultaneously the chromatically and spatially resolved light. The signal of the camera is treated with the *WinSpec* software. For the spectral calibration of the monochromator a Hg-Ne lamp (*OMNILAB D-03929*) was used.

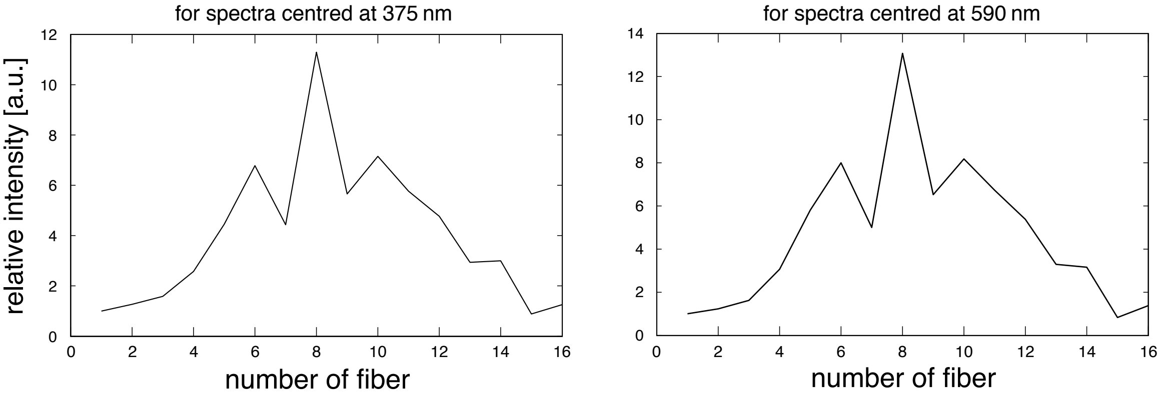

Figure 2.10: Relative intensity of the 16 fibers, measured for the two spectral domains used.

The 16 fibers vary in their sensitivity of the incoming light due to imperfections in the alignment. Therefore the fibers were calibrated by illuminating them with the spatial homogeneous light of a *MARKERlight* lamp (OS-ML03A). The total spectrum of every fiber was integrated, leading to the relative intensities of the fibers, shown in figure 2.10 for the two spectral domains used: 256–453 nm and 451–707 nm.

2.2 In situ film analysis

2.2.1 In situ growth rate measurement with reflectometry

The reflectometry is the only *in situ* method used in the framework of this thesis to analyse the deposited films. The relatively simple setup of this measurement consists of a Helium-Neon laser with a wavelength of 632.8 nm and a photodiode which captures the laser beam reflected from the growing film. A fringe model to simulate the measured interference patterns leads to various characteristics of the film: 1) the deposition rate and the final film thickness, 2) the refractive index (real and complex), 3) film porosity and 4) surface roughness of the film. In [10] a model for the case of a single-layer deposition on a reflective substrate is presented. A further development of this model presented in the next section includes also an intermediate layer on the bulk substrate. This intermediate layer can be a given native oxide layer or an unintentional layer of SiO_2 deposited during the heating process with the plasma.

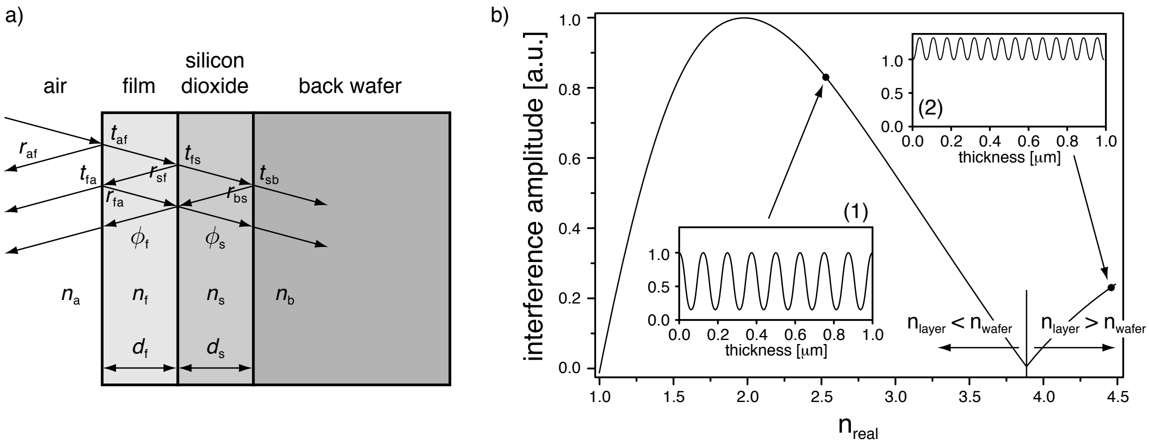

Figure 2.11: a) Propagation of an electromagnetic wave in a multilayer medium. ϕ_f and ϕ_s are the complex phase factors of the respective layers; b) Relation between interference fringe amplitude and the real part of refractive index of a film deposited on a silicon wafer ($n_{wafer} = 3.88 - 0.0179i$). [10]

Reflectometry fringes model

A laser beam reflected on the multilayer structure will show interference fringes due to multiple reflections inside the layer (cf. figure 2.11a). In the simple case of only one transparent layer growing on the wafer the normalised light signal has the behaviour presented in figure 2.11b. If $n_{\text{real}} < n_{\text{wafer}}$ the signal varies between 0 and 1, if $n_{\text{real}} > n_{\text{wafer}}$ the signal is always greater than 1. If the deposited layer is not completely transparent, the amplitude of the fringes will decrease as a part of the light is absorbed by the layer. The roughness of the interface between air and film determines how strong the total signal is reduced due to the light reflected in random direction, and porosity will affect the refractive index and therefore modify the size of the fringes.

The measurement shown in figure 2.12 was made during the deposition of a silicon film on a Si-wafer. After a normalisation of the measured intensity with respect to the starting point, the measured signal oscillates between values smaller than one and values bigger than one, which is impossible if only one layer was deposited. Therefore the model with only one deposited layer had to be improved, as with an additional intermediate layer the measured fringes can be perfectly simulated.

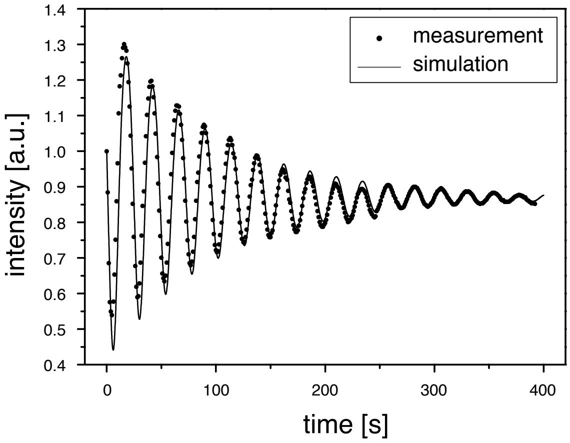

Figure 2.12: Reflectometry measurement (···) and simulation (—) of interference fringes during the deposition of a silicon film on a Si-wafer with a significant intermediate layer.

The refractive index of the Si-wafer is given as $n_{\text{wafer}} = 3.874 + 0.016\text{i}$ [24]. To reduce ambiguity in the determination of the simulation parameters used in figure 2.12, some assumptions were made: The refractive index of μc-Si:H at a wavelength of 632.8 nm is about 3.6 [25] and the thickness of the intermediate layer is about 10 nm (cf. TEM measurements in figure 2.13). The parameters found for the simulation with the multi-layer model were: the deposition rate $d = 3.84\,\text{nm/s}$, the refractive index of the intermediate layer $n_{\text{s}} = 1.1$ and of the film $n_{\text{f}} = 3.43 + 0.13\text{i}$ and the thickness of the intermediate layer $d_{\text{s}} = 14\,\text{nm}$. The measurements showed no significant effects of roughness or porosity. As the support of the wafer is sensitive to the heating and is weakly fixed, it can slightly move during the deposition. Therefore the reflected beam can partially miss the photodiode if not adjusted. This explains the difference between measurement and simulation at the beginning and also the small jump around 250 s.

The single-layer model includes only one deposition layer, for instance the deposition of an incubation layer. This layer was found with TEM measurements of films deposited in the BAI reactor when heating up the wafer with an argon plasma of about 30 min. In figure 2.13 an amorphous incubation layer with a thickness of about 110 nm is shown. To find the total reflection and transmission coefficients (Fresnel coefficients) in a multi-layer system all the different intensities from the reflected or transmitted waves have to be

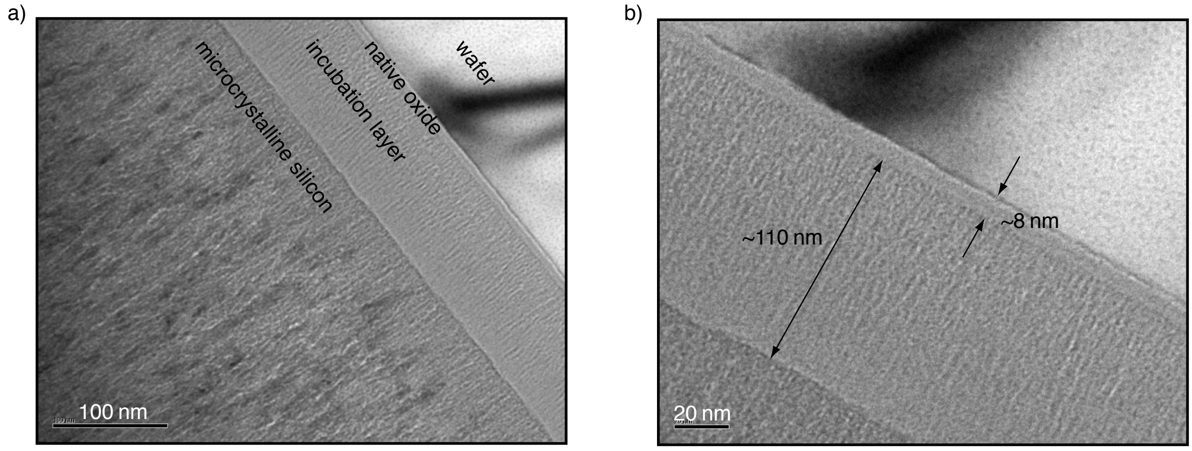

Figure 2.13: TEM measurements showing a wafer on which is deposited a three-layer system with a native oxide layer ($\approx 8\,\text{nm}$), an amorphous incubation layer ($\approx 110\,\text{nm}$) and the microcrystalline silicon layer.

summed. These infinite series can be simplified to give the following expressions:

$$r_{\text{ab}} = r_{\text{as}} + \frac{t_{\text{as}}\, t_{\text{sa}}\, r_{\text{sb}}\, \phi_{\text{s}}^2}{1 - r_{\text{sa}}\, r_{\text{sb}}\, \phi_{\text{s}}^2} \quad ; \quad t_{\text{ab}} = \frac{t_{\text{as}}\, t_{\text{sb}}\, \phi_{\text{s}}}{1 - r_{\text{sa}}\, r_{\text{sb}}\, \phi_{\text{s}}^2} \tag{2.2}$$

where $\phi_{\text{s}} = \exp(j\omega n_{\text{s}} d_{\text{s}}/c)$ is the complex phase factor, defining the transformation of the wave inside the layer, and the complex amplitude reflection and transmission coefficients r and t depend on the corresponding refractive indices. They are calculated as:

$$r_{\text{ij}} = \left(\frac{n_{\text{i}} - n_{\text{j}}}{n_{\text{i}} + n_{\text{j}}}\right) \quad ; \quad t_{\text{ij}} = \left(\frac{2n_{\text{i}}}{n_{\text{i}} + n_{\text{j}}}\right)$$

Finally the total reflectance, measured with the photodiode, and transmittance are found as:

$$R_{\text{ab}} = |r_{\text{ab}}|^2 \quad ; \quad T_{\text{ab}} = |t_{\text{ab}}|^2$$

To refine this model for the case of a second layer, all the reflection and transmission coefficients at the interface air-SiO_2 have to be recalculated the same way as in equation 2.2. This includes the coefficients r_{as}, r_{sa}, t_{as} and t_{sa}. In these calculations the indices change as b → s and s → f, leading also to a new phase factor ϕ_{f}. At the same time the phase factor ϕ_{s} becomes constant as the layer no longer changes in thickness.

The effect of a rough surface profile is to introduce a small shift into the Fresnel coefficients [26]. They are recalculated as

$$r'_{\text{ij}} = r_{\text{ij}} S_{\text{ij}} = r_{\text{ij}} \exp(-2k^2 n_{\text{i}}^2 \sigma^2) \quad ; \quad t'_{\text{ij}} = t_{\text{ij}} S_{\text{t}} = t_{\text{ij}} \exp\left(\frac{-k^2 (n_{\text{j}} - n_{\text{i}})^2 \sigma^2}{2}\right)$$

with k the wave number, n_{i} and n_{j} the corresponding refraction coefficients and σ the standard deviation of a Gaussian probability distribution defining the probability for every point of the surface to be at a certain height. The new coefficients r' and t' are called the *incoherent roughness* Fresnel coefficients. To introduce roughness into the model, all coefficients at the interface air–film and, depending on the origin of the intermediate SiO_2 layer, also at the interface film–SiO_2 have to be adapted.

The last effect included in the model is porosity of the deposited film, presented by Bruggeman et al. [27]. For media with relative permittivity ε_i, the effective permittivity of a binary mixture is ε_{eff}, given by

$$d\left(\frac{\varepsilon_1-\varepsilon_{\text{eff}}}{\varepsilon_1+2\varepsilon_{\text{eff}}}\right)+(1-d)\left(\frac{\varepsilon_2-\varepsilon_{\text{eff}}}{\varepsilon_2+2\varepsilon_{\text{eff}}}\right)=0$$

where d is the fraction of volume of media 1 and $\varepsilon_2=\varepsilon_{\text{air}}=1$ for porous films. The effective complex refractive index is then given by $n_{\text{eff}}=\sqrt{\varepsilon_{\text{eff}}}$.

With the final version of the model, including all these different effects, the interference fringes measured on silicon and silicon carbide films were fitted (as shown in figure 2.12) in order to calculate the growth rate and to characterise the film structure.

2.3 Ex situ film analysis

2.3.1 Micro-Raman spectroscopy

The Raman effect, first reported by Raman and Krishna in 1928 [28], has been used in this work to evaluate the degree of crystallinity of the deposited silicon layers [4].

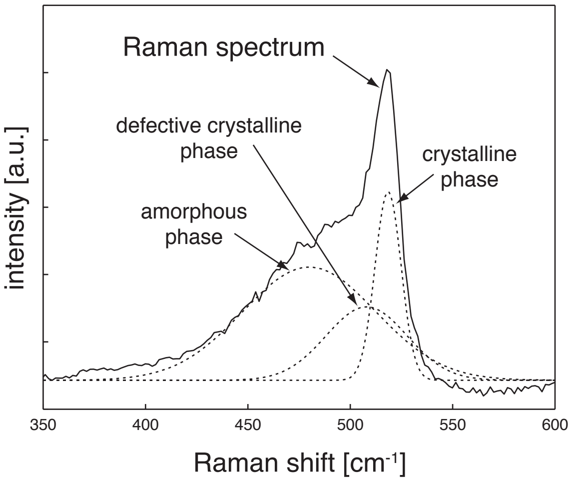

Figure 2.14: Gaussian fitting of a Raman spectrum with three peaks centered at 480, 510 and 518 cm^{-1} associated with amorphous, defective crystalline and crystalline silicon phases, respectively. The sample presented here has a Raman crystallinity of 42 % [4].

Figure 2.14 shows a typical Raman spectrum of a microcrystalline silicon film. The spectrum can be separated into three peaks, being fitted with three different Gaussian peaks centered at 480 cm^{-1}, 510 cm^{-1} and 518 cm^{-1}. These three peaks are associated with amorphous, defective crystalline and crystalline silicon materials structure, respectively. The Raman crystallinity is defined as

$$\phi_c=\frac{A_{518}+A_{510}}{A_{518}+A_{510}+A_{480}}, \tag{2.3}$$

where A_j is the area of the peak centered at j cm^{-1}. This generally accepted [29, 30] definition gives a rough estimation of the crystallinity.

For the measurement of the Raman spectra of μc-Si:H films deposited in the BAI reactor, a Micro-Raman spectroscopy system was used. It consists mainly of three parts: A laser source, a spectrometer and a microscope, holding the studied sample (cf. figure 2.15. Several technical improvements made in the last 20 years transformed the Raman spectrometers into easy to use tools: a) modern compact laser sources are much more practical and cheaper than before, b) an efficient notch filter rejects the strong light from Rayleigh scattering, c) modern CCDs with improved signal to noise ratios and the ability to register multi-wavelength signals and d) last but not least the progress in informatics, resulting in cheap but powerful PCs used for the control of the spectrometer and the CCDs.

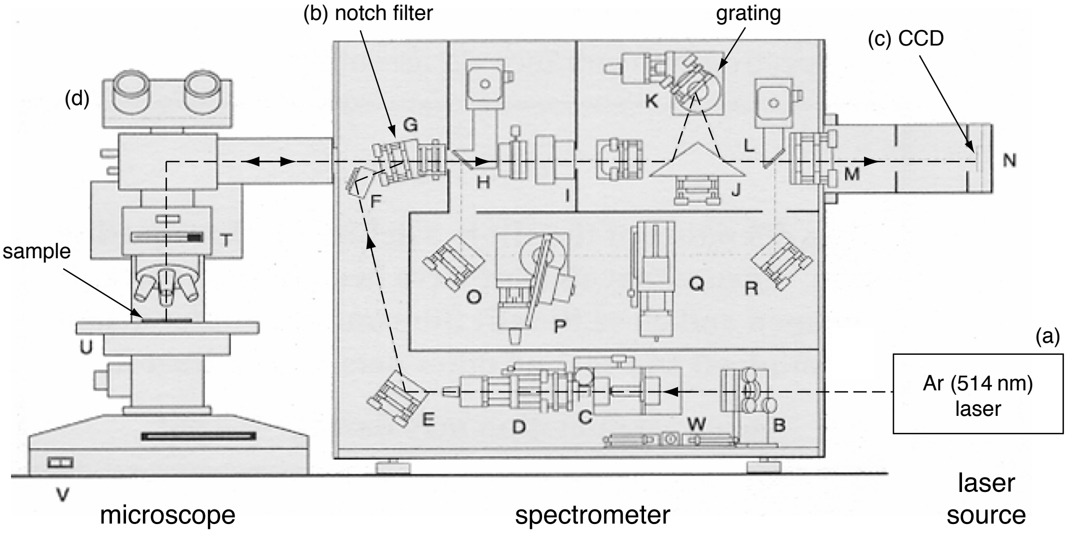

Figure 2.15: Micro-Raman spectrometer composed of an Ar laser source, a microscope, a notch filter, a grating and a CCD camera.

The Micro-Raman system used for this work was a *Renishaw RM series* with an Ar laser source (514 nm). The advantage of the Micro-Raman is the additional optical microscope, focusing the laser beam on the film surface, which improves the output signal. The measurements were made with a microscope magnification of 50, resulting in a 2 mm diameter laser spot. To avoid crystallisation of the silicon structure due to the illumination of the film with the laser beam, the laser was blocked during the alignment of the sample under the microscope and the 20 acquisitions for one Raman spectrum were limited to one second per acquisition.

2.3.2 Alpha-step device

For ex situ measurements of the film thickness and deposition rate of thin silicon and silicon carbide films produced in the BAI reactor, an *alpha-step 200* device from *Tencor Instruments* was used. The alpha-step 200 is a rapid and easy-to-use stylus-based surface profiler with a manual X-Y stage and computer controlled scanning and data collection.

On a video screen a magnified image of the sample and the stylus is displayed, as well as the scanned profile and several control parameters.

To measure the vertical profile of the sample, the stylus, in contact with the film, moves linearly along a chosen direction on the surface (cf. figure 2.16a). The vertical deflection of the stylus is measured by means of an induction coil and a magnetic core fixed to the stylus. By moving the core inside the coil, the inductance of the coil changes. This inductance can be measured with a high precision leading to a vertical resolution of 5 Å. The horizontal resolution is about 400 Å. For reliability, the measured profile has to be leveled after the acquisition.

In order to measure the thickness of a deposited film, it is necessary to have a zone of deposition close to a clean reference zone, where no material was deposited. In figure 2.16b the three steps to be executed are shown. First a spot was drawn on the substrate with a waterproof marker (1), which hinders the deposition material from adhering to the underlying substrate. After the deposition process (2), the thin film at the spot position is washed away with alcohol and cleaning paper (3), leaving on the wafer an undeposited zone necessary for the alpha-step measurements. To avoid errors due to variable film thickness, every spot is measured three times in three different directions.

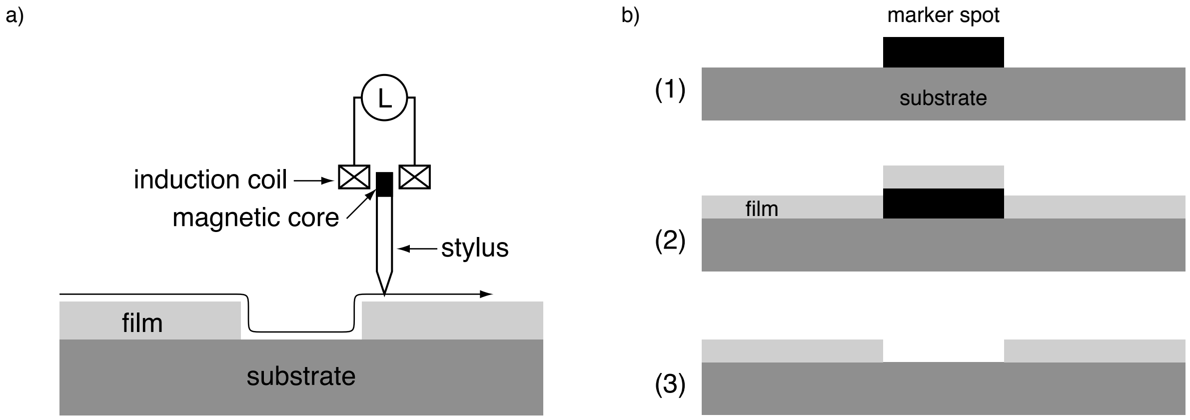

Figure 2.16: a) Schematic of the alpha-step measurement. The vertical position of the stylus is registered with an inductance measurement on a coil, fixed around the mobile stylus holding a magnetic core; b) Preparation process for the thickness measurements: (1) marker spot on the wafer, (2) film deposition, (3) after film elimination at marker spot position.

2.3.3 Spectroscopic Reflectometer

A second ex situ method to measure the film thickness is the spectroscopic reflectometry. This method is better adapted for the measurement of large surface depositions, where the alpha-step device is not adequate. A *NanoCalc-2000-UV/VIS/NIR* reflectometer from *Mikropack* was used to measure the thickness of silicon films deposited on large surface glasses in the BAI reactor. The light source frequency ranges from ultraviolet (UV) to near infrared (NIR) (250–1100 nm).

The measurement principle of the reflectometer is the interference of light in thin layers. The light coming from the light source is reflected and partially transmitted, resulting in phase shifts and superposition of amplitudes and finally adding up to different intensities for different wavelengths. A typical reflectance signal is given in figure 2.17, measured on a silicon film deposited on a glass substrate.

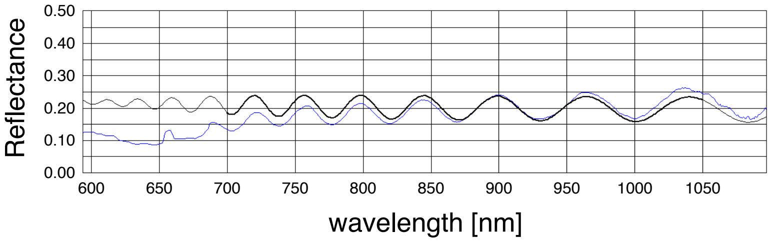

Figure 2.17: Reflectometry measurement (—) and interpolation (—) of a rough silicon film deposited on a glass substrate. The found film thickness is 1693.2 nm with a high roughness of $R = 86\,\%$ at the boundary between wafer and silicon film and a low roughness of $R = 21\,\%$ at the top surface of the film.

The reflectance measurement is interpolated with the *NanoCalc* software. For the model used by the software one has to define the single layer or multilayer film composition with the appropriate refractive indices and the roughness of the different layer boundaries. The measurements presented in figure 2.17 gave a film thickness of 1693.2 nm. The roughness R is defined as the percental loss of light at a certain boundary. Between silicon wafer and deposited silicon film the roughness is high ($R = 86\,\%$). The film surface however has a low roughness ($R = 21\,\%$).

Chapter 3

Plasma instabilities and non-uniformities

As mentioned in section 1.1, in industrial applications a homogeneity in film thickness of less than 5 % is achieved by using two different magnetic fields: The static field produced with one of the two Helmholtz coils, and a dynamic field produced with four solenoids or "wobblers". In this chapter the effects of the different magnetic field components on the plasma density will be studied as well as different types of instabilities appearing due to the use of the circular anode and the DC source for the filament heating. In the last section the effects of a third type of plasma confining field, a multipolar cusp field, is discussed. The expected effect of using this cusp field is a stabilisation of the plasma and an increased plasma density towards the reactor walls. This would lead to a more uniform plasma density profile and avoid the use of the dynamic field component of the wobblers.

3.1 LEP configuration with circular anode

Figure 3.1 shows four profiles of ion saturation current density at argon pressures from 0.003 mbar to 0.01 mbar and a discharge current of 50 A, found with the multi-Langmuir probe. In this case the magnetic field given by the Helmholtz coils is at its maximum of 5.4 G and no wobblers are used. The neutral density n_0 is calculated from the gas pressure and an estimated mean temperature of 200°C. The indicated homogeneity h of the measured values of current density j_i is calculated as $h = (j_\mathrm{max} - j_\mathrm{min})/(j_\mathrm{max} + j_\mathrm{min})$. The plasma density $n = n_\mathrm{i} = n_\mathrm{e}$ is calculated from the ion saturation current density j_isat and an estimated value of the electron temperature $T_\mathrm{e} = 4\,\mathrm{eV}$ (cf. section 4.2.1):

$$j_\mathrm{isat} = e n_\mathrm{s} u_\mathrm{B} \quad \Rightarrow \quad n_\mathrm{e} = 1.64 \frac{j_\mathrm{isat}}{e\sqrt{\frac{eT_\mathrm{e}}{m_\mathrm{Ar}}}}$$

with j_isat the current density in $\mathrm{Am^{-2}}$, n_e and n_s the electron respectively the sheath edge density in $\mathrm{m^{-3}}$, u_B the Bohm velocity in $\mathrm{ms^{-1}}$ and T_e in eV [16].

The measurements show two important results. First, the maximum plasma density n decreases from 8 to $3 \times 10^{16}\,\mathrm{m^{-3}}$ with increasing pressure. This leads to a strong decrease of the maximum ionisation degree from 0.18 % to 0.02 %. At the same time the mean free path decreases from 17 cm to 5 cm. So the loss of ionisation can be explained by a stronger radial scattering loss of the primary electrons from the source in a denser gas. The density of primary electrons and hence the ionisation rate in the lower part of the reactor decreases with higher pressure. Secondly, the homogeneity changes only by about 4.5 % from low to high pressure, despite the strong change in plasma density. In these cases the plasma density is too inhomogeneous to obtain a deposited layer meeting industrial requirements.

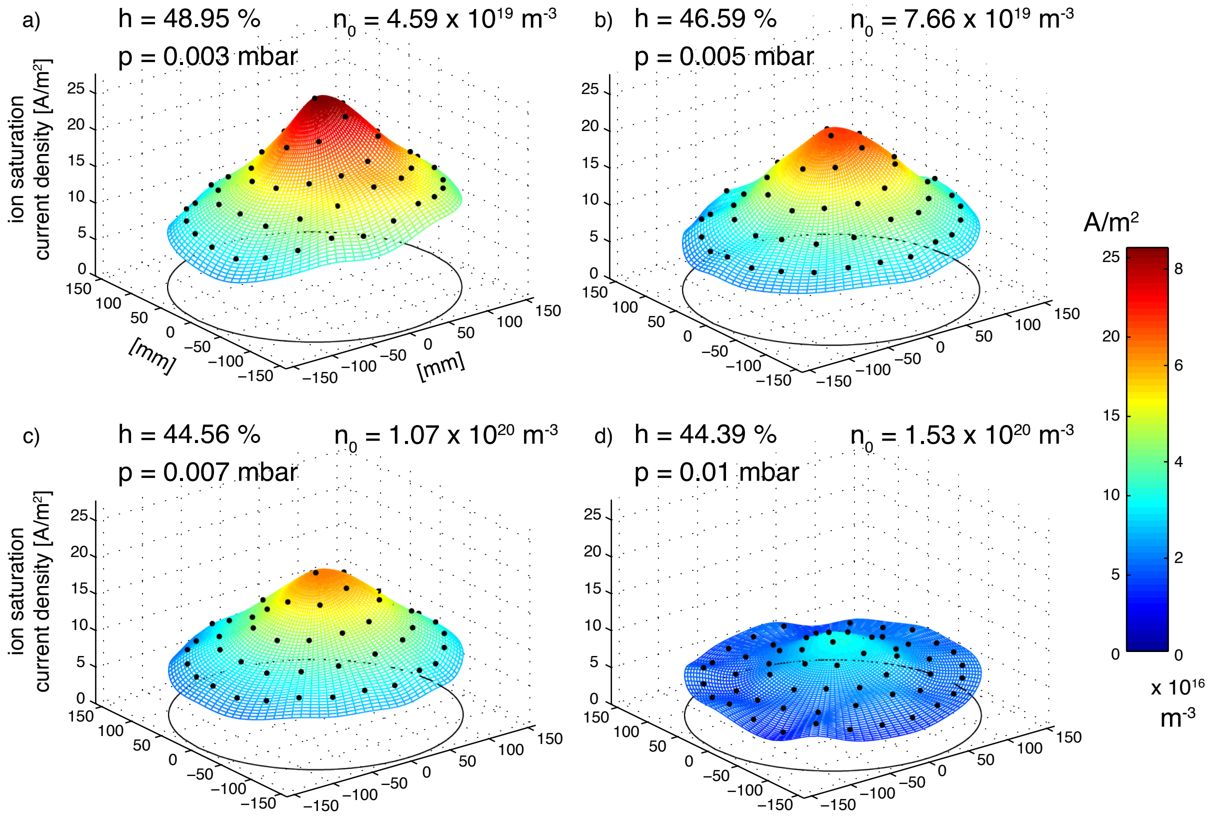

Figure 3.1: Profiles of plasma density measured with the multi-Langmuir probe. Measurements are made at a maximum magnetic field of 5.4 G and for four different pressures.

To get closer to the configuration of the LEP module with circular anode and wobblers used for industrial applications, the magnetic field is reduced to 2.7 G. In figure 3.2 the measured plasma density is shown for the same conditions as in figure 3.1. Three important differences are found with the weaker field. The most visible is the less axisymmetric behaviour of the plasma. Secondly the plasma density decreased by a factor of 2–3. This could be explained by a higher radial scattering loss of the primary electrons due to a weaker field on the reactor axis, but also with a higher loss rate of primary electrons that do not pass the orifice between source and reactor chamber. And thirdly the homogeneity increased by about 10 %, except for the measurements at 0.01 mbar, where the increase in homogeneity is only of 2.5 %. This is a slight improvement but still insufficient for any

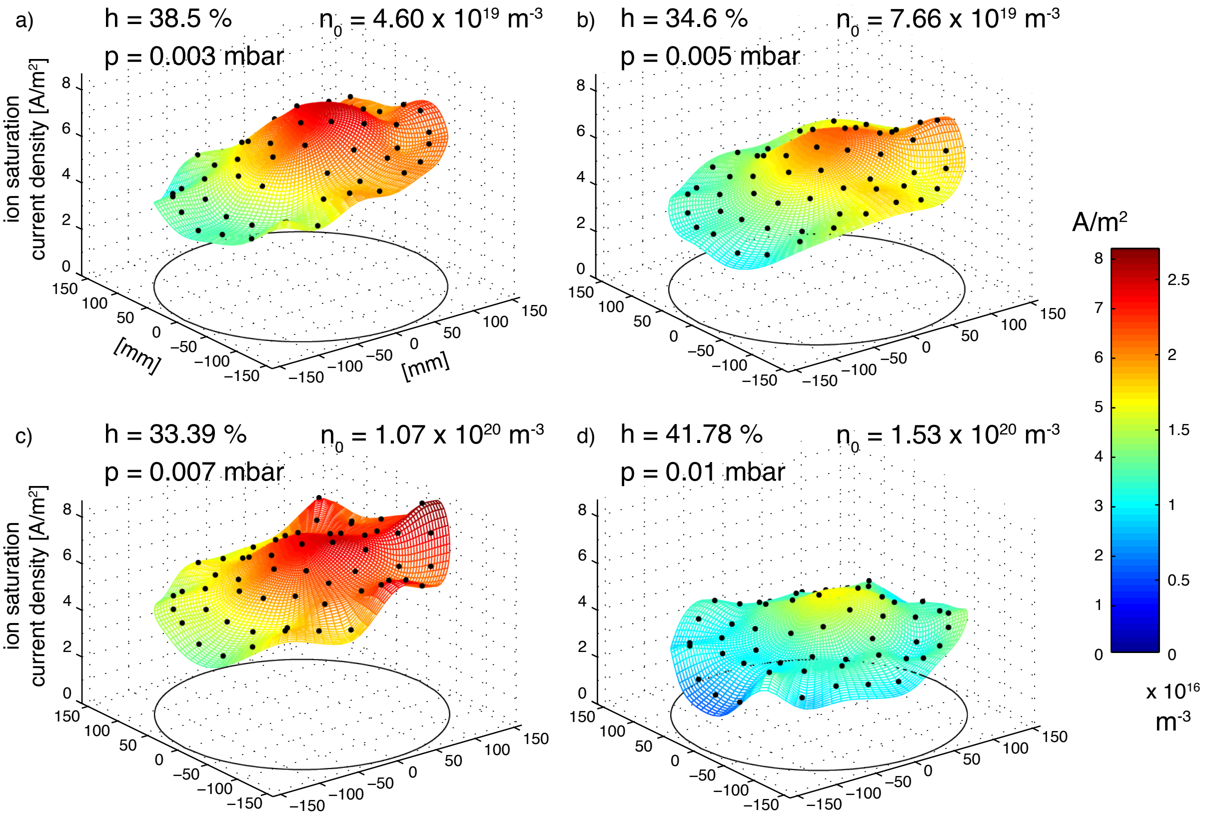

Figure 3.2: Profiles of plasma density measured with the multi-Langmuir probe. Measurements are made at a magnetic field of 2.7 G and for four different pressures.

technical application.

The reduction in symmetry shows a main problem of this type of discharge. With reduced magnetic field the plasma becomes unstable. The discharge either finds one point of attachment on the circular anode or it bounces between several preferential points. It seems to be very difficult if not impossible to have an absolutely symmetric anode, especially when the reactor is used for deposition of silicon or other semiconductor materials. These materials will be deposited on the anode, eventually breaking the symmetry. Even a plasma cleaning or a mechanical treatment of the anode would not reinstall the initial symmetry. The problems in getting a stable plasma and at the same time a homogeneous electron density distribution, led to the idea of installing a cusp field at the lateral reactor wall. The effects of this field on the plasma are discussed later in section 3.3.

To test the multi probe and study the effect of the dynamic magnetic field used in industry, one of the four wobblers was installed. The ion saturation current density found when applying a DC current of ±0.67 A is shown in figure 3.3. The static field has a magnitude of $B_\mathrm{w} \approx 100\,\mathrm{G}$ at the inner chamber wall and decreases to $B_\mathrm{w} \approx 2\,\mathrm{G}$ on the axis.

The measurements demonstrate that one can move the high density zone of the plasma to the edge of the substrate and, by using the four solenoids with a phase shift, produce a

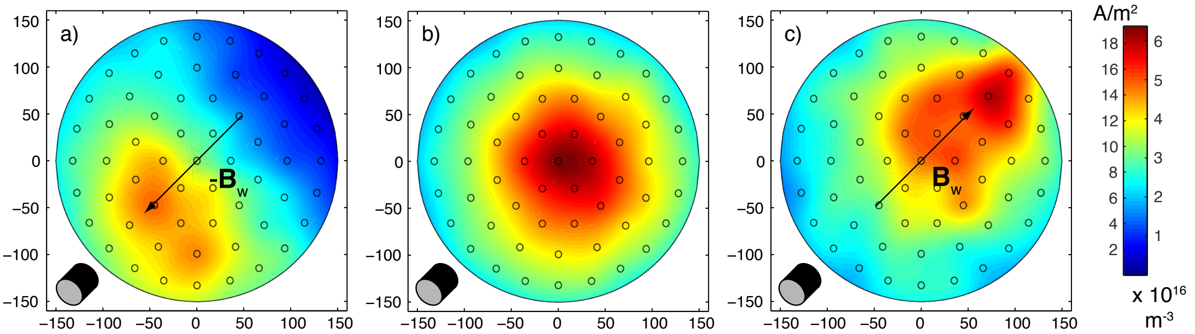

Figure 3.3: Effect of a horizontal magnetic field on the plasma produced by one solenoid (black cylinder). Magnitude of $B_\mathrm{w} \approx 100\,\mathrm{G}$ at the inner chamber wall and $\approx 2\,\mathrm{G}$ on the axis.

homogeneous layer averaged over a certain time. Comparing figures 3.3a and 3.3c, which should be symmetric along an axis perpendicular to the field vector of $\mathbf{B}_\mathrm{w}$, shows again that the configuration of the reactor with a circular anode leads to homogeneity problems.

3.1.1 Filtering the DC power supply

Measurements made with a double probe have shown that a strong noise is induced from the Fronius DPS 400 power supply, providing the discharge current. The noise made it difficult to fit the double probe characteristics and to find the plasma parameters such as electron density and temperature. To avoid this noise a low-pass filter on the output of the power supply was installed. In order to choose adequate filter components, the current surge during the plasma ignition and the noisy current signal was measured at the power supply output (cf. figure 3.4a). The amplitude of the current noise is about 20 A peak to peak or 25 % of the set value and a Fast Fourier Transform (FFT) analysis (cf. figure 3.4b) shows the main component at 59.4 kHz.

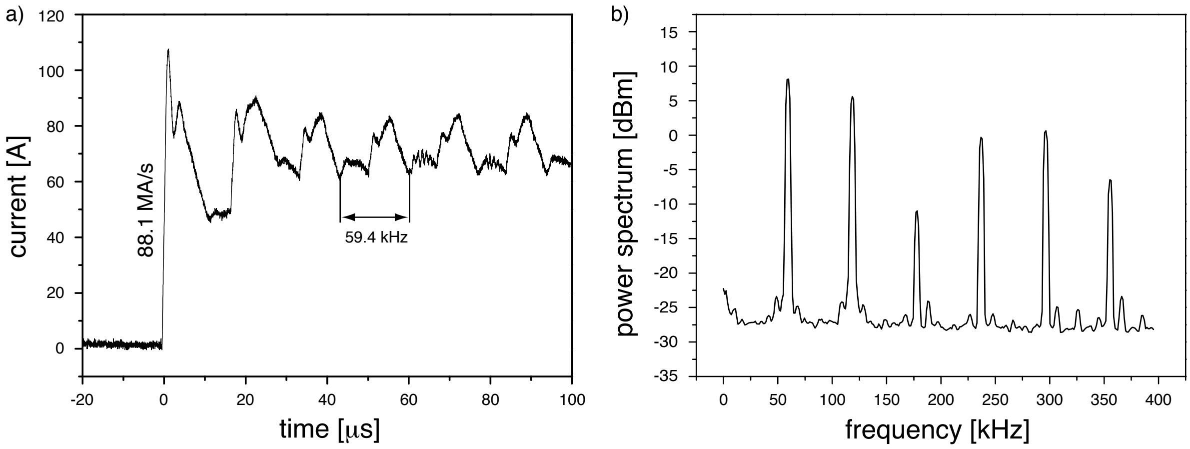

Figure 3.4: a) Current surge during plasma ignition of $88.1\,\mathrm{MAs}^{-1}$ and characteristic noise found on the plasma current; b) FFT of the noisy voltage signal measured over a $0.4\,\Omega$ dummy load with peaks at 59.4 kHz and its harmonics.

The finally installed filter consists only of a 180 μF capacitor as shown in figure 3.5a. The filter will slow down the fast current surge of 88.1 MA s^{-1} found without filter to approximately 100 kA s^{-1}, but several tests have shown this has no negative effects on the plasma ignition.

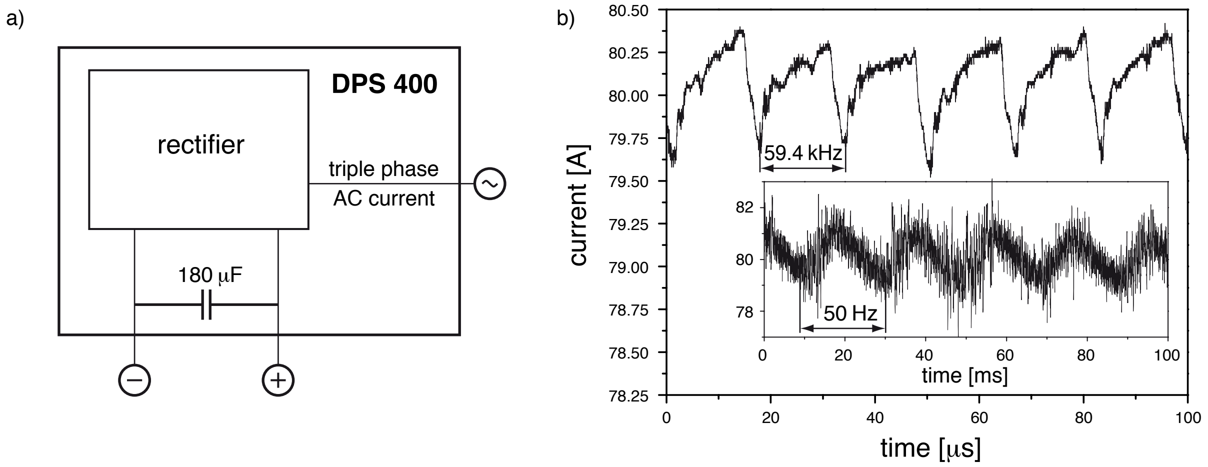

Figure 3.5: a) Schematic of the DPS 400 with a 180 μF capacitor used as low-pass filter; b) Noise measurements on the modified power supply showing two types of noise: 50 Hz and 60 kHz.

A repetition of the noise measurements using the modified power supply (cf. figure 3.5b) show a significant reduction of the high frequent noise at 59.4 kHz. The amplitude of the noise decreases by a factor of 20 to less than 1 A peak to peak. However another type of noise was found, hidden before by the high frequency signal. This noise of 50 Hz and of about 4 A peak to peak is inherent to the system and originates from the filament heating AC current. Although the filtered output shows a noise that is reduced by a factor of 5 compared to the original high frequency noise, a variation of 5 % of the "DC" current is not negligible and has an effect on the plasma as will be shown in section 3.2. Therefore new types of power sources were introduced for the filament heating and the plasma discharge as shown in the next section.

3.1.2 Noise characterisation of new DC power sources

In order to reduce the noise in the plasma coming from different sources, two separated DC power sources from HP were used for the DC discharge and the filament heating current. In figure 3.6 the noise characteristics of the HP 6469C, used for the DC discharge, and of the HP 6472C, used for the filament heating, are presented. The frequency analyses were made with a voltage measurement over a 0.4 Ω dummy load connected to the power sources and an applied current of 50 A.

The presented frequencies of 50 Hz, 100 Hz and 150 Hz are the only noise found up to 100 MHz on these sources. Comparable measurements done with the Fronius DPS 400 power source show no noise at 50 Hz or its harmonics, but still a strong noise at 59.4 kHz was found.

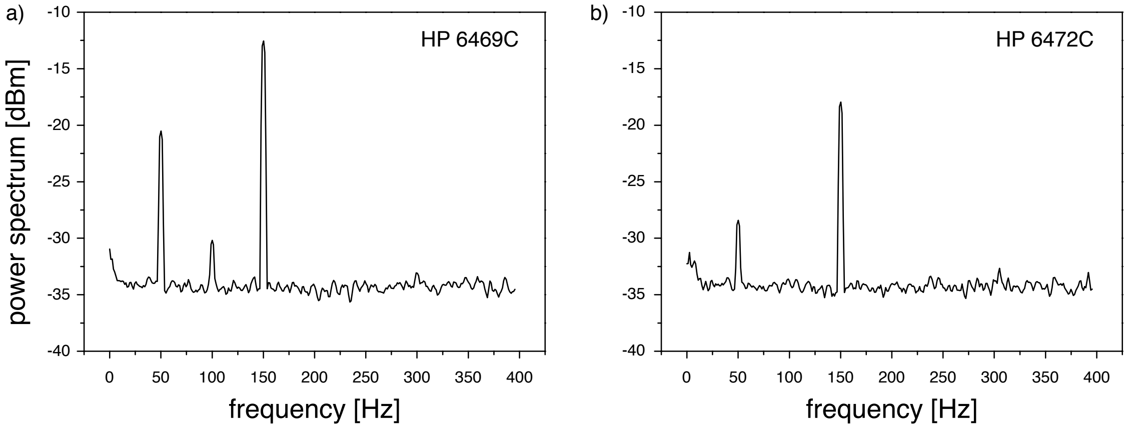

Figure 3.6: Noise characteristics found by connecting a $0.4\,\Omega$ dummy load at the new power supplies. a) HP 6469C, for DC discharge; b) HP 6472C, for filament heating

To be sure the new power supplies do not change substantially the plasma, the profiles of the ion saturation current density at different parameters are measured with the multi-Langmuir probe by using the different sources. The comparison, given in figure 3.7, show no significant difference in the ion saturation current density profiles, hence the plasma density.

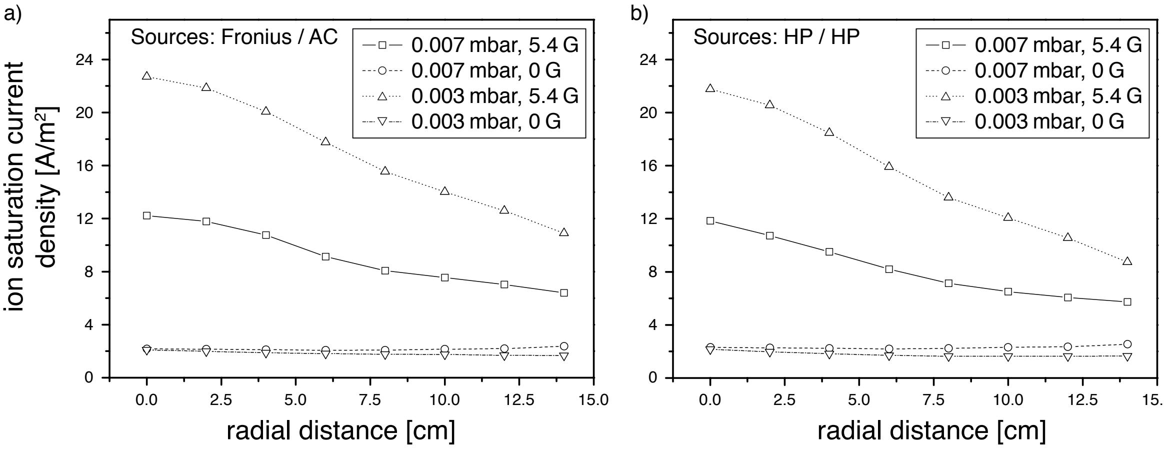

Figure 3.7: Comparison of different ion saturation current profiles found either with the Fronius DPS 400 source and an AC filament current or with the two HP sources. a) Fronius DPS 400 power supply for plasma discharge and AC current for filament; b) HP power supplies for discharge and filament.

3.2 Instability and non-uniformity characterisation

3.2.1 General plasma observations

A very simple method to analyse the different instabilities and non-uniformities is to simply observe the plasma through a window. The parameters defining principally the behaviour of the plasma and its stability are the pressure and the magnetic field. Therefore several characteristics of the different types of plasmas in this parameter space were established. Depending on the two parameters and the use of both coils or only the top coil, six types of plasmas are found: (green) an optically stable and homogeneous plasma, (orange) a weakly unstable, flickering plasma, (red) a strongly unstable, heavily flickering plasma, (violet) a plasma jumping irregularly between different points of attachment on the ring anode, (light blue) a plasma attaching to one of several different points on the anode, showing a bright glow and (blue) a stable but generally dark plasma with bright glows in the view ports or in front of the turbo pump.

The two characteristics shown in figure 3.8 were produced with the ring anode a short time after its construction. The observation shows that there are certain conditions where the plasma is visually stable and axisymmetric. If both coils are used with at least 6–7 A the plasma is stable for most of the pressures used. But the magnetic field in industrial applications uses only the top coil and as can be seen in figure 3.8b this leads to a strongly reduced parameter set producing a stable plasma. For the case of only 5 A in the top coil used in industrial applications, the plasma is unstable in the whole pressure range.

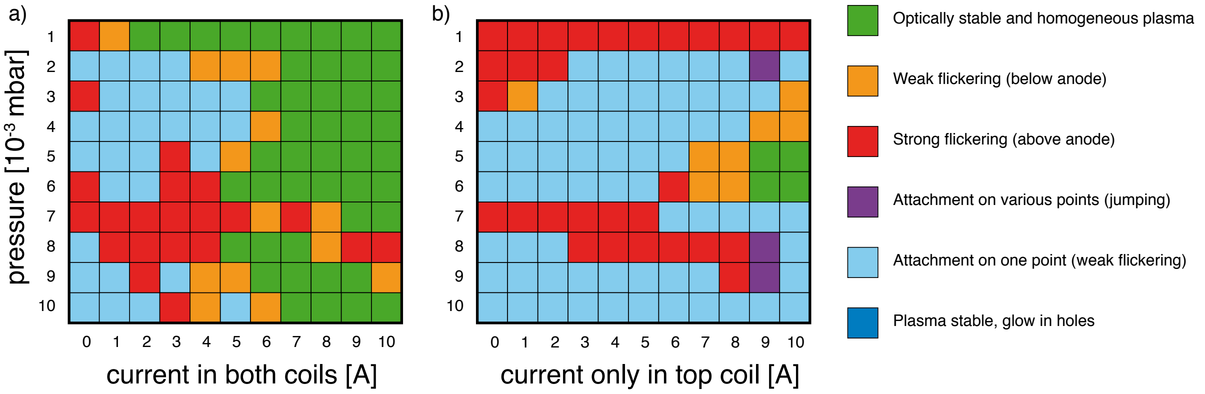

Figure 3.8: Characteristic of different types of instabilities observed with the new circular anode: a) using both coils; b) using only the upper coil for the magnetic field.

This kind of observation was repeated after several hours of operation with the ring anode. In figure 3.9 the new characteristic is presented. Most of the stable conditions now are unstable, preferentially showing an attachment to one point on the anode and even if there are some cases at 0.001 mbar and at 0.01 mbar where the plasma has become stable (figure 3.9b), the overall situation is even worse. So even though in the LEP module only an argon plasma was used, not depositing any material on the anode, the stable and homogeneous conditions found in figure 3.8 are nearly all lost. This supports the apprehension mentioned in section 3.1 about the loss of anode symmetry.

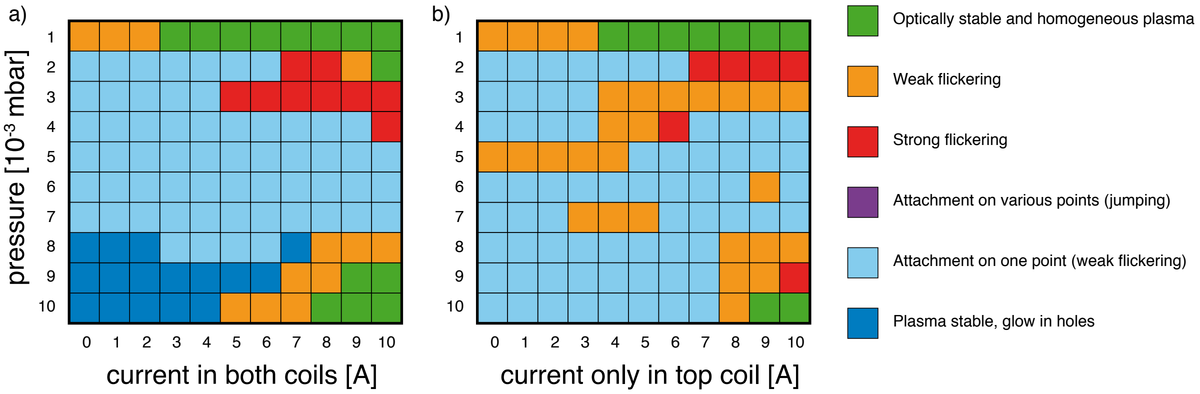

Figure 3.9: Characteristic of different types of instabilities observed after several hours of operation with the circular anode: a) using both coils; b) using only the upper coil for the magnetic field.

3.2.2 50 Hz driving frequency from filament supply and nonlinear effects

Four different probes were used to characterise the noise produced by the 50 Hz AC current of the filament heating: (1) a differential voltage probe measuring the output voltage V_{out} directly at the sources; (2) a 0.1 Ω shunt to measure the total current I_{tot} in the system; (3) a Langmuir probe measuring the floating potential V_{float} of the plasma; and (4) a photo diode measuring the light emitted by the plasma (V_{opt}). In figure 3.10 the electrical circuit of the LEP module and the position of the four probes is shown.

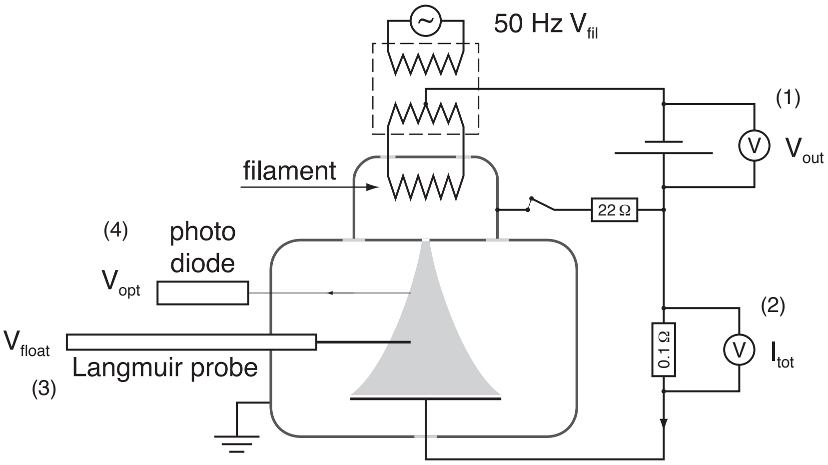

Figure 3.10: Electrical circuit of the LEP module power sources connections and positions of the four probes used to characterise the noise produced by the 50 Hz AC current of the filament heating.

Figure 3.11a shows the noise characteristics of the four measurements found in a plasma with pressure $p = 0.003\,\mathrm{mbar}$, magnetic field $B_{\mathrm{c}} = 5.4\,\mathrm{G}$, and filament current $I_{\mathrm{fil}} = 150\,\mathrm{A_{AC}}$. All probes show peaks at the driving frequency of the filament heating current (50 Hz) and several of its harmonics, which result from nonlinear effects in the plasma. A further but small peak is found with the Langmuir probe at 12.5 Hz. This type of noise will be discussed in detail in the next section.

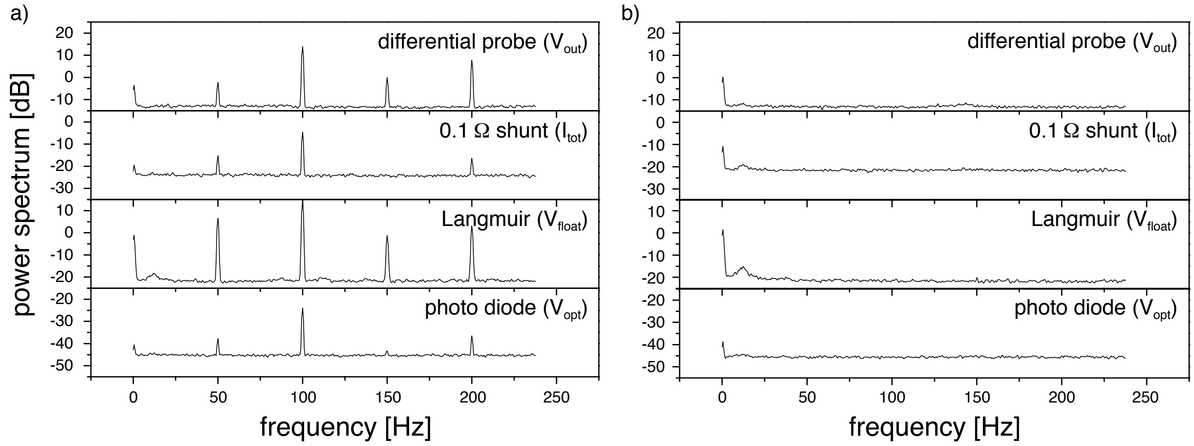

Figure 3.11: Frequency characteristics obtained from four different probes when using an AC or DC filament current, $p = 0.003\,\mathrm{mbar}$, $B_c = 5.4\,\mathrm{G}$. a) $I_{\mathrm{fil}} = 150\,\mathrm{A}_{\mathrm{AC}}$ inducing 50 Hz noise and harmonics; b) $I_{\mathrm{fil}} = 150\,\mathrm{A}_{\mathrm{DC}}$ with HP source.

In figure 3.11b the frequency characteristics, measured when using a DC current from the HP source for the filament heating, are presented. The only peak found again is the one at 12.5 Hz, here also on I_{tot}. Although the HP source shows a small noise of 50 Hz, this oscillation of the DC signal is too weak to be transfered into the plasma.

An uncertainty of the change from AC to DC power supply for the filament heating was the lifetime of the filament. It is known that the plasma current attaches to a certain point on the filament, called hotspot. The position of this hotspot is assumed to vary when applying an AC heating current on the filament. It seemed to be possible that the hotspot sets to a fixed position when a DC heating current is applied instead. This could actually melt the filament locally and therefore decrease the lifetime of the filament.

As the ionisation source holding the heating filament is inaccessible for direct observation, an indirect imaging method was developed. The light emitted by the filament passes trough the hole in the separation plate between ionisation source and reactor chamber, projecting an image of the filament on the Langmuir multi probe. The diameter of this hole is 2 mm, producing a strongly blurred image. Therefore a smaller one with a diameter of 0.5 mm was drilled into the separation plate, producing a second, more focused image, like in a pinhole camera (cf. figure 3.12a). In Figures 3.12b and 3.12c these images are shown, taken without and with a plasma respectively.

Without a plasma the image of the filament has a constant brightness, as a constant DC current is heating the filament. With a plasma however, it was suspected to find find a brighter zone at some point of the image, indicating a substantially stronger local heating of the filament. As the image of the filament together with a plasma is hardly visible, even if different band- and high-pass filters were used to filter the light emitted by the argon plasma (principally at 700–850 nm), since the light from the filament is too

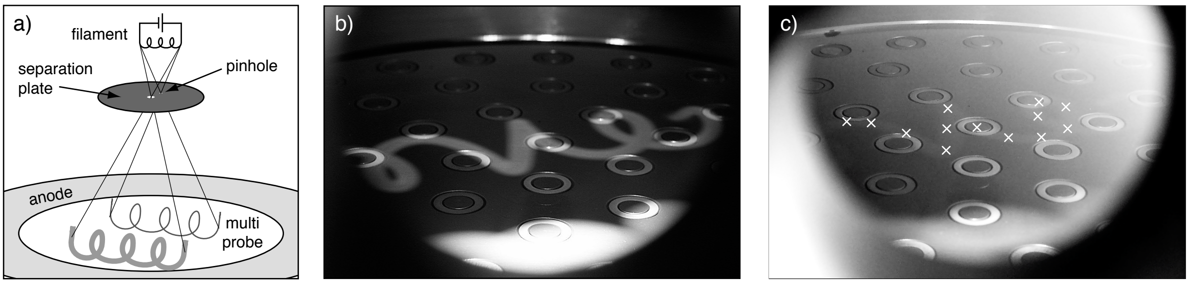

Figure 3.12: a) Schematic of the pinhole system to produce an image of the heating filament. The plate separates ionisation source and reactor chamber; b) filament image without plasma; c) hardly visible filament image with plasma, the white crosses indicate the position of the filament image (exposer time: 2 s).

weak. Figure 3.12c shows an image of the filament, indicated by white crosses, with the plasma switched on and an exposure time of 2 s. The fact that no hotspot is found on the image could have three different reasons: (1) The hotspot is not attaching to one point but moving, (2) the hotspot is attaching to one point but the difference in heating is too weak or (3) the method is not precise enough to find the expected hot spot. (1) and (2) would cause no problems and (3) was finally proven to be wrong, as in practice no significant reduction of the filament lifetime was found.

3.2.3 Subharmonics of driving frequency

As mentioned in the last section, not only higher-order harmonics of the driving frequency peak were found, but also peaks at subharmonic frequencies. Miller et al. [31] and Hayashi

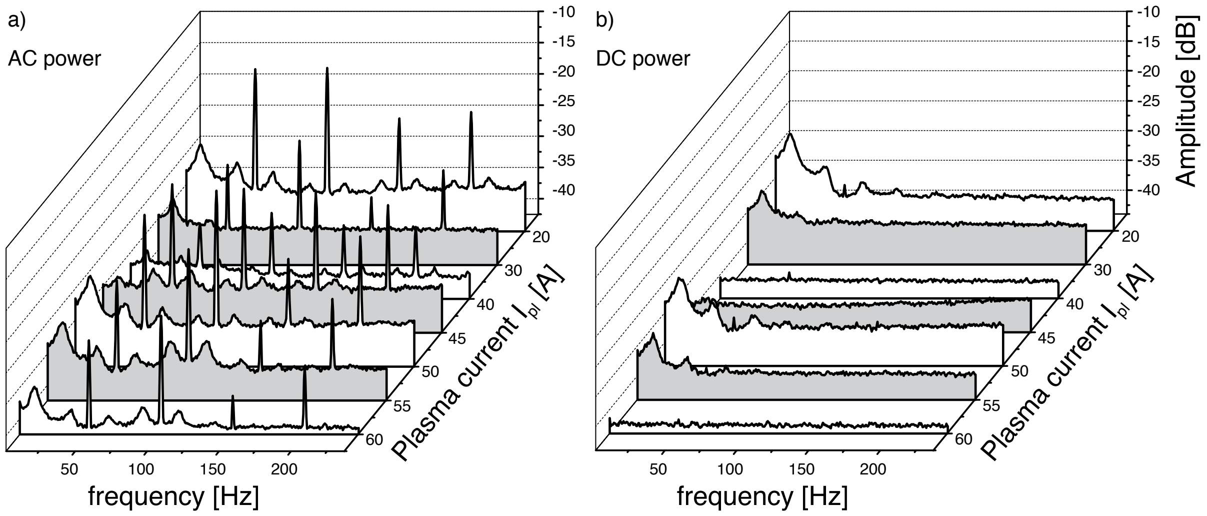

Figure 3.13: Frequency characteristics obtained from floating potential measurements. a) With an AC filament connection, leading to 50 Hz peaks and harmonics; b) with a DC filament connection.

et al. [32] have shown that a plasma, or more general an electrical system, with nonlinear behaviour can show period-multiplying bifurcation. They show that the subharmonics are not considered to be waves but oscillations and that bifurcation can occur at a certain threshold of one or several plasma parameters such as current, pressure or geometry. Mausbach et al. [33] presented different methods to control the chaotic current oscillations arising from bifurcation.

The aim of the noise study presented in this section was to (a) find the source of the subharmonic frequencies and (b) to change the system in order to eliminate them. The frequency spectra given in figure 3.13 are obtained from floating potential measurements with a Langmuir probe. A clear dependency between the plasma current and the appearance of subharmonic signals is not found. An improvement is found by the elimination of the strong 50 Hz noise driven by the AC power of the filament. All the profiles in figure 3.13b show reduced higher-order subharmonics than in figure 3.13a. Nevertheless they could not be eliminated completely.

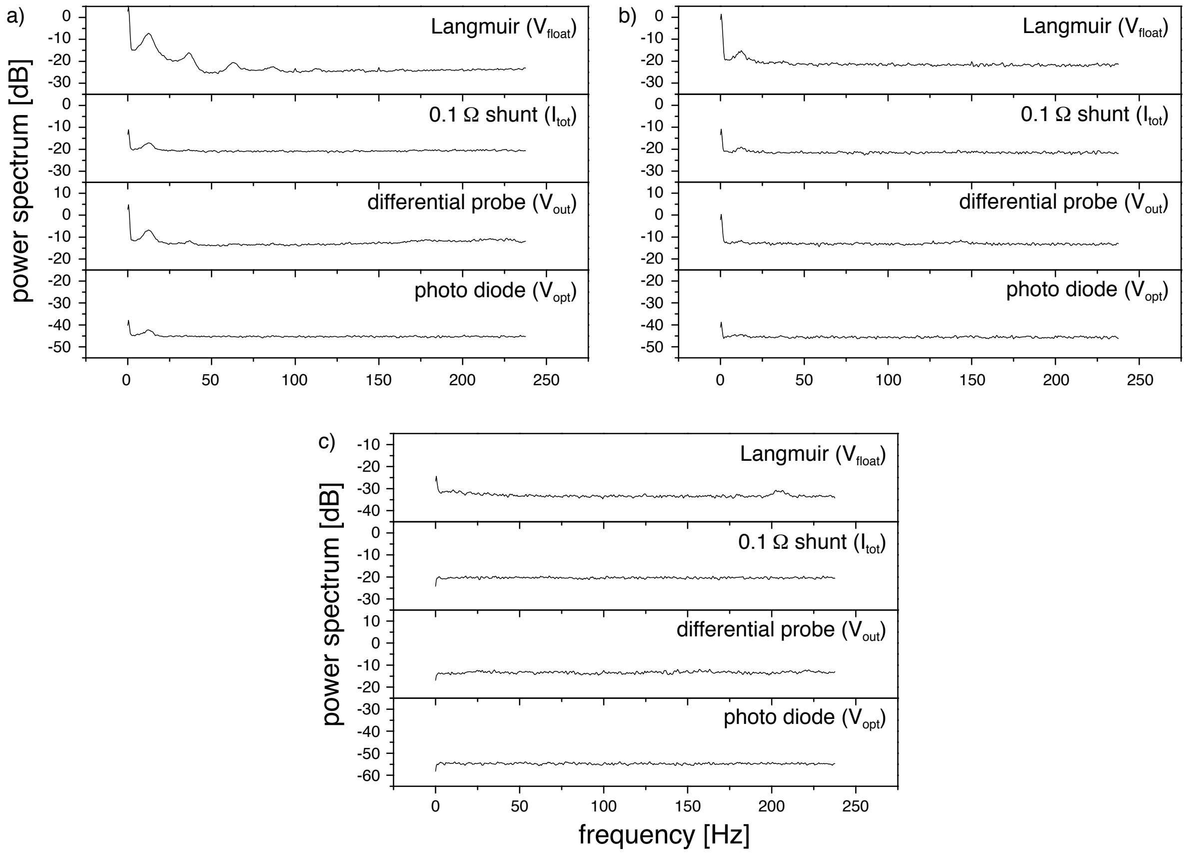

Figure 3.14: Frequency characteristics obtained from four different probes. a) in a strongly flickering plasma (0.007 mbar, 5.4 G); b) in a weakly flickering plasma (0.003 mbar, 5.4 G); c) in an optically stable plasma (0.007 mbar, 0 G).

Plasma current and filament heating current can be eliminated as probable sources of the observed subharmonics. Another potential source is the reactor geometry and the observed flickering presented in section 3.2.1. In figure 3.14 four different frequency measurements made in three different plasma states are shown: a) in a strongly flickering plasma, b) in a weakly flickering plasma and c) in an optically stable plasma. The four types of probes are: 1) a Langmuir probe for the floating potential, 2) a 0.1 Ω shunt for the total current, 3) a differential probe for the output voltage and 4) a photo diode for the optic emission of the plasma. These measurements show clearly a dependence between the observed flickering and the subharmonic signals measured on the different probes.

It seemed to be highly probable that the subharmonic noise and the flickering is related to the geometry of the ring anode. To prove this, the ring anode was replaced by a simple copper cylinder with a diameter of about 2 cm. This new anode was placed vertically in the lower part of the reactor. Here the plasma was optically stable showing no flickering for any parameter set. In figure 3.15 the frequency characteristics of three different probes show no subharmonic noise using either an AC or a DC filament heating current. Only the 50 Hz noise and its harmonics are found again for the case of an AC filament current. This indicates at least a possible relation between the observed instabilities and the use of a circular anode. In the next sections this relation is analysed in more detail.

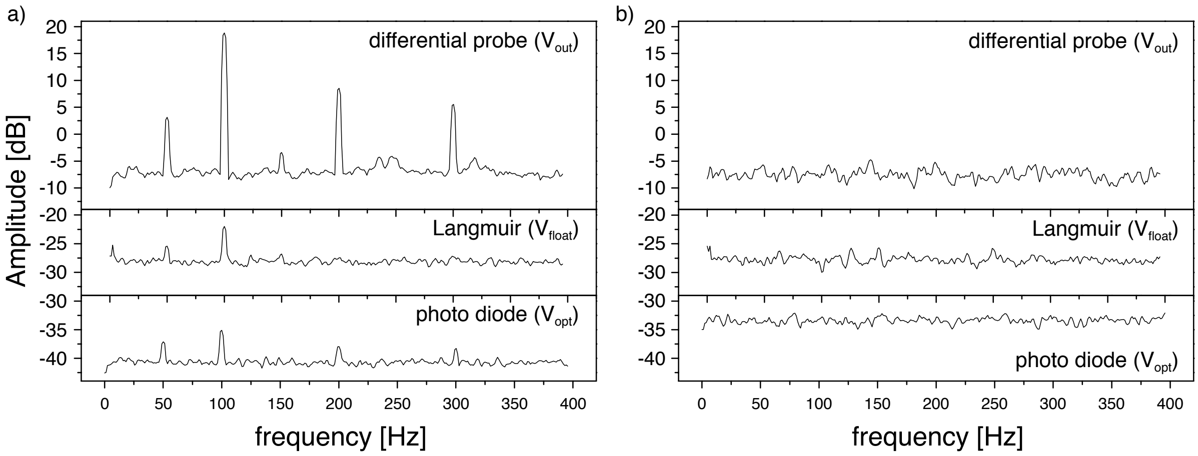

Figure 3.15: Frequency characteristics found when using a copper point anode ($p = 0.003$ mbar, $B_c = 5.4$ G, $I_{fil} = 150$ A). a) With an AC filament current; b) with a DC filament current.

3.2.4 Local plasma attachment on the circular anode

In section 3.2.1 it was shown that after several hours of operation with the ring anode the plasma tended, for most values of pressure and magnetic field, to attach to one of several points of the anode. With ongoing tests the plasma attached preferentially to one of total six points on the anode. In some cases the plasma also flipped from one point to another spontaneously. A rough localisation of these six points is presented in figure 3.16a.

It is assumed that the bright attachment zones of the plasma represent the zones where most of the electrons, transporting the DC plasma current, reach the anode. To analyse if bright glows on the anode correlate completely or at least partially with the DC current path in the reactor, the Hall probe is used to measure the magnetic field induced by the discharge current. In figure 3.16b a schematic view of the current direction and

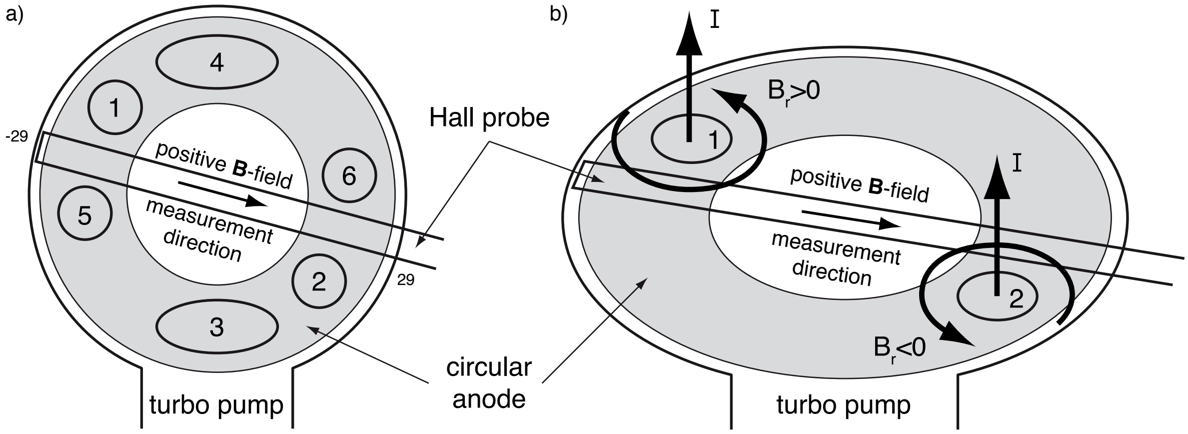

Figure 3.16: a) Schematic top view of the circular anode with the rough localisation of the six points of current attachment. The position of the Hall probe prototype used is indicated; b) Schematic of the current orientation in the plasma hot spots and of the resulting magnetic field. At point 1 the measured B_r is positive, at point 2 B_r is negative.

its induced magnetic field is presented for two different points of attachment. Depending on the location of the attachment point, the radial component of the field measured is positive or negative, and has a variable amplitude depending on the distance between attachment point and Hall probe.

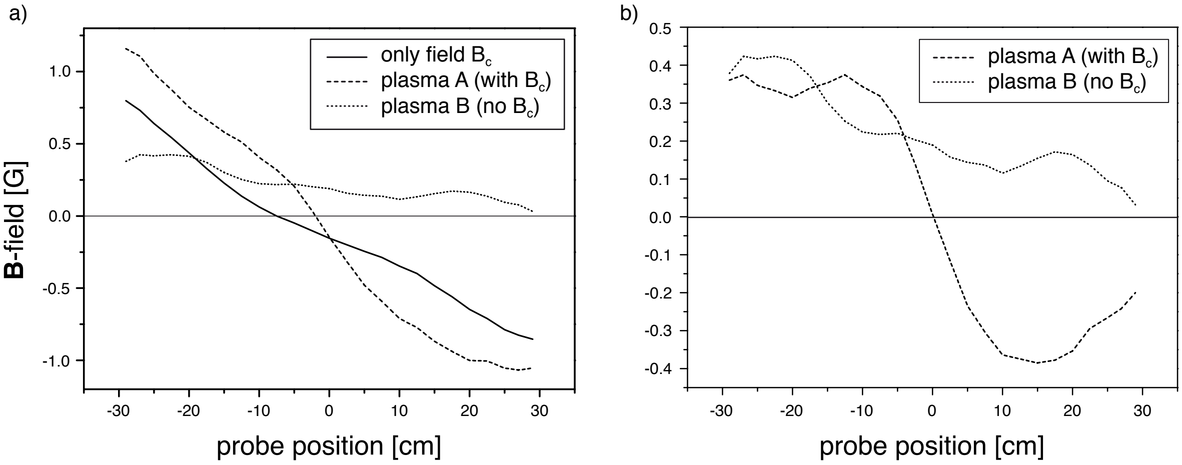

Figure 3.17: Single Hall sensor measurements: a) magnetic field B_r of the Helmholtz coils (—), B_r of plasma A with magnetic field (- - -) and B_r of plasma B without magnetic field (···); b) B_r of plasmas A and B corrected by the offset of the magnetic field.

All measurements presented here are made with the single sensor prototype of the Hall probe presented above and with the following plasma parameters: plasma current $I_\mathrm{pl} = 50\,\mathrm{A}$, filament current $I_\mathrm{fil} = 150\,\mathrm{A}$, pressure $p = [0.001, 0.003, 0.007]\,\mathrm{mbar}$, magnetic field $B_\mathrm{c} = 0$–$5.4\,\mathrm{G}$. A typical measurement is shown in figure 3.17. Plasma A (0.003 mbar, 5.4 G), although with a maximum magnetic field, is not stable and attaches alternatively to points 1 and 2 (cf. figure 3.16a). Considering the direction of magnetic field produced by the plasma current (cf. figure 3.16b), this is in good agreement with the measurement showing a positive signal, hence a magnetic field in the positive measurement direction, near point 1 and a negative signal, hence a magnetic field in the opposite direction, near point 2. Plasma B (0.003 mbar, 0 G) showed a large and stable hot spot at zone 4. This leads to a positive signal all along the Hall probe, hence a magnetic field in the positive measurement direction.

To be sure that the probe itself has no visible effect on the measurements, the above measurements were repeated from the opposite side of the reactor. Therefore the measured profiles of plasmas with the same current distribution as before should be identic, but with opposite sign, as the probe measures in opposite direction. The two profiles presented in figure 3.18a (plasmas C and D) are made with plasmas comparable to plasmas A and B shown in figure 3.17. Only the pressure is higher ($p = 0.007$ mbar) which makes the plasmas more stable. Plasma C showed no flickering and attached completely to point 1. This is confirmed by the single Hall probe measurement, showing a negative signal around point 1, in contrast to the positive signal found around point 1 when measuring from the opposite side (cf. figure 3.16b). The signal is not only of opposite sign compared to plasma A, but as the total current passes through point 1 the absolute maximum value found around -20 cm is also two times higher than the maximum in figure 3.17b.

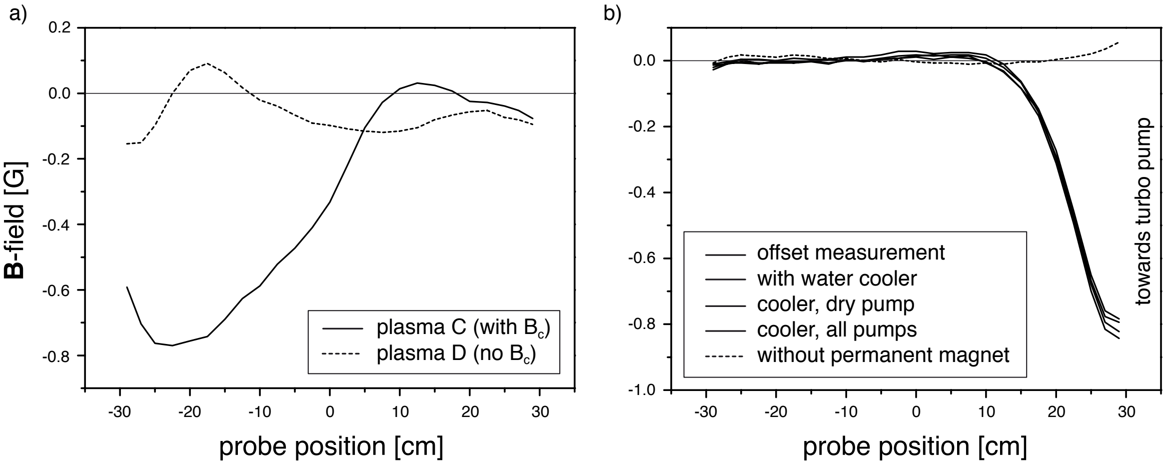

Figure 3.18: Single Hall probe measurements: a) Plasma C (with magnetic field) and plasma D (without) measured from opposite side; b) No effects due to turbo pump levitation or other system components are found. The negative peak is due to a permanent magnet on the outside of the reactor.

Plasma D showed a hot spot at point 5, opposite to point 1. This explains the minor positive peak around -15 cm. But the lack of a confining magnetic field leads to a much weaker signal probably due to a stronger scattering of the electrons in the reactor.

Numerous plasmas without magnetic field attached to point 3 in front of the turbo pump. To exclude probe perturbation effects of the levitation system of the turbo pump, the dry pump or the electric motor of the water cooling system, a magnetic field measurement from the opposite side of the pump was made (probe position 3, cf. figure 1.5).

Figure 3.18b shows four measurements at four different stages of the system. A first offset measurement was made with the whole system switched off. Then one system component after the other was started. It can be seen that none of them changed anything in the measurement. The reason for the negative peak on the side of the turbo pump was a permanent magnet on the outside of the reactor wall.

3.2.5 Simulation of the 2D current distribution with circular anode and comparison with measurements and observations

With the asymmetric distribution of the current due to a local attachment on the circular anode no simple model is available to find the 2D current distribution. The observations of the bright plasma glows on the anode were used for the placing of the current passages in the model. The field simulation software *QuickField* was used to simulate the Hall probe measurements. For this the 2D geometry had to be defined with the appropriate magnetic permeability for the reactor wall and the vacuum part, the position and size of one or more current passages, their corresponding current densities and the desired mesh density around the different elements. The simulated magnetic field can be presented either in a 2D plot with field lines or field strength or by various components along a contour (cf. figure 3.19).

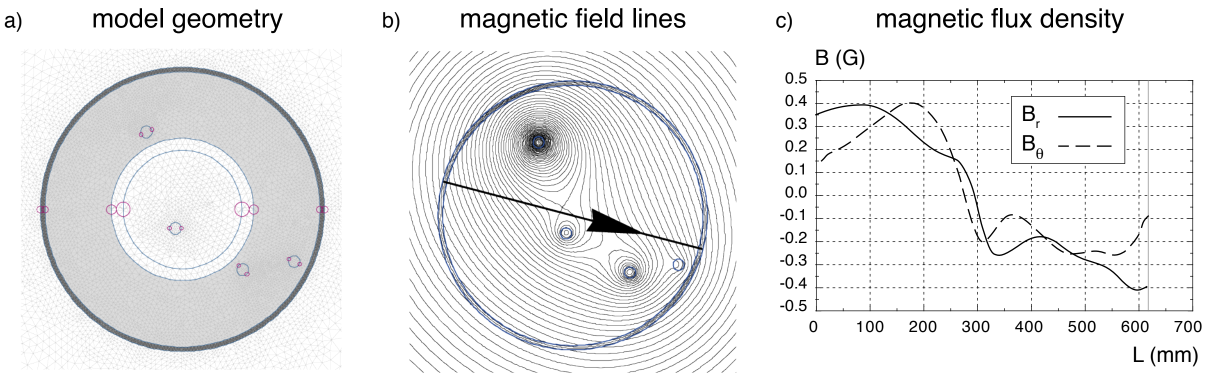

Figure 3.19: QuickField simulation for current profiles of an arbitrary configuration: a) 2D model geometry with reactor wall (dark grey), anode (light grey) and four arbitrary current positions and intensities, the current is positive in out-of-plane direction; b) Magnetic field lines and Hall probe position (flash); c) Radial (B_r) and transversial (B_θ) flux density along the Hall probe position indicated in b).

The components of the simulated magnetic field used to compare with the multi-Hall probe measurements were the radial (B_r) and transversal (B_θ) component of the total field $\mathbf{B}$. For the measurements with the single sensor measurements only the radial component B_r was used.

The observation of the hot spots of plasmas A and B, shown in figure 3.17, were in good agreement with the Hall probe measurements. Using QuickField calculations it can be shown that the total plasma current of 50 A passes through the hot spots. To simulate plasma A two circular current passages with a radius $r = 30\,\mathrm{mm}$ and a constant current

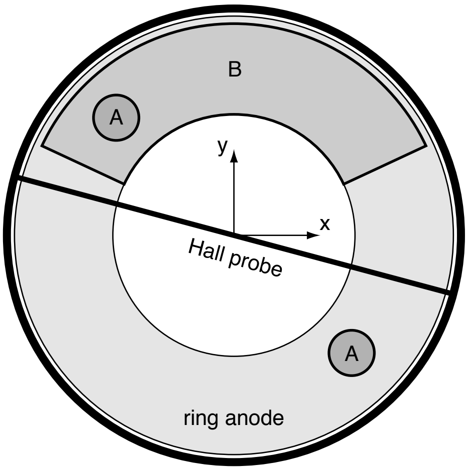

Figure 3.20: Arrangement of current passages on the circular anode. For plasma A two circular passages are used at the positions of hot spots 1 and 2, for plasma B a ring segment passage is used, representing hot spot 4.

density $j = 8.84\,\mathrm{kAm}^{-2}$ were set in the region of points 1 and 2, as indicated in figure 3.20. With this a good fit of the measurements was found (cf. figure 3.21).

As plasma B attached to a large part of the anode, the simulation was done with the section of a ring: outer radius $R_1 = 280\,\mathrm{mm}$, inner radius $R_2 = 160\,\mathrm{mm}$, angle range $\phi = 25°–155°$ and current density $j = 835\,\mathrm{Am}^{-2}$. Again the total current was assumed to pass through this region. As already discussed above for plasma D, the measurement was weaker than expected. Again a part of the current must be diffused in the reactor due to the missing magnetic field from the Helmholtz coils.

The Hall probe measurements can not only be compared to the simulations of the magnetic field but also to saturation current measurements done with the multi-Langmuir probe (cf. section 2.1.2). Figure 3.22 shows the results of a non-confined plasma (0.007 mbar) that attached at point 3 in front of the turbo pump. The hot spot was simulated by a ring segment: $R_1 = 290\,\mathrm{mm}$, $R_2 = 160\,\mathrm{mm}$, $\phi = -30°$ to $-160°$ and $j = 716\,\mathrm{Am}^{-2}$. And as

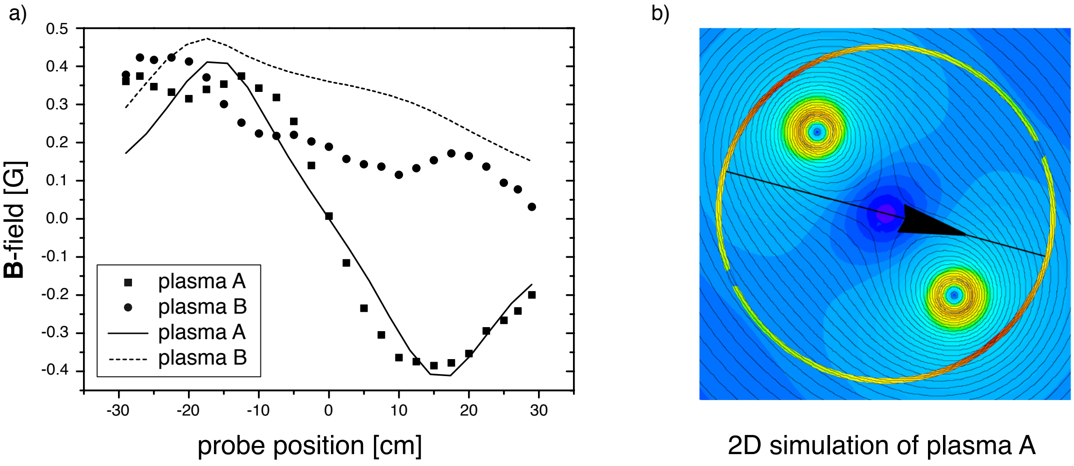

Figure 3.21: a) Measurements (symbols) and simulation (lines) of plasmas 1 and 2; b) 2D simulation with QuickField of two current passages. Distance from reactor center: 190 mm, radius: 30 mm, angular positions: $-50°$ and $130°$ and constant current density: $8840\,\mathrm{Am}^{-2}$

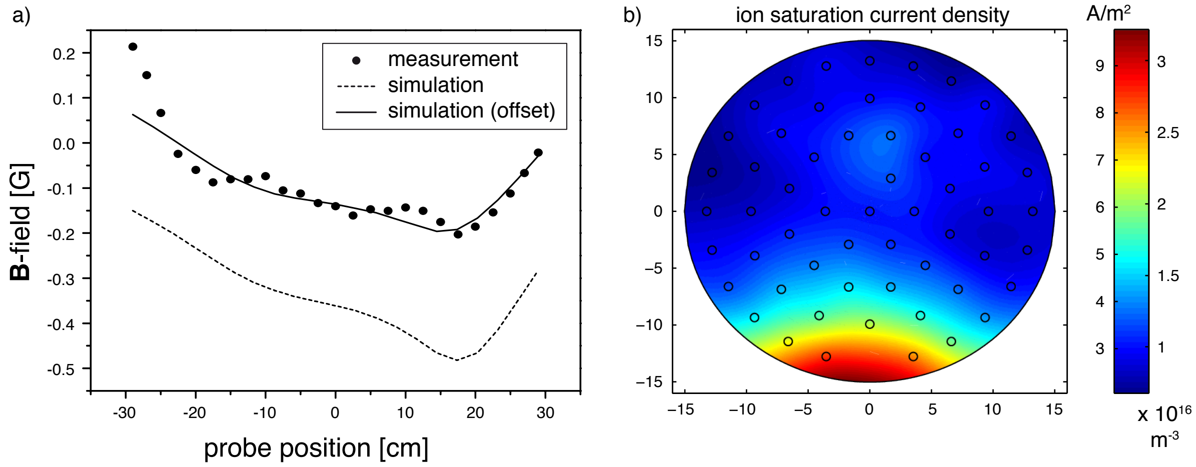

Figure 3.22: a) Hall probe measurements and simulations of a non-confined plasma (0.007 mbar); b) Corresponding multi-Langmuir probe measurements showing a high saturation current in the vicinity of point 3 where the plasma shows a hot spot.

for plasmas 2 and 4 an offset has to be added. The multi-Langmuir probe measurements show, as expected, a high saturation current in the vicinity of the plasma hot spot.

For plasmas with a magnetic field of 5.4 G, it is difficult or even impossible to correlate the Langmuir probe measurements with the Hall probe measurements. The ion saturation current profile depended mainly on the confining magnetic field, leading to profiles similar to those shown in figure 3.1, in contrast to the measurements presented in figure 3.22b. The multi-Langmuir probe measurements show a profile similar to the ones presented in figure 3.1, whereas the Hall probe measurements of the induced magnetic field still show mainly the attachment effects, also observed by eye. In the case of $p = 0.001$ mbar, the

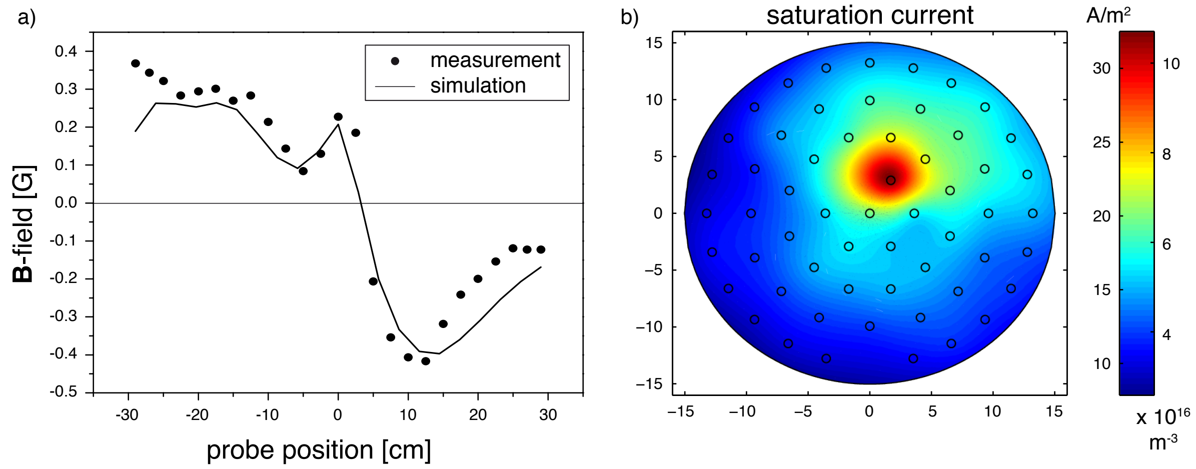

Figure 3.23: a) Hall probe measurement and simulation of a plasma at 0.001 mbar showing a positive peak at 0 cm; b) multi-Langmuir probe measurements showing a strong peak near the centre of the probe due to the fast electron beam directly reaching the probe.

lowest pressure to get a discharge in the reactor, a different behaviour was observed. Here the fast electrons from the source have a mean free path of about 52 cm, which is more than the distance between ionisation source hole and the multi-Langmuir probe ($\approx$ 39 cm). Therefore only a part is lost by radial scattering and the rest of them can be seen with the Hall probe as a peak at 0 cm and also with the Langmuir probe as a strong peak near the centre of the probe (cf. figure 3.23). For the simulation given in figure 3.23a, the position of the peak on the Langmuir probe is used. A current passage is defined at its position with a radius of 12.5 mm and a total current of 8.8 A, the rest of the 50 A total current is set to three other typical positions on the anode.

3.3 Additional cusp field

Takekida et al. [34] have shown in a small cylindrical DC-plasma discharge that a multipolar magnetic field can increase the electron density by a factor of nine. Three effects are found to be important for this: (1) magnetic mirror effect near the cusp of two magnetic poles, (2) suppressed electron diffusion in the direction normal to magnetic field line, and (3) electron repelling in the sheath on the chamber wall.

To verify if a similar effect can be found on the six-times-larger LEP reactor three rows of alternately north and south pole magnets were installed. Because of the observation windows and the turbo pump in the reactor wall the multipolar field was not continuous around the reactor. Figure 3.24a shows the magnetic field from one permanent magnet used for the multipolar field as a function of distance from one magnet. The magnets have dimensions of $3 \times 3\,\text{cm}^2$ and a thickness of 1.5 cm. In the vicinity of the reactor wall the field strength of the multipolar field is about a 100 times stronger than the maximum confining field from the near Helmholtz coils. Figure 3.24b shows two different possible arrangements of the permanent magnets. In black is the arrangement as installed for the measurements and in grey the additional magnets necessary for an optimal confinement.

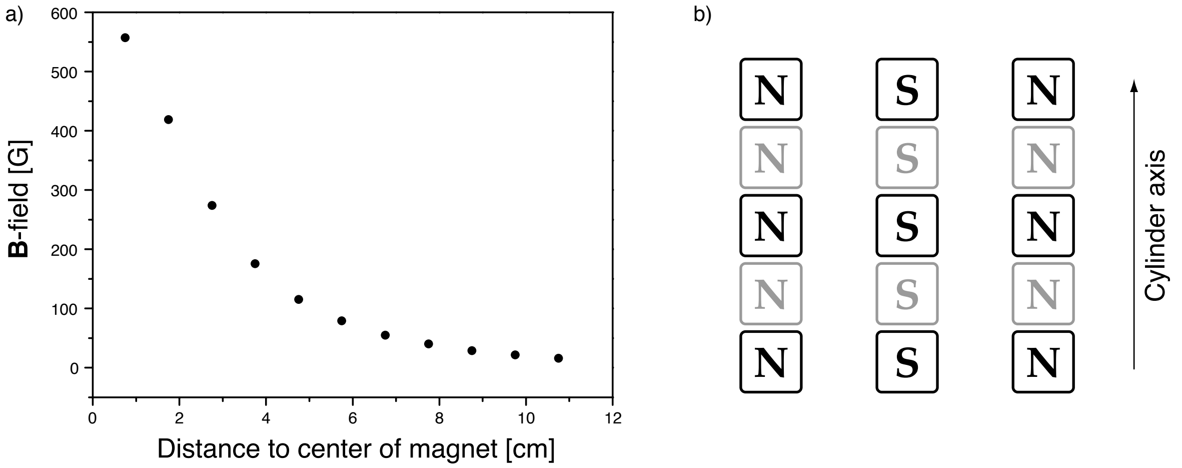

Figure 3.24: a) Magnetic field strength of one permanent magnet depending on the distance to its center; b) in black: arrangement of the three rows of permanent magnets around the reactor; in grey: the additional magnets necessary for an optimal confinement.

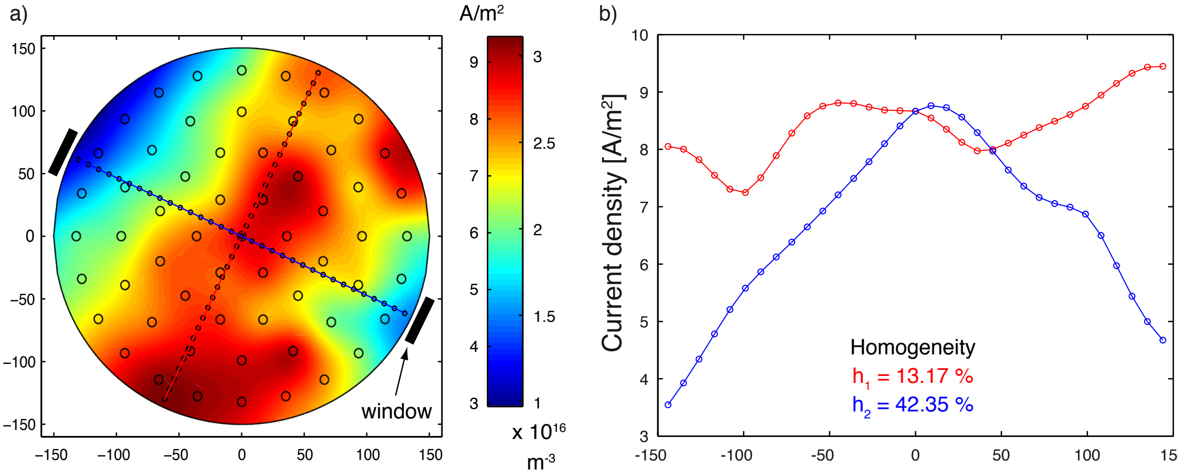

Figure 3.25: a) Multi-Langmuir probe measurements of the plasma density with 2.7 G magnetic field at 0.007 mbar. The multipolar field is interrupted at the position of the two windows; b) Linear profiles along the two windows (blue) and in perpendicular direction (red)

The measurements of the plasma density (cf. figure 3.25) show a significant increase of homogeneity where the multipolar field is uniformly installed. At the two sides where the observation windows make it impossible to install the magnets the plasma density decreases by a factor of two. The measured homogeneity of 13 % is already close to the requirements of certain industrial applications such as solar cells (10 %). But for electronic device applications the necessary uniformity is only 2 % as the device size is continually reduced. This would probably necessitate further improvements in geometry and plasma process.

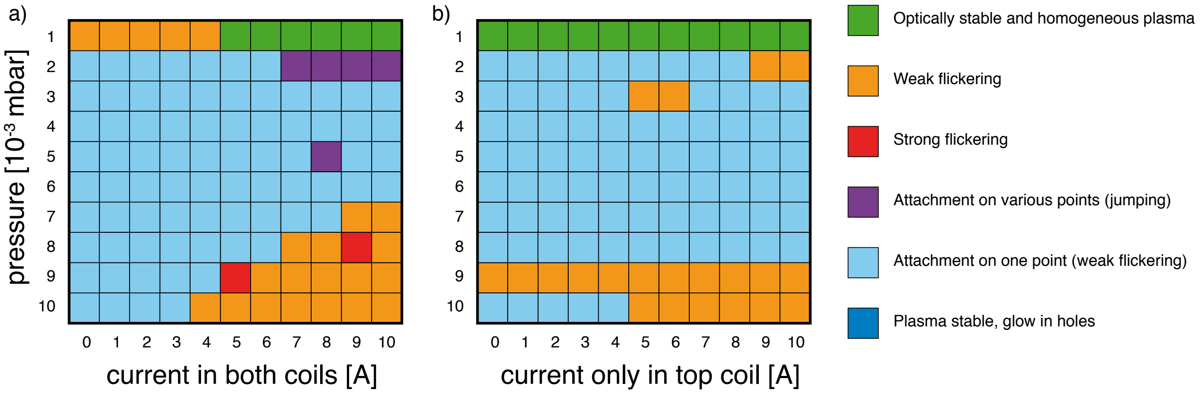

Figure 3.26: Characteristic of different types of instabilities observed with an applied cusp field: a) using both coils; b) using only the upper coil for the magnetic field.

Even though this measurement looked very promising the problem of the plasma attaching on various points did not disappear with the cusp field. A characteristic of the plasma instabilities with the cusp field (figure 3.26) show only small differences compared to the characteristic shown in figure 3.9. The total number of parameter pairs leading the plasma to attach on a single point of the anode is even increased.

As the reactor was only used with non-depositing argon plasmas, this problem is likely to be even worse when using silane or other reactive gases which deposit different type of materials everywhere in the reactor. It was tried to reverse this effect of local attachment by milling the top surface of the anode. But even by removing 1 mm of material the plasma still tended to attach to the same 3–4 points.

3.4 Conclusions on the ring anode configuration

The circular anode is an equipotential surface, but the plasma has no reason to spread out uniformly to give a uniform current density around the whole ring perimeter. The schematic of the plasma, as given in figure 1.1, is purely wishful thinking by the designer of the circular anode configuration. With hindsight it is clear that such a plasma will always be unstable due to several first order effects such as plasma source instabilities, material deposits or the irregular positioning of view ports and the pumping system. These instabilities, leading to local plasma attachment on random points of the anode, can not be controlled with a static magnetic field. The only way to overcome these problems is the installation of the dynamic wobbler field. Therefore, the decision was made to abandon the circular anode configuration and to come back to the geometry of the older generation BAI reactors. For this, a conical anode in the lower centre of the reactor and two larger Helmholtz coils were installed as mentioned in section 1.1.1.

Chapter 4

Characterisation of the columnar plasma

In chapter 3 the various instabilities found with the circular anode have been discussed. To avoid these problems the reactor underwent two fundamental changes. The first was to replace the circular anode by a conical point anode and the second was to change the Helmholtz coils to get a maximum magnetic field of 45 G. In this configuration the reactor is similar to the older BAI 730 D reactor from Balzers.

In this chapter the results of three different types of measurements of the columnar plasma are presented: (1) Single and multi-Langmuir probe measurements to find the electron density distribution, (2) multi-Hall probe measurements to find the current density profiles of the plasma column and to estimate the electron temperature in the plasma and (3) optical emission spectroscopy (OES) measurements to analyse the plasma species inside and outside the plasma column and to characterise the high dissociation efficiency of the plasma.

4.1 Point anode with weak magnetic field

Changing the UHV module to a conical anode configuration (cf. section 1.1.1) leads to an important change of the plasma shape and parameters. In figure 4.1 plasma density measurements, made at probe position b (cf. figure 1.5), are shown. The plasma used has a gas pressure of 0.003 mbar and a discharge current of 50 A. In the case without a magnetic field ($B_c = 0\,\mathrm{G}$) the measurements show a high density plasma close to the anode. This is in good accordance with optical observation as a bright plasma glow can be seen around the anode but no plasma column can be observed. By increasing the magnetic field the plasma becomes more and more confined in a columnar shape.

Beside the magnetic field, the pressure is an additional parameter to modify the behaviour of the plasma. In figure 4.2 the plasma density measurements at three different pressures are presented. By increasing the pressure the primary electrons coming from the source are lost by scattering in a shorter distance from the source. This leads to a decrease of plasma density from bottom to top. At 0.003 mbar the highest density is found around the anode, at 0.007 mbar the highest density is found at the top of the probe, about 15 cm

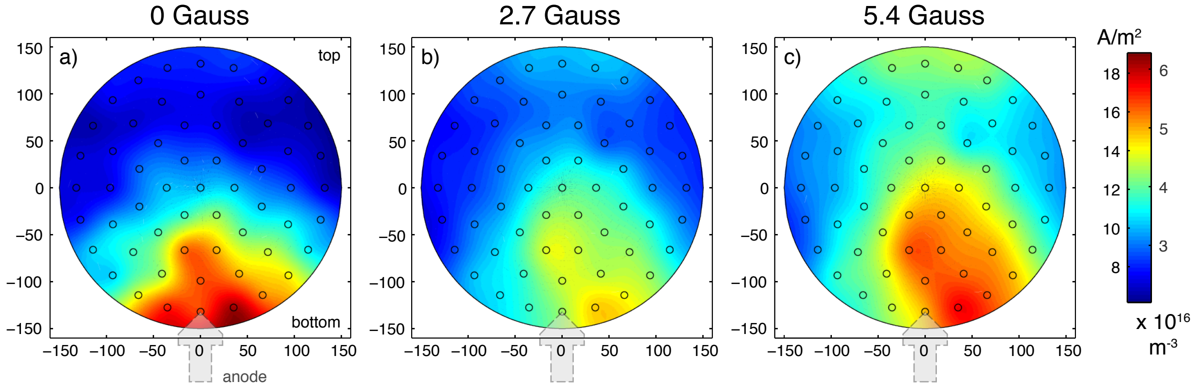

Figure 4.1: Plasma density measurements with the vertically oriented multi-Langmuir probe at different magnetic fields. $p = 0.003\,\mathrm{mbar}$ and $I_{\mathrm{pl}} = 50\,\mathrm{A}$.

below the source and at 0.01 mbar the primary electrons are mostly lost already in the top zone of the reactor.

These measurements show that the plasma has not yet a columnar shape despite the conical anode. For this the magnetic field has to be increased by one order of magnitude in order to have the same plasma configuration as in the BAI reactor.

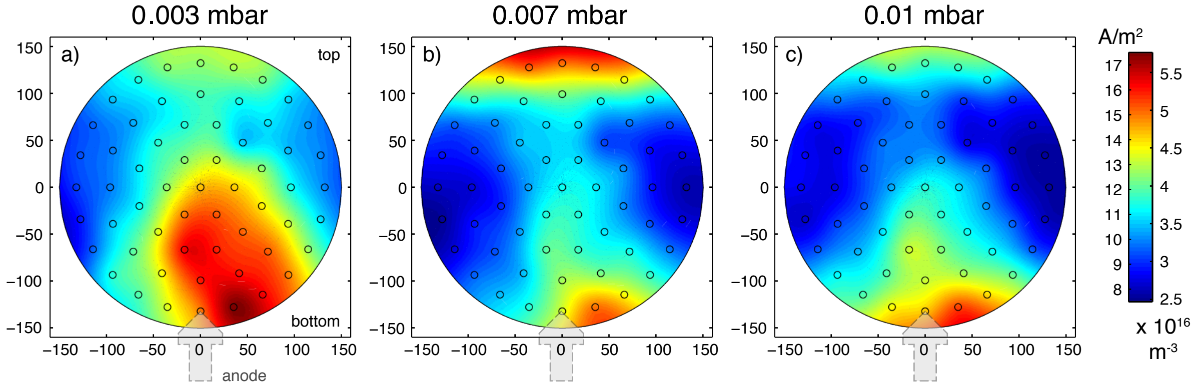

Figure 4.2: Plasma density measurements with the vertically oriented multi-Langmuir probe at different pressures. $B_{\mathrm{c}} = 5.4\,\mathrm{G}$ and $I_{\mathrm{pl}} = 50\,\mathrm{A}$.

4.2 Current density profiles in a DC plasma column

With a point anode and a magnetic field of 45 G a plasma column with an axisymmetric current density profile $\mathbf{j}(r)$ is expected to be found. Using Ampère's law of Maxwell's equations a relation between the measured magnetic field $\mathbf{B}$ and the current density $\mathbf{j}$ is found:

$$\operatorname{rot} \mathbf{B} = \mu_0 \mathbf{j} \tag{4.1}$$

where $\mathbf{B} = (B_\mathrm{r},\, B_\theta,\, B_\mathrm{z})$ and $\mathbf{j} = (j_\mathrm{r},\, 0,\, j_\mathrm{z})$ only depend on r and z as the current density is supposed to be axisymmetric. With $j_\theta = 0$ and the definition for the rotational in cylindrical coordinates

$$\mathrm{rot}\,\mathbf{B} = \left(\frac{1}{r}\frac{\partial B_\mathrm{z}}{\partial \theta} - \frac{\partial B_\theta}{\partial z}\right)\mathbf{e}_\mathrm{r} + \left(\frac{\partial B_\mathrm{r}}{\partial z} - \frac{\partial B_\mathrm{z}}{\partial r}\right)\mathbf{e}_\theta + \frac{1}{r}\left(\frac{\partial (rB_\theta)}{\partial r} - \frac{\partial B_\mathrm{r}}{\partial \theta}\right)\mathbf{e}_\mathrm{z},$$

equation 4.1 for the current density can be written as:

$$\mathbf{j} = \frac{1}{\mu_0}\left[-\frac{\partial B_\theta}{\partial z}\mathbf{e}_\mathrm{r} + \left(\frac{\partial B_\mathrm{r}}{\partial z} - \frac{\partial B_\mathrm{z}}{\partial r}\right)\mathbf{e}_\theta + \frac{1}{r}\frac{\partial (rB_\theta)}{\partial r}\mathbf{e}_\mathrm{z}\right].$$

A second assumption is to define $\mathbf{j} \approx j_\mathrm{z}(r)\mathbf{e}_\mathrm{z}$, as the variations along the vertical axis are small. Therefore the induced magnetic field becomes $\mathbf{B} \approx B_\theta(r)\mathbf{e}_\theta$ and the derivations along z as well as the term with B_z can be neglected. This leads to the final expression for the current density:

$$j_\mathrm{z}(r)\mathbf{e}_\mathrm{z} = \frac{1}{\mu_0}\left(\frac{dB_\theta(r)}{dr} + \frac{B_\theta(r)}{r}\right)\mathbf{e}_\mathrm{z}. \tag{4.2}$$

The results presented in this section are obtained with the multi-Hall probe as presented in section 2.1.3. As it includes only 8 transversally oriented sensors, the measurement is repeated 15 times with steps of 5 mm between each acquisition in order to get a high resolution measurement profile. The measurements, made in a highly confined plasma ($B_\mathrm{c} = 45\,\mathrm{G}$) in probe position 1 (cf. figure 1.5) and with the probe set inside the plasma column, are presented in figure 4.3a. Using equation 4.2 the current density profile is calculated numerically from the measured B_θ as shown in figure 4.3b.

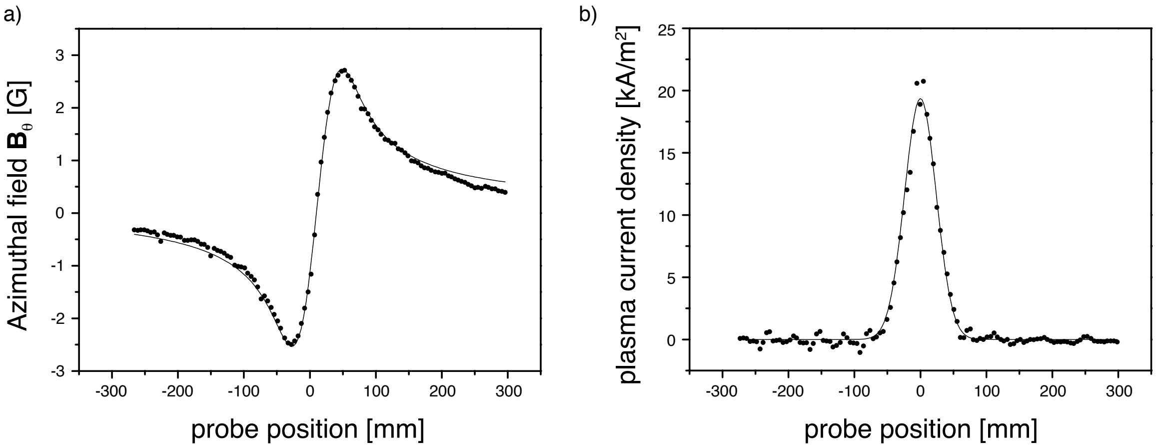

Figure 4.3: a) Magnetic field measurement (···) and fit using equation 4.3 (—) of the azimuthal magnetic field; b) Numerically calculated current density profile (···) and assumed Gaussian fit (—). The plasma parameters are: $p = 0.01\,\mathrm{mbar}$, $I_\mathrm{pl} = 70\,\mathrm{A}$ and $B_\mathrm{c} = 45\,\mathrm{G}$.

Having a total current in the plasma of $I_\mathrm{pl} = 70\,\mathrm{A}$, the current density was fitted with a Gaussian of fixed amplitude J

$$j_\mathrm{z}(r) = Je^{-\frac{r^2}{2w^2}}$$

which leads to a total current of

$$I = \int_0^{2\pi}\int_0^{\infty} J e^{-\frac{r^2}{2w^2}} r\,dr\,d\phi = 2\pi J w^2.$$

The fit of the Gaussian leads to $w = 23.99 \pm 0.13\,\mathrm{mm}$ and to an amplitude of $J = 19'360 \pm 210\,\mathrm{Am^{-2}}$. The function representing B_θ is then found as

$$B_\theta(r) = \frac{B}{r}\left(1 - e^{-\frac{r^2}{2w^2}}\right). \tag{4.3}$$

Introducing B_θ into equation 4.2 leads to a Gaussian distribution for the current density

$$j_z(r) = \frac{1}{\mu_0}\left(\frac{B}{w^2} e^{-\frac{r^2}{2w^2}}\right). \tag{4.4}$$

The amplitude of B_θ is found as $B = \mu_0 J w^2 = 2 \times 10^{-7} I\ \mathrm{m\,kg\,A^{-2}\,s^{-2}} = 140 \pm 3\,\mathrm{Gmm} = (1.40 \pm 0.03) \times 10^{-5}\,\mathrm{Tm}$. The interpolation of the current density peak and the found function for B_θ are shown in figure 4.3.

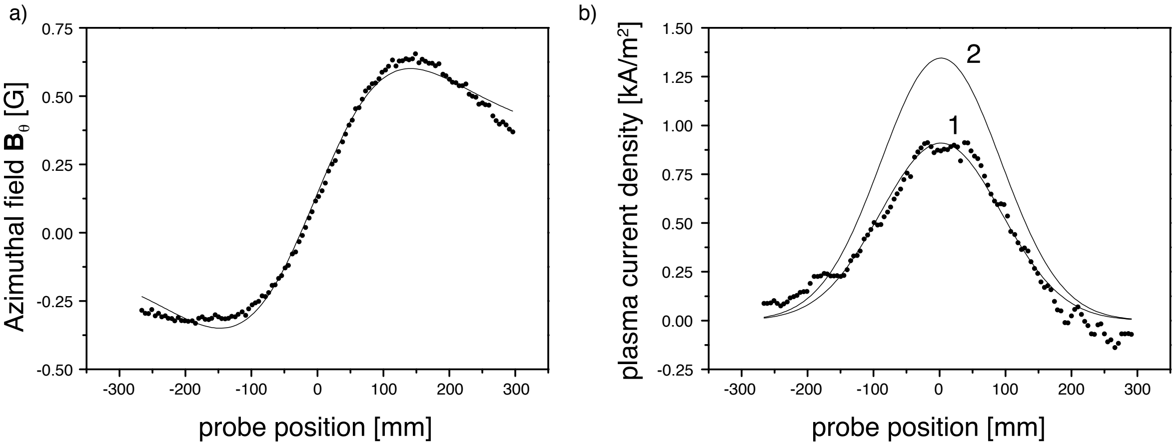

Figure 4.4: a) High spatial resolution measurement and fit of the azimuthal magnetic field; b) Numerically calculated current density profile and assumed Gaussian fit. Curve 1 is the fitted profile and curve 2 the expected profile without current loss. The plasma parameters are: $p = 0.01\,\mathrm{mbar}$, $I_{\mathrm{pl}} = 70\,\mathrm{A}$ and $B_{\mathrm{c}} = 0\,\mathrm{G}$

Switching off the magnetic field the current density profile is expected to become very large as the plasma loses completely its columnar shape at the height where the measurements are performed. The integrated total current should still be equal to the applied discharge current $I_{\mathrm{pl}} = 70\,\mathrm{A}$. Figure 4.4a shows the Hall probe measurements of a plasma without magnetic field and at $p = 0.01\,\mathrm{mbar}$. The calculated current density profile is shown in figure 4.4b. The profile shows that the plasma still has a columnar shape but much wider than before. In the same figure the two curves 1 and 2 are given. The fitting with $j_z(r)$ given in equation 4.4 leads to $w = 91.11 \pm 1.30\,\mathrm{mm}$ and a total current of $I_{\mathrm{pl}} = 48\,\mathrm{A}$ (curve 1). This means that without magnetic field an important loss of the discharge current in the reactor is found. As the total current is controlled by the power source, this must be explained by a current flowing through the reactor wall. Curve 2 shows the expected interpolation with a total current of $I_{\mathrm{pl}} = 70\,\mathrm{A}$.

The same measurements were repeated in probe position 2 (cf. figure 1.5), closer to the source. Figure 4.5 shows the current density profiles found for a plasma with and without magnetic field. The values found for the width of the plasma column are $w_{45\mathrm{G}} = 17.64 \pm 0.12\,\mathrm{mm}$ and $w_{0\mathrm{G}} = 42.43 \pm 0.34\,\mathrm{mm}$. The integration of the profile again gives a total current of 70 A for the confined plasma and a current of only 48 A in the not confined case. Comparing these two profiles with the ones measured at position 1 shows that the plasma column expands from the source orifice towards the anode due to radial scattering of the primary electrons.

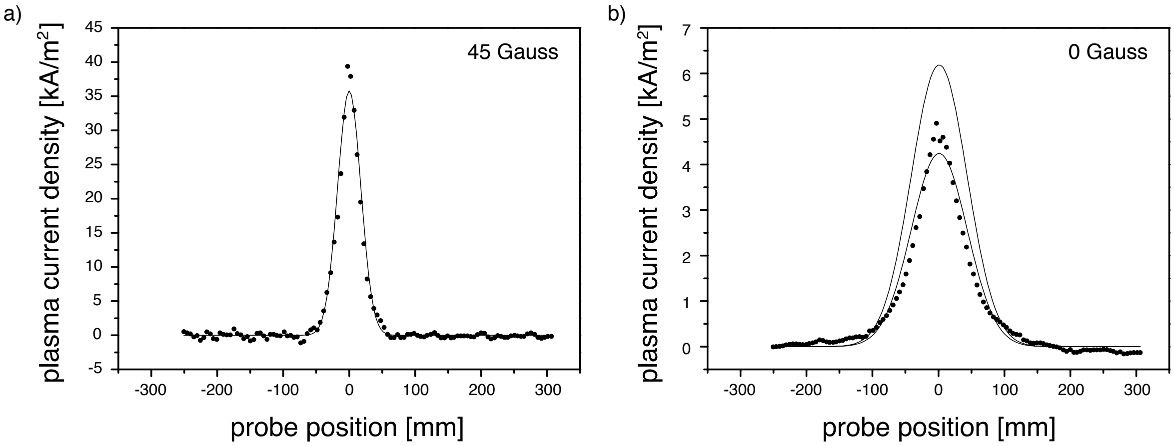

Figure 4.5: Plasma current density profiles in the upper part of the reactor: a) with magnetic field (45 G) ; b) without magnetic field (0 G). The other plasma parameters are: $p = 0.01\,\mathrm{mbar}$ and $I_{\mathrm{pl}} = 70\,\mathrm{A}$

Current density profiles at different angular probe positions

The rotatable vacuum feedthrough is used to measure five current density profiles at different angles. This to check if the probe placed into the plasma column could be perturbing the plasma current density profile. The azimuthal magnetic field given in equation 4.3 has to be rewritten to fit the measurements made at variable angles. The magnetic field due to the assumed plasma profile in the horizontal plane is given by

$$\mathbf{B}(r) = B_\theta(r)\mathbf{e}_\theta = \frac{B}{r}\left(1 - e^{-\frac{r^2}{2w^2}}\right)\mathbf{e}_\theta,$$

with $\mathbf{e}_\theta$ the azimuthal direction (cf. figure 4.6a). The field, defined in polar coordinates, is then transformed into a field given in cartesian coordinates x and y. This is necessary to make a translation of the origin by the distance d between the reactor center and the rotated probe, as shown in figure 4.6a.

By doing this origin translation the x and y components of the magnetic field $\mathbf{B} = (B_{\mathrm{x}}, B_{\mathrm{y}})$ can be compared with the measurements of longitudinal and transversal sensors

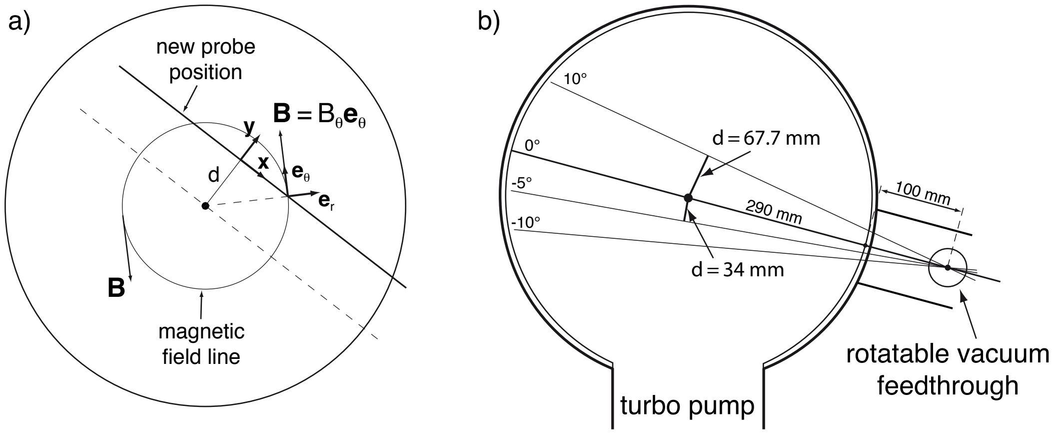

Figure 4.6: a) Linear transformation of the reference system for different angular positions of the probe; b) Schematic of the probe positions accessible ($-10°$ to $10°$) with the rotatable vacuum feedthrough

in the case of an angle different than zero. B_{x} corresponds to B_{long}, measured in longitudinal direction, and B_{y} corresponds to B_{trans}, measured in the transversal direction. The transformed field is found as

$$B_\theta(x,y)\mathbf{e}_\theta = \frac{B}{\sqrt{x^2+y^2}}\left(1-e^{-\frac{x^2+y^2}{2w^2}}\right)\left(\frac{-y}{\sqrt{x^2+y^2}}\mathbf{e}_{\mathrm{x}} + \frac{x}{\sqrt{x^2+y^2}}\mathbf{e}_{\mathrm{y}}\right). \qquad (4.5)$$

With the assumption of an axisymmetric plasma current distribution, the Hall probe direction equal to the x-direction and a given angle of probe rotation, the distance of the probe to the reactor axis can be calculated and set as the constant y-value d, shown in figure 4.6b. Thus the longitudinal and transversal components of $B_\theta \mathbf{e}_\theta$ measured with the multi-Hall probe are found from equation 4.5 as

$$\begin{aligned} B_{\mathrm{long}}(x,d)\,\mathbf{e}_{\mathrm{x}} &= \frac{-Bd}{x^2+d^2}\left(1-e^{-\frac{x^2+d^2}{2w^2}}\right)\mathbf{e}_{\mathrm{x}} \\ B_{\mathrm{trans}}(x,d)\,\mathbf{e}_{\mathrm{y}} &= \frac{Bx}{x^2+d^2}\left(1-e^{-\frac{x^2+d^2}{2w^2}}\right)\mathbf{e}_{\mathrm{y}} \end{aligned}$$

The vacuum feedthrough for the multi-Hall probe allows angles of measurement from $-10°$ to $10°$ (cf. figure 4.6b). Figure 4.7a shows the measurements of longitudinal magnetic field for five different angles and the corresponding fits, in a plasma with $p = 0.01\,\mathrm{mbar}$, $I_{\mathrm{pl}} = 70\,\mathrm{A}$ and $B_{\mathrm{c}} = 45\,\mathrm{G}$. The fitted curves are found with the same values for the amplitude B and the peak width w as used for the fit in figure 4.3, measured in a plasma with same parameters. The calculated plasma current density profile using the given parameters is presented in figure 4.7b.

With the multi-Hall probe at 0° the longitudinal field B_{long}, corresponding to the radial field component, is theoretically equal to zero for an axisymmetric current distribution. The found peak is fitted with a function $B_{\mathrm{long}}(x,d)$ rotated by about 0.5°. This slight shift can be explained either by the difficulty of a correct positioning of the probe or by a slight

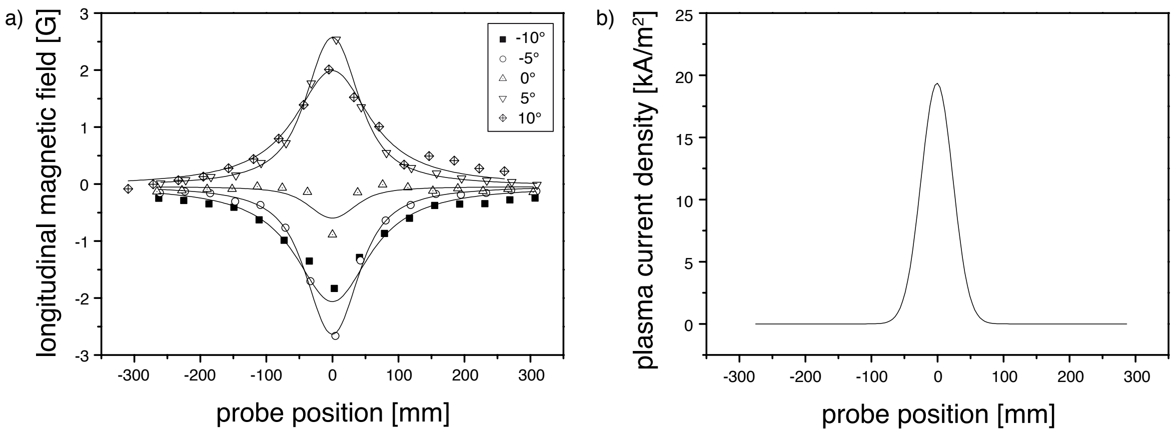

Figure 4.7: a) Measurements in longitudinal direction for five different angles; b) Current density profile calculated from found fitting parameters. The plasma parameters are: $p = 0.01\,\mathrm{mbar}$, $I_{\mathrm{pl}} = 70\,\mathrm{A}$ and $B_{\mathrm{c}} = 45\,\mathrm{G}$

non-symmetry of the plasma due to the disturbance of the probe placed directly in the plasma. The photos in figure 4.8 show the difference between plasmas with and without having the multi-Hall probe placed in it. In (a) and (b) a shadow is observed underneath the probe whereas (c) shows the unperturbed column. Nevertheless, the good fit of the measurements at angles different than zero using the same parameters as for the fit of the azimuthal field measured in the column shows that the current density profile is not perturbed by the probe. Apparently the only part of the plasma perturbed by the probe are the hot primary electrons responsible for a major part of the plasma light emission.

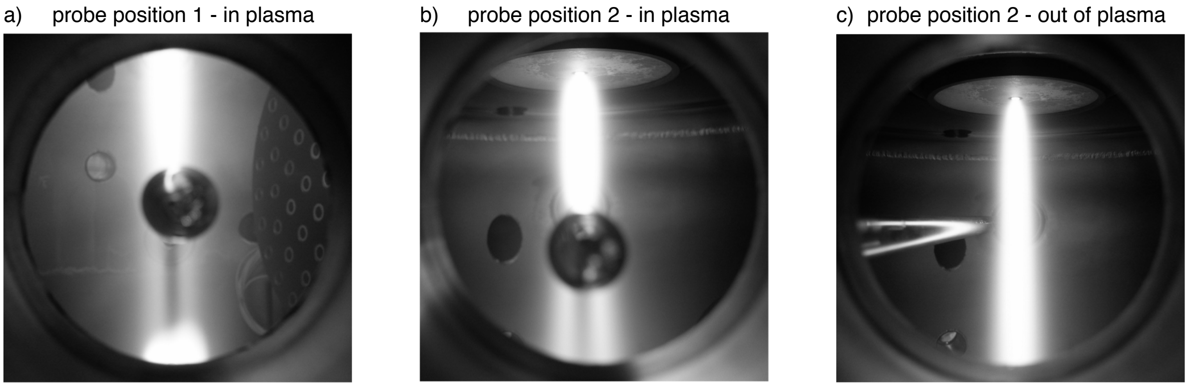
a) probe position 1 - in plasma

b) probe position 2 - in plasma

c) probe position 2 - out of plasma

Figure 4.8: Perturbation of the plasma column due to the multi-Hall probe: a) probe in position 1 placed into the plasma; b) probe in position 2 placed into the plasma; and c) probe in position 2 moved to the side, out of the plasma, by an angle of 10°.

As the hottest electrons are responsible for the measured floating potential, the perturbation of the plasma column observed visually can also be seen on the central V_{f} measurements shown in figure 4.9a made with a Langmuir probe. A potential difference of 3–5 V is found when measuring V_{f} at position 1 and placing the Hall probe in the plasma column as shown in figure 4.8b.

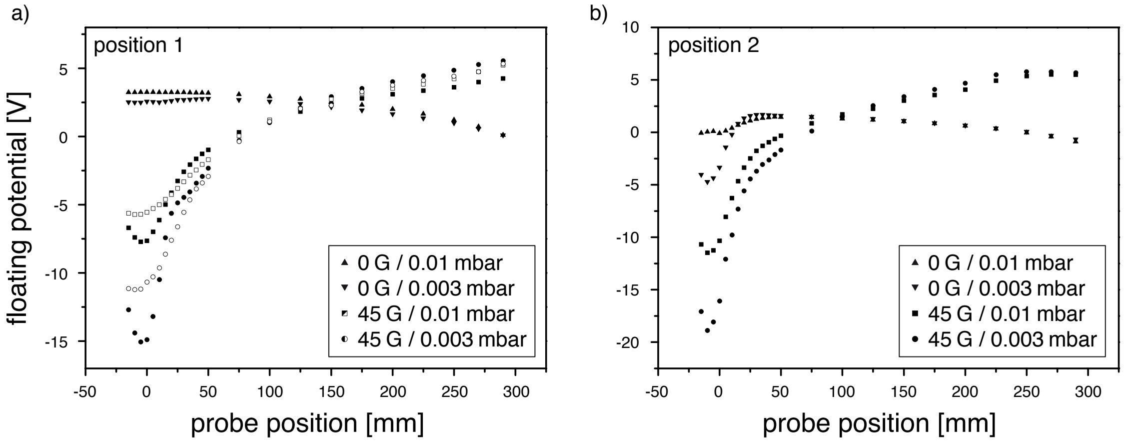

Figure 4.9: Floating potential measurements with a Langmuir probe. a) in position 1, empty symbols represent measurements with a plasma screened by the Hall probe at position 2; b) in position 2, without the Hall probe.

4.2.1 Estimation of the electron temperature from j_z and j_isat

In this section an estimation of the electron temperature T_e will be presented by using the above shown measurements of current density j_z and measurements of the ion saturation current density j_isat. The Ohm's law and a simplified function for the electron collision rate constant $K(T_\mathrm{e})$ leads to a simple relation between the electron temperature T_e on one side and the ion saturation current density j_isat and the current density j_z on the other side. Ohm's law

$$\mathbf{j} = \sigma \mathbf{E}, \tag{4.6}$$

where σ is the plasma conductivity and $\mathbf{E}$ is the electric field. The electric field is assumed to be constant in the whole system, oriented in vertical direction. Thus equation 4.6 can be simplified to

$$j_\mathrm{z} = \sigma E_\mathrm{z}. \tag{4.7}$$

The plasma conductivity can be calculated as

$$\sigma = \frac{e^2\, n_\mathrm{e}}{m_\mathrm{e}\, \nu_\mathrm{m}}, \tag{4.8}$$

with n_e the electron density and ν_m the electron-neutral collision frequency [16]. The electron density is calculated from the ion saturation current density j_isat (cf. figure 4.10a) measured with a single pin Langmuir probe:

$$n_\mathrm{e} = 1.64 \frac{j_\mathrm{isat}}{e\sqrt{\frac{e\,T_\mathrm{e}}{m_\mathrm{Ar}}}}. \tag{4.9}$$

And the electron-neutral collision frequency ν_m for argon is calculated as

$$\nu_\mathrm{m} = n_0 K_\mathrm{ap} = 2.6 \times 10^{-14}\, n_0\, T_\mathrm{e}^{1.3}, \tag{4.10}$$

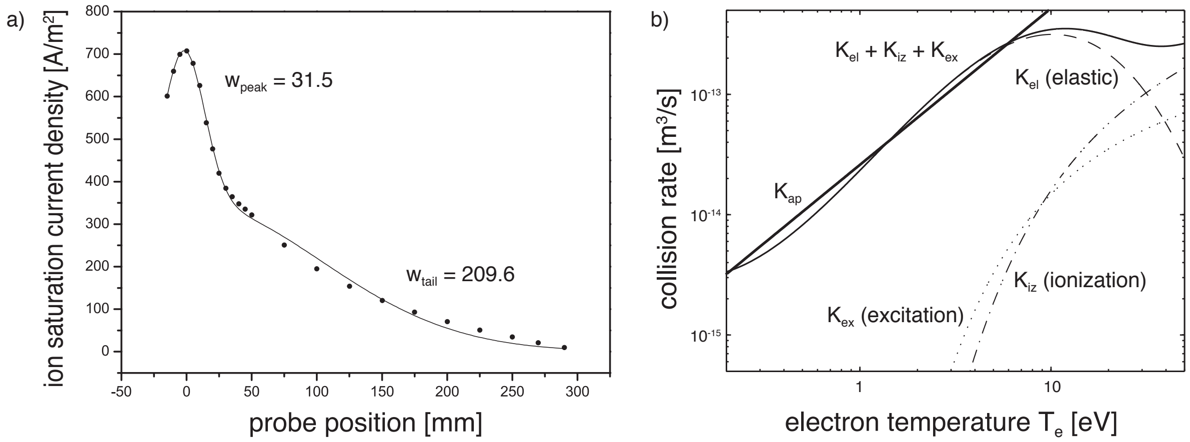

Figure 4.10: a) Ion saturation current density: measurement with single pin Langmuir probe polarised to $-70\,\mathrm{V}$, interpolation with two gaussians; b) Electron collision rate constants K_{el}, K_{iz}, K_{ex} and the approximation K_{ap} versus T_{e} in argon gas [16].

where n_0 is the neutral density and K_{ap} is an approximation of the electron collision rate constant depending on T_{e} in argon gas (cf. figure 4.10b).

By replacing equations 4.8–4.10 in equation 4.7 the electron temperature T_{e} is found from j_{z} and j_{isat}

$$T_{\mathrm{e}} = \left(6.3 \times 10^{13} \frac{E_{\mathrm{z}}\sqrt{e\, m_{\mathrm{Ar}}}}{m_{\mathrm{e}}\, n_0} \frac{j_{\mathrm{isat}}}{j_{\mathrm{z}}}\right)^{5/9} = 3.0 \times 10^{12} \left(\frac{j_{\mathrm{isat}}}{n_0\, j_{\mathrm{z}}}\right)^{5/9}, \tag{4.11}$$

where $E_{\mathrm{z}} = 4\,\mathrm{Vm}^{-1}$ is the mean vertical electric field, found from the floating potential measurements shown in figure 4.9. The difference of V_{f} at the two probe positions is about $1\,\mathrm{V}$ outside the column and the distance between the probes is about $250\,\mathrm{mm}$.

The measurements of the ion saturation current density used for the electron temperature estimation are presented in figure 4.11. In (a) the effect of the applied bias voltage can be seen, measured at probe position 1. In a plasma with $B_{\mathrm{c}} = 45\,\mathrm{G}$ and $p = 0.01\,\mathrm{mbar}$ the electrons in the central column are hot and therefore the probe has to be biased with a higher voltage in order to measure the ion saturation current. The measurements are fitted with the sum of two gaussian distributions. They show a highly dense column in the centre and a weaker but much larger distribution of electrons in the rest of the reactor. (b) shows the profiles of current density of a non confined plasma at probe position 1. With a bias of $-70\,\mathrm{V}$ a central peak can still be found, but it is very weak compared to the confined case. Most of the primary electrons, used for the production of the plasma column, are lost by radial diffusion. Difference pressures show a higher density for higher pressures but taking into account the actual neutral density the maximum ionisation rate in the plasma at $0.003\,\mathrm{mbar}$ is higher ($n_{\mathrm{e,max}}/n_0 = 0.50\,\%$) than in the plasma at $0.01\,\mathrm{mbar}$ ($0.18\,\%$). The current density profiles measured at probe position 2 with $-70\,\mathrm{V}$ bias are given in (c). Three observations can be made: (1) near the source the plasma column is narrower than in the lower part of the reactor, the electrons are less diffused radially by collisions, (2) the electron density in the confined plasma is higher than in a non-confined, not only in the centre column but in a zone with at least half the reactors diameter and (3) at 0.003 mbar and 0 G a small central peak is found with about the same width (22.7) as the ones formed in a confined plasma, the primary electrons are less lost by radial diffusion due the lower pressure.

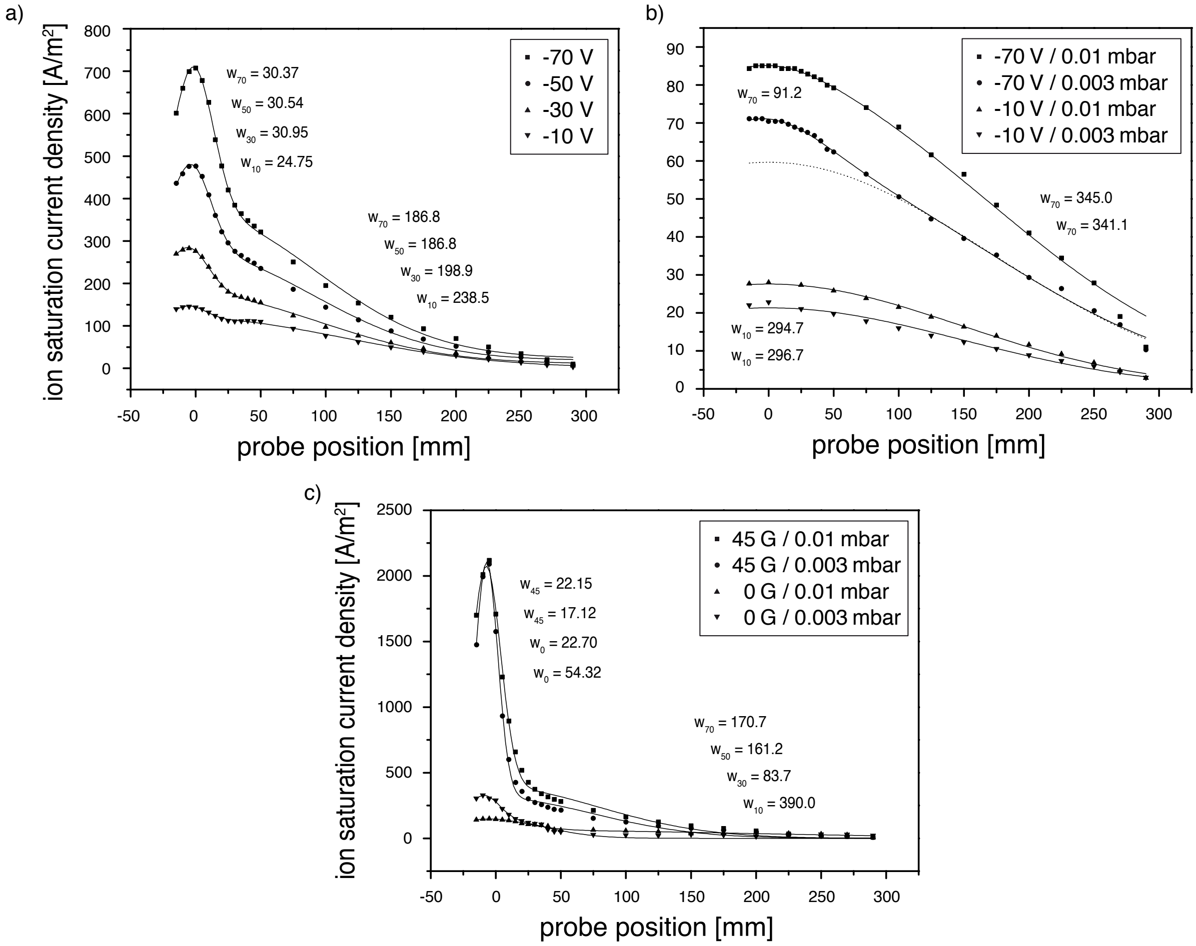

Figure 4.11: Profiles of ion saturation current density measured with a single pin Langmuir probe: a) measured at probe position 1 with 0.01 mbar and 45 G, b) measured at probe position 1 with 0 G, the dotted line represents the ion saturation current density without the weak central peak, and c) measured at probe position 2 with −70 V bias.

With equation 4.11 and the presented Hall probe measurements of j_z and Langmuir probe measurements of j_{isat} an estimation of the electron temperature in the plasma column can now be found (cf. figure 4.12a). As the current density decreases almost to zero outside the plasma column, the calculation for T_e diverges (cf. figure 4.12a) and so it has only a reasonable meaning inside the column (−25 to 25 mm). There the found values of T_e are between 3–6 eV. The temperature is probably slightly overestimated in the case of the non-confined plasma measured at probe position 1. To simplify calculations in the following sections, the electron temperature is taken as constant with a value of 4 eV.

The electron density profiles presented in figure 4.12b are calculated using equation 4.9

with the constant electron temperature $T_e(0\,\mathrm{mm})$. As expected from the measurements of j_{isat} the magnetic field plays an important role for the electron density. The magnetic field reduces the radial diffusion which leads to a higher collision rate inside the plasma column. This in turn increases the number of secondary electrons also outside the column. An interesting result from the calculation of n_e is that the density outside the plasma column hardly depends on the position of measurement, but inside the column the density is about 2.5 times higher for the measurements near the source than near the anode.

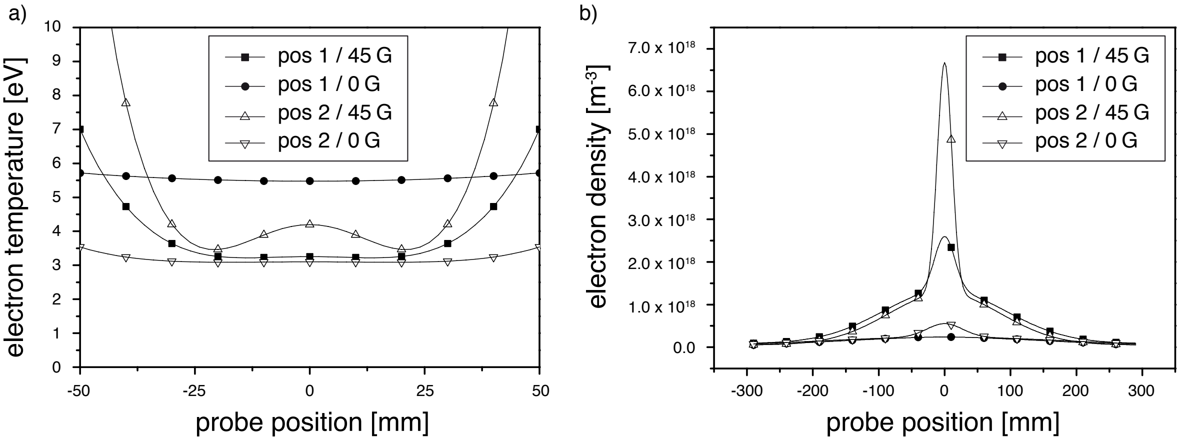

Figure 4.12: a) Calculated electron temperature profiles (equation 4.11) in the plasma column for different magnetic fields and at probe positions 1 and 2; b) Electron density profiles found from ion saturation current density j_{isat} and constant electron temperature approximation $T_e = 4\,\mathrm{eV}$.

4.3 Plasma species composition

In this section optical emission spectroscopy (OES) measurements of argon-silane plasmas in the BAI reactor are presented, made with an imaging spectrograph, as presented in section 2.1.4. These spectra are compared to the spectra found in a large area RF plasma and a higher pressure (1.5 mbar) HCDCA plasma, showing that the dominating species are molecular in a RF plasma, atomic in a high pressure HCDCA plasma and ionic in a low pressure HCDCA plasma [36]. Furthermore the species found inside and outside the plasma column by OES and the effect of the silane influx on the plasma composition are presented.

Figure 4.13 shows OES spectra of a RF silane plasma, a HCDCA argon-silane plasma in the millibar range and a HCDCA argon-silane plasma at 0.01 mbar respectively. The RF plasma used for large area depositions dissociates the silane molecule into different types of radicals such as SiH, SiH_2 and SiH_3, whereof only the SiH radicals have a line in the emission spectrum. The liberated hydrogen is found either as excited atomic H_α or as excited H_2. This is shown in the OES spectrum given in figure 4.13a. In a HCDCA plasma used in the millibar range the emission spectrum, measured in the center of the plasma column (with fiber 13), shows several important differences (cf. figure 4.13b). A strong

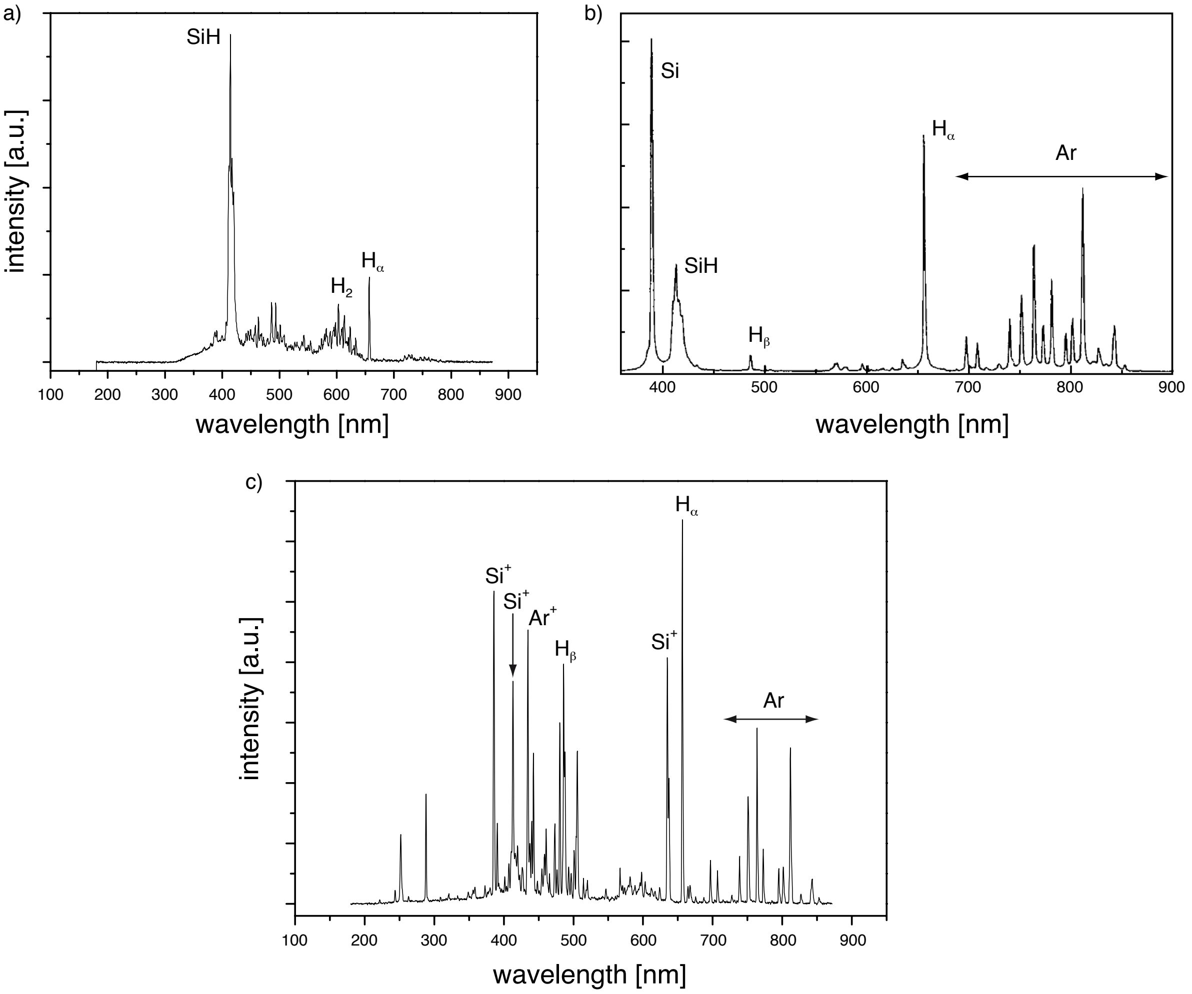

Figure 4.13: Optical emission spectroscopy measurements of three different plasmas. The dominating species are molecular, atomic and ionic, respectively in a) a large area RF plasma, b) a high pressure (1.5 mbar) HCDCA plasma and c) a low pressure (0.01 mbar) HCDCA plasma.

peak from excited atomic silicon is found whereas the peak of SiH is strongly decreased. Hydrogen is found mainly as H_α and even in the form of H_β, but no molecular hydrogen is found. As in the process argon is used to protect the filament from backdeposition with silicon, also a broad band of lines due to excited argon is found. A decrease of the pressure by two orders of magnitude again leads to important changes in the spectrum, shown in figure 4.13c. Silicon is mainly found in its ionic state. Also ionic argon is found besides the broad band of excited neutral argon. Hydrogen is still found in majority as H_α, but the relative amount of H_β has become larger. These spectra show that the plasma source studied in this thesis is very efficient for dissociation, especially at low pressure.

4.3.1 Qualitative analysis of the electron thermalisation in the plasma column

Some of the main peaks of the species found from the intensity spectrum shown in figure 4.13c are presented in table 4.1 with their corresponding wavelengths and excitation energies.

Species found			
species	name	wavelength	energy [eV]
Si^+	Si II n°1	385.70 nm	6.86–10.07
Si	Si I	390.55 nm	1.91–5.08
SiH	SiH	414.23 nm	0.00–3.01
Ar^+	Ar II n°1	434.81 nm	16.64–19.49
H_β	H_β	486.14 nm	10.20–12.75
Ar^+	Ar II n°2	487.99 nm	17.14–19.68
Si^+	Si II n°2	634.71 nm	8.12–10.07
H_α	H_α	656.27 nm	10.20–12.09
Ar	Ar I n°1	696.54 nm	11.55–13.33
Ar	Ar I n°2	706.72 nm	11.55-13.30

Table 4.1: Principle species found in the plasma with OES measurement and their respective wavelengths and excitation energies [37,38,39].

For the detection of the weak SiH peak at 414.23 nm, it was necessary to measure the intensity spectrum at 3 cm from the column, outside the high energy electron beam. In figure 4.14 the zoom of two intensity spectra found in a argon-silane plasma are given, one measured inside the plasma column and one measured outside. It can be seen that the weak SiH peak is comparable to the background noise, coming from impurities and measurement inaccuracy, when measured in the column center, but becomes equivalent to the Si^+ peak when measured at 3 cm from the center of the column.

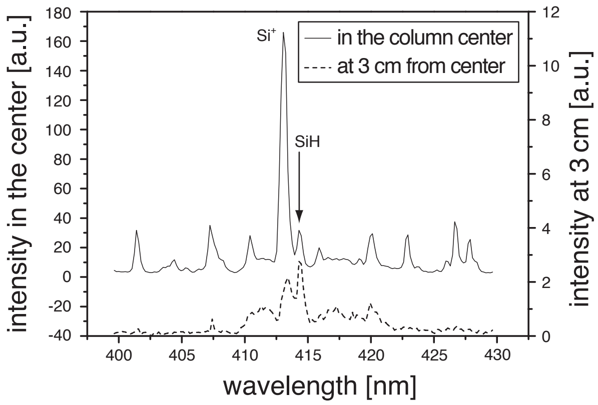

Figure 4.14: Comparison of two spectra, one measured in the center of the plasma column (fiber 13), the other measured at a distance of 3 cm from the center (fiber 1).

The results from figure 4.14 indicate that the fast primary electrons, forming an electron beam, are not thermalised with the electrons produced in the ionisation process. For a qualitative analysis of the thermalisation of the electron beam, the intensity profiles through the plasma column of the different species as given in table 4.1 were measured and calculated. The profiles, normalised for the central position, are shown in figure 4.15. They were measured in three variable conditions, using 100 sccm or 200 sccm of silane and 40 A or 120 A for the discharge current, respectively. The profiles of the species with the lowest excitation energy (Si and SiH) show a profile less peaked than the others in all three conditions. On the other hand, the profile of Ar^+, having the highest excitation energy of the species concerned, shows a stronger peaked profile in the case of $\phi_{\mathrm{SiH}_4} = 100\,\mathrm{sccm}$ and $I_{\mathrm{pl}} = 120\,\mathrm{A}$, but no difference to the other profiles in the other two conditions.

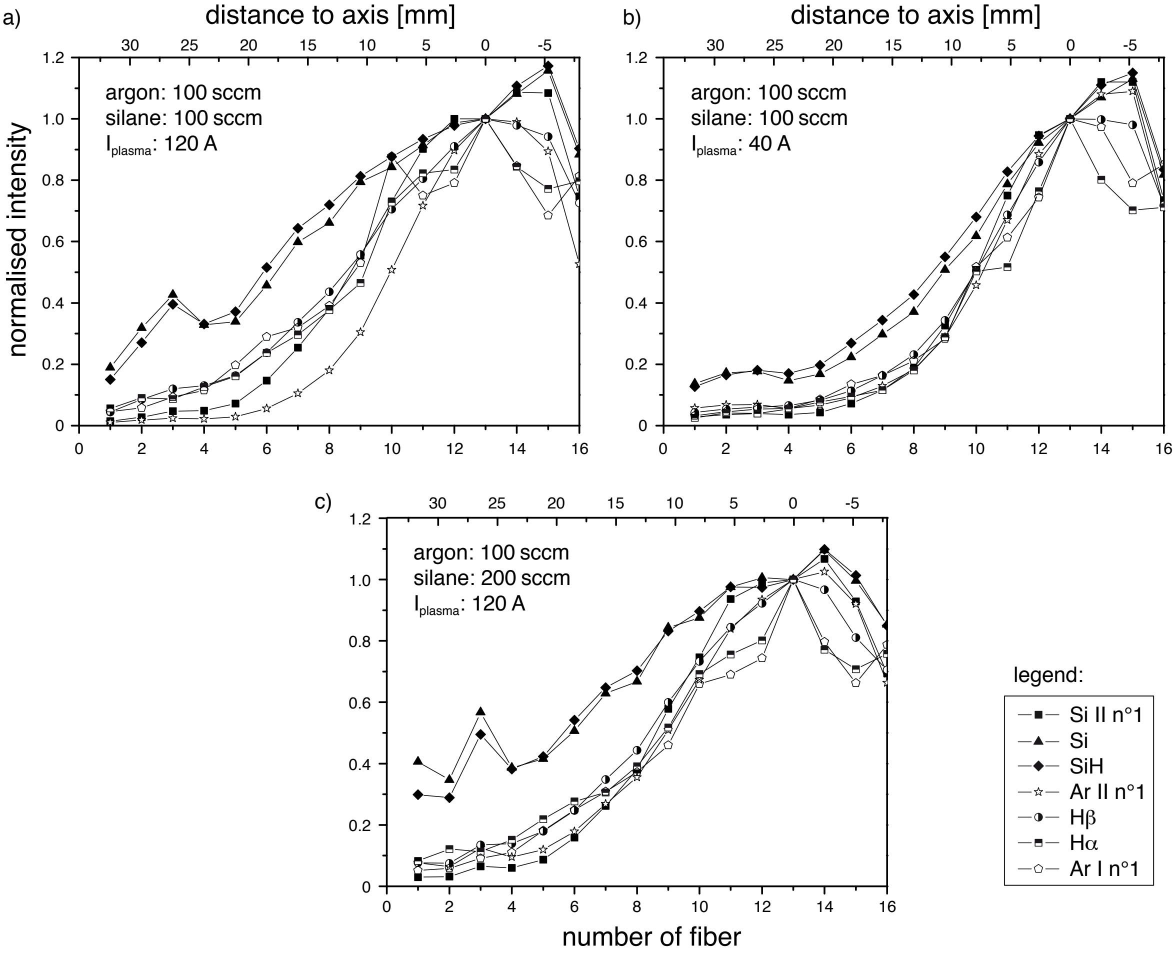

Figure 4.15: Integrated peak values of the optical emission spectra depending on radial position. All profiles are normalised for the central peak integral measured with fiber 13. a) With 100 sccm SiH_4, 120 A; b) with 100 sccm SiH_4, 40 A; c) with 200 sccm SiH_4, 120 A.

These intensity profiles can be used to qualitatively estimate the thermalisation process of the electron beam with the background low energy population of the electrons. The intensity of the light emitted by the plasma due to recombination and de-excitation processes is given by

$$I_{\mathrm{s}} = n_{\mathrm{s}} n_{\mathrm{e}} \langle \sigma v \rangle \,, \tag{4.12}$$

where the index s stands for any given species, supposed to be immobile compared to the electrons. n_s and n_e are the species and electron density, respectively, σ is the electron-species collision cross-section and v the velocity of the electrons. The species density n_s is assumed to be constant in the whole reactor volume. The term $\langle\sigma v\rangle$ can be calculated as the convolution of the collision cross section with the electron energy distribution function (cf. figure 4.16a). Therefore equation 4.12 can be written as

$$I_s = n_s n_e \int f(\varepsilon)\sigma(\varepsilon)d\varepsilon, \tag{4.13}$$

with ε the electron energy and $f(\varepsilon)$ the electron energy distribution function. From figure 4.16a one can see that the convolution only depends on the high energy tail of the electrons and the higher the threshold energy for the collision the stronger the effect of the electron beam.

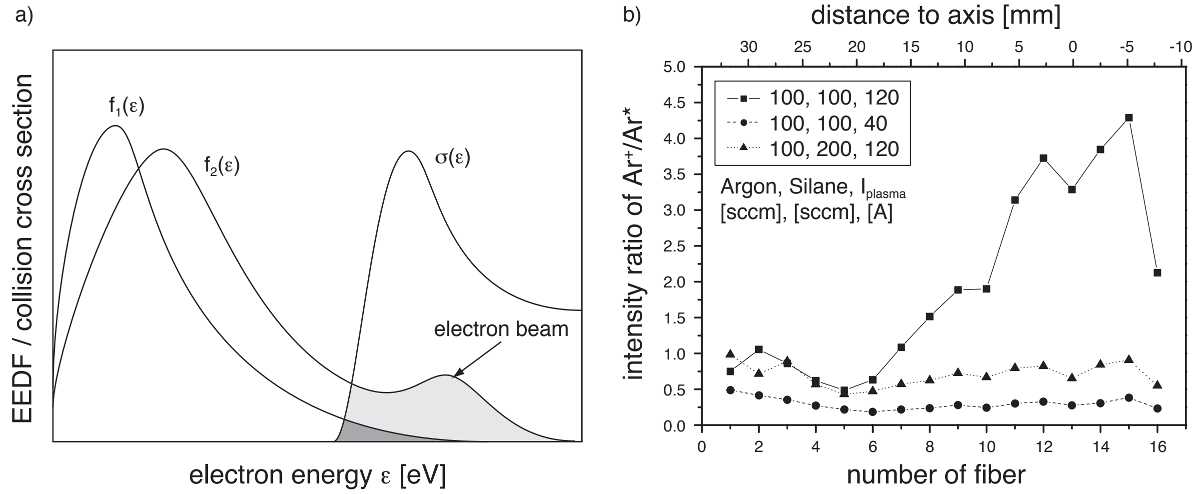

Figure 4.16: a) Convolution (grey surfaces) of a collision cross section with electron energy distribution functions (EEDF). $f_1(\varepsilon)$ represents a Maxwellian EEDF, whereas $f_2(\varepsilon)$ represents an EEDF with a hot directional electron beam; b) Intensity ratio profiles through the plasma column of argon ions compared to argon radicals in three variable plasma conditions. With $\phi_{\mathrm{SiH_4}} = 100\,\mathrm{sccm}$ and $I_{\mathrm{pl}} = 120\,\mathrm{A}$ an electron beam is found, whereas in the two other cases the electrons are thermalised between themselves.

By dividing the intensity profiles of argon ions and argon radicals, having different minimal excitation energies, the electron density is eliminated from equation 4.13. The intensity ratio calculated is an indicator of the size of the hot electron population: The higher the ratio the larger the population of electrons in the beam.

In figure 4.16b profiles of the intensity ratios between argon ions and argon radicals through the plasma column are presented. For these calculations the non-normalised intensity profiles were used. In the case of $\phi_{\mathrm{SiH_4}} = 100\,\mathrm{sccm}$ and $I_{\mathrm{pl}} = 120\,\mathrm{A}$ a peaked intensity ratio profile is found, indicating the existence of an electron beam in the centre of the plasma column. When the discharge current is reduced to 40 A, the intensity ratio profile has become completely flat, indicating that the electron beam is thermalised at the position of measurement. The same behaviour can be observed for an increased silane flux ($\phi_{\mathrm{SiH_4}} = 200\,\mathrm{sccm}$), different only in the value of the ratio but not in the profile shape. This is easily explained by the higher discharge current used to drive the plasma, which leads to a higher electron temperature in the whole reactor.

4.3.2 Composition dependence on silane flux

The spectra presented in figures 4.13b and 4.13c show an important pressure dependence of the plasma composition. It was observed that an increase if the silane flux from 50 sccm to 300 sccm leads to a strong increase of pressure from 0.005 mbar to 0.05 mbar. In section 5.4 the pressure behaviour with variable silane flux will be further discussed. In this section the effect of the observed change in pressure on the composition of the different plasma species is discussed.

In figure 4.17 the integrated intensities of the Si^+ peak at 385.7 nm for different silane fluxes measured with the 16 fibers is given. The decrease of the intensities for silane fluxes higher than 100 sccm is related to a better thermalisation of the hot primary electrons when the gas pressure in the reactor rises.

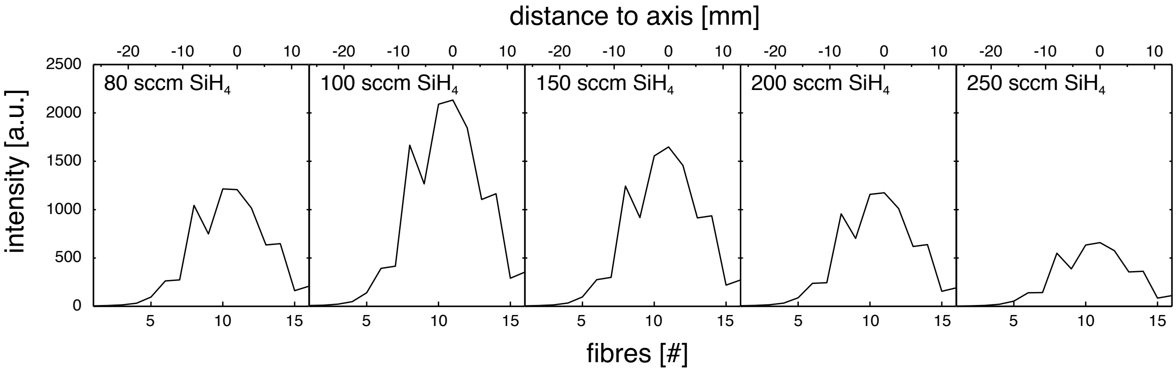

Figure 4.17: Integrated intensity of the Si^+ peak at 385.7 nm for different silane fluxes measured with 16 equally spaced optical fibers.

In figure 4.18 the variations of the integrated intensity peaks found in the center of the plasma column and depending on the silane flux are given for four plasma species: argon ion, silicon ion and excited hydrogen H_α and H_β. The three graphs depending directly on silane (Si^+, H_α and H_β) show a maximum between 100 and 150 sccm. This has a direct effect on the film growth rate as will be shown in section 5.2.1.

The drastic drop of ionic argon compared to ionic silicon can only partly be explained by the higher density and, resulting from this, the lower power per particle. The argon flux into the ionisation chamber is fixed for all measurements to 100 sccm. Therefore its proportion in the gas mixture decreases, leading to a stronger drop in the intensity measurements. Furthermore the argon is entering the reactor through the ionisation source, whereas the OES measurements are made at half height of the reactor, 32 cm above the reactor floor. With increasing pressure the argon no longer reaches the lower part of the reactor but is lost to the pumps by convection.

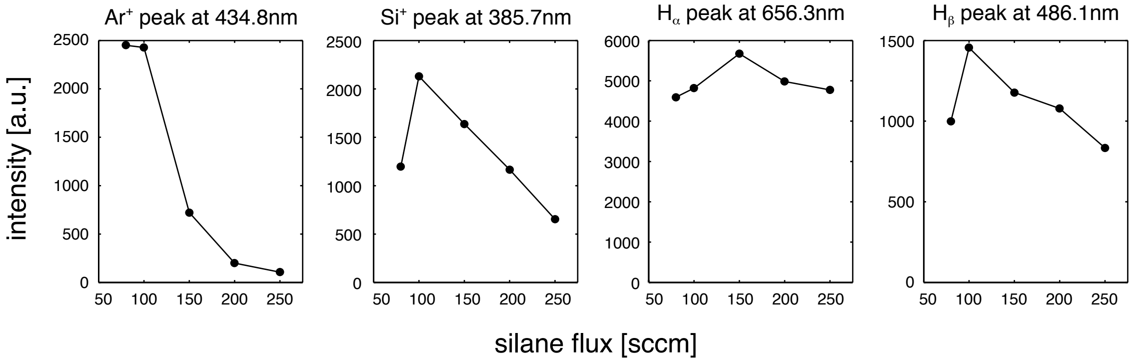

Figure 4.18: Variation of the integrated peak intensity of four different species measured in the center of the plasma column.

A further and very simple way to analyse roughly the plasma composition is the analysis of the color of the plasma column. In figure 4.19 five photos of the plasma with increasing silane flux are shown. A typical argon RF plasma has a pink colour coming from the spectral argon lines at 700 nm. In the low pressure HCDCA argon plasma the dominating species are Ar^+ (≈ 450 nm) radiating in blue. When adding silane the colour changes to violet, the emission is dominated by the different silicon species (Si, SiH and Si^+) with wavelengths at 385–415 nm. With a silane flux higher than 250 sccm the colour changes to red-orange, similar to a pure hydrogen plasma.

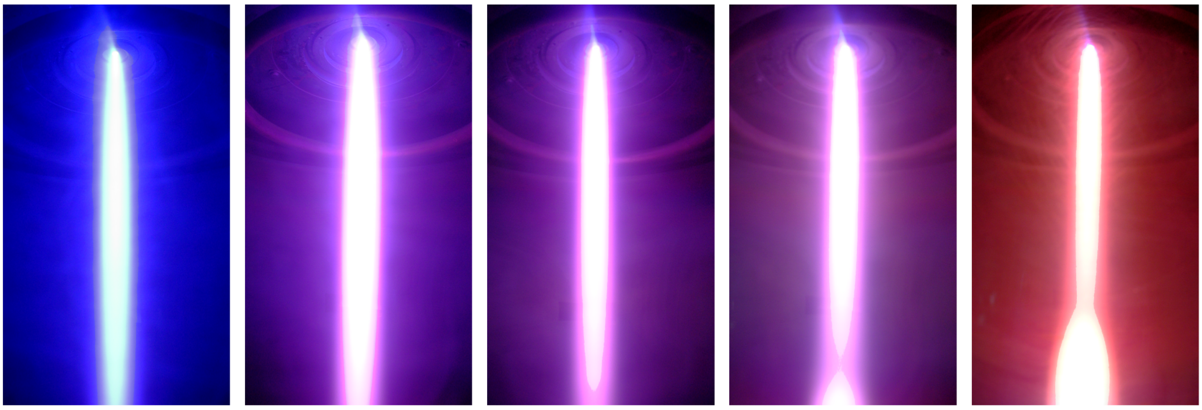
0 sccm SiH_4 0.0015 mbar
80 sccm SiH_4 0.0047 mbar
150 sccm SiH_4 0.0097 mbar
225 sccm SiH_4 0.022 mbar
300 sccm SiH_4 0.047 mbar

Figure 4.19: Colour variation of the plasma emission depending on the silane flux. The argon flux is constant at 100 sccm.

The photos in figure 4.19 show also an upcoming problem. For a silane flux of 150 sccm or higher the plasma column is no longer homogeneous along the vertical axis. This effect is best seen for 300 sccm, where a large glow over the anode appears. It is assumed that this effect is directly related to the higher pressure in the reactor and the resulting collisional loss of primary electrons.

4.4 Conclusion

With the installation of two larger Helmholtz coils the plasma could be confined in a narrow columnar shape. Inside this column a strongly peaked current density profile is found, measured with a custom-built multi-Hall probe. Testing the probe in different angular positions, thus inside the plasma column or outside it, showed no perturbation effects on the current density although optical observations show a strong reduction of light emission from the plasma if the probe is turned into the column. With a Langmuir probe the ion saturation current density profiles of the plasma were measured in order to estimate the electron temperature and electron density inside of the plasma column.

Optical emission spectroscopy measurements proofed the high dissociation efficiency of the HCDCA plasma, especially in the low pressure range used in this work. The intensity spectra are dominated by lines of silicon and argon ions as well as hydrogen radicals. The OES measurements were also used to make a qualitative analysis of the electron temperature in different plasma conditions, using the intensity profiles of argon radicals and argon ions through the plasma column. It was shown that an increase of silane flux from 100 sccm to 200 sccm as well as a reduction of I_{pl} from 120 A to 40 A leads to thermalised electrons at the position of measurement. This indicates that, depending on the applied discharge current and the gas pressure in the reactor, the electrons thermalise at variable position in the plasma column. The effects of this variation in plasma flame length will be further discussed in section 5.2.1.

Chapter 5

Characterization of films produced by PECVD

5.1 SiC films for hard coatings

Thin films of silicon carbide (SiC) are of great scientific and technological interest, since these materials present an outstanding set of properties, like good mechanical resistance, high hardness, high thermal conductivity and very high thermal stability. Their applications may range from protective coating against corrosion to microelectronic devices, and from X-ray mask materials to the protection of thermonuclear reactor walls [40]. This variety of applications led to different processes for the deposition of SiC films, such as: RF magnetron sputtering [40], RF plasma-enhanced chemical vapour deposition (PECVD) [41], laser reactive ablation deposition [42] or atmospheric pressure CVD [43]. Depending on these methods the deposition rates and the final film structures are very different:

a) 0.07 nm/s for crystalline SiC with RF magnetron sputtering

b) 0.3 nm/s for nanocrystalline SiC with RF PECVD

c) 1 nm/s for polycrystalline SiC with laser reactive ablation deposition

d) 14 nm/s for polycrystalline SiC with atmospheric pressure CVD.

A second important parameter in these processes is the substrate temperature as high temperature heat treatments can have the consequence of long-range diffusion of dopants and impurities into the substrate or previously deposited films. Depending on the process the substrate temperature varies from a few hundred degrees Celsius (magnetron sputtering or laser deposition) to about 1200°C (RF PECVD or atm. pressure CVD).

In collaboration with Oerlikon Balzers, the capabilities of the BAI reactor to be used for the production of wear resistant SiC coatings was studied. The SiC films were deposited on Si wafers with native oxide, positioned inside the reactor on substrate holders as shown in figure 1.8. The discharge current was fixed to 100 A with an arc voltage varying between 37–48 V. Additional to the used precursor gases, silane and methane, a 100 sccm argon flux is set directly into the ionisation source. The gas pressure varied between 0.004–0.02 mbar and the magnetic field was typically set to 60 G. Several diagnostics were used during and after the deposition process. The temperature of the samples, typically around 300°C, was measured with a thermocouple. In situ laser reflectometry measurements were performed during the film growth for deposition rate calculation. With ex situ alpha-step measurements the growth rates found were cross checked. Finally FTIR measurements were used for film-composition analysis. In section 5.1.2 it will be shown the films contained still too high hydrogen and oxygen concentrations, so the films either peeled off directly or could be scratched easily.

5.1.1 Growth rate studies

For an efficient industrial process it is important to have high deposition rate. Therefore in situ laser reflectometry as described in section 2.2.1 was used for growth rate measurements with different gas mixtures. The gases used were argon, silane and methane, whereas argon was set to a fixed flux of 100 sccm. Silane and methane fluxes varied from 20–160 sccm and from 20–80 sccm respectively. Figure 5.1a shows the effect of increasing silane flux $\phi_{\mathrm{SiH_4}}$ on the film growth rate. For low fluxes up to 80 sccm the increase is linear, but for higher fluxes a saturation can be observed. This effect has also been observed in the deposition process of μc-Si:H films (cf. section 5.2.1).

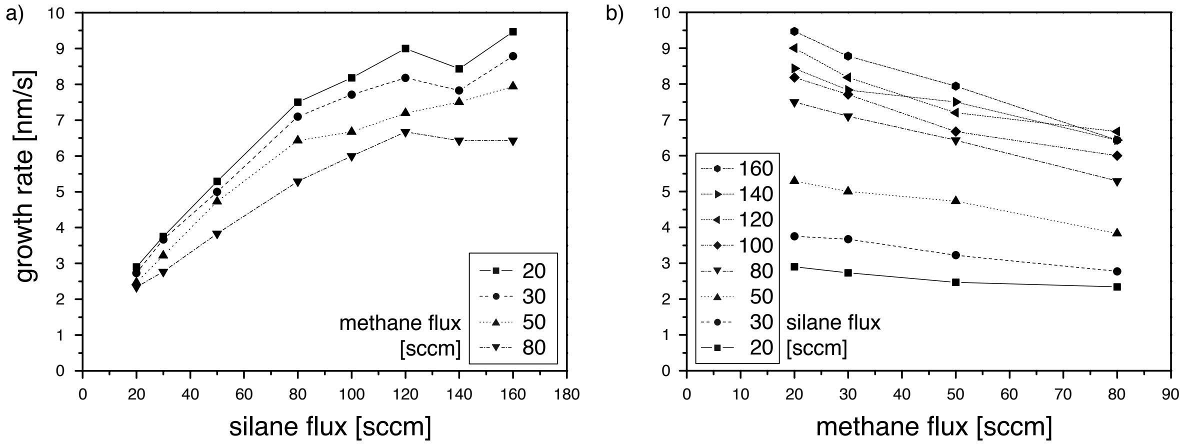

Figure 5.1: Film growth rate calculations from in situ interferometry measurements. a) an increase in silane flux leads to an increase of the growth rate, with a slowdown for higher fluxes; b) an increase of methane flux leads to a linear decrease of the growth rate.

In figure 5.1b the growth rates for variable methane flux is shown. With increasing methane flux for any given silane flux a linear decrease is found. This can be explained with the different sticking properties of the $\mathrm{SiH_x}$ and $\mathrm{CH_x}$ radicals ($\mathrm{x} = 0$–3). In table 5.1 the surface loss probabilities β and sticking coefficients s of different types of radicals are given. In general the values show a loss probability and sticking coefficient for silicon species about 1–2 orders of magnitude higher. Therefore, by increasing $\mathrm{CH_x}$ radical concentration, less $\mathrm{SiH_x}$ radicals arrive at the substrate surface as they are replaced by the

CH_x radicals. Therefore, with the CH_x radicals having much lower sticking coefficients, the total loss of silane and methane to the pumps is increased and the growth rate is slowed down.

Species	β	s
SiH_3	0.26	0.09
SiH_2	0.8	0.8
SiH	0.95	0.95
Si	1	1
CH_3	0.014	–
CH_2	–	0.025

Table 5.1: Surface loss probabilities β and sticking coefficients s of SiH_x and CH_x radicals [44, 45, 46]

A further system parameter, who effects the growth rate, is the applied magnetic field. In figure 5.2 the growth rate measurements at four different field strengths and with four different gas mixtures are shown. It can be seen that for a small magnetic field an increase of the field strength leads to an increase in growth rate. This can be explained by an increase of electron and ion confinement in the plasma column leading to a higher collision rate. This in turn leads to more SiH_x and CH_x radicals which are deposited on the wafer. However, if the magnetic field gets higher than 50 G the growth rate begins to decrease. Here another effect becomes more dominant: The radicals needed for the deposition are confined in the center region of the plasma column and can no longer diffuse to the wafer.

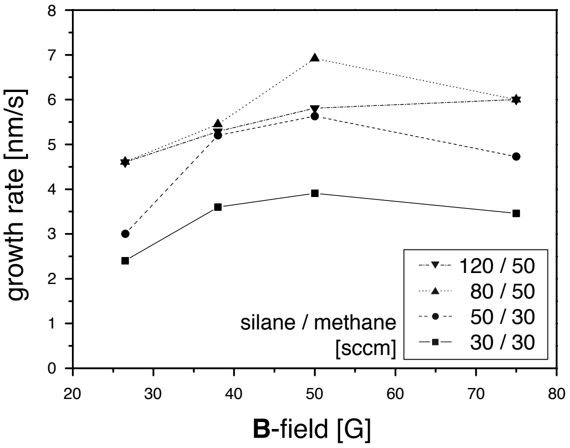

Figure 5.2: Film growth rate with variable magnetic field. The maximum value is found around 50 G.

5.1.2 Film quality and impurity concentration

More important than having a fast deposition process is to get an SiC film showing the desired tribological properties. Unlike the hydrogenated microcrystalline silicon films used for solar cells or other applications, the hydrogen content in hard SiC films has to be minimized. To analyse the components of the SiC films produced in the BAI reactor, FTIR absorption spectra were measured on 16 different SiC films. The variable parameters to deposit these films were the silane and methane fluxes (20, 50, 80 and 120 sccm) and film thicknesses between 1000 nm and 2000 nm. Because of the rather thin films the FTIR spectra show an oscillating background due to interferences. This background signal had to be eliminated in order to deconvolute the spectra and to integrate the different peaks. To do this a spline polynomial interpolation was used for about 20 points manually chosen from the spectra where no peak is found. An example of the interpolated function and the resulting corrected spectrum can be seen in figure 5.3a.

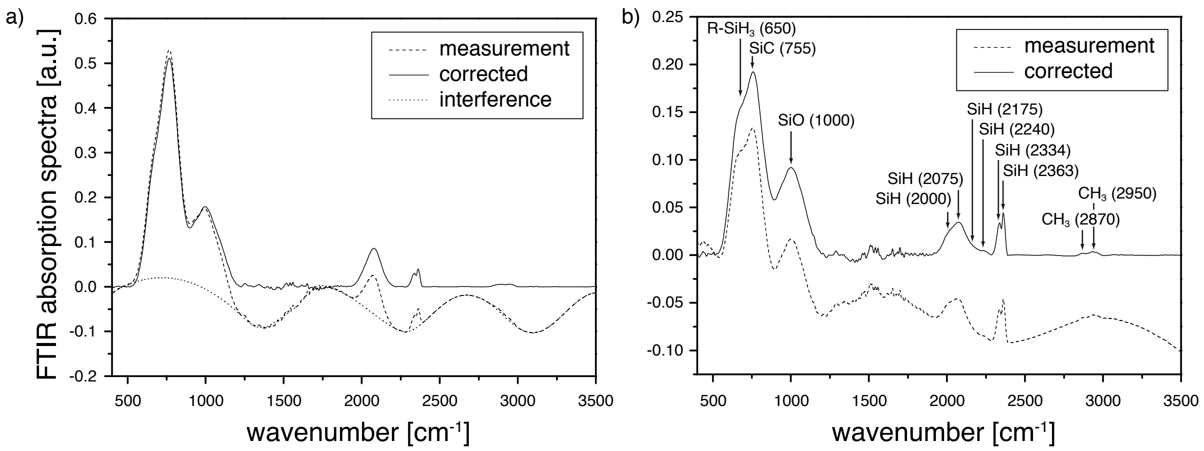

Figure 5.3: a) Correction of a FTIR spectrum for deconvolution. (- - -) measured absorption spectrum showing interferences, (· · ·) background interpolation and (—) corrected FTIR spectrum; b) All interesting peaks found in the spectra and the assignment to the different atomic connections.

The different peaks found in the spectra and the assignment to the different atomic connections are shown in figure 5.3b. In total 11 important peaks were found: R-SiH_3 (650 cm^{-1}), SiC (755 cm^{-1}), SiO (1000 cm^{-1}), 6 SiH peaks (2000–2363 cm^{-1}) and 2 CH_3 peaks (2870 cm^{-1}, 2950 cm^{-1}). The CO peak is close to the SiO peak, so they are taken as one for the deconvolution and intensity analysis as they represent the same problem: oxygen contamination.

Hydrogen concentration in the SiC films

To compare the hydrogen concentration on the film to the SiC bonding, the 6 SiH peaks are integrated and compared to the integrated SiC peak. In figure 5.4a the ratios between the sum of the SiH peaks and the integrated SiC peak are presented. It shows that a minimum of hydrogen concentration is obtained around 50 sccm of silane flux except for a flux of 50 sccm of methane, where the minimum is found for even lower silane fluxes. This minimum around 50 sccm of silane is due to a balance between two opposed effects: 1) having a high enough SiH_x concentration for the deposition of SiC and 2) having too much SiH_x leading mostly to silicon deposition.

A study of the effect of methane flux variation shows a decrease of hydrogen concentration for an increasing methane flux. This is a result of a much higher increase of Si-C bonds compared to the relatively small increase of SiH bonds when adding more methane in the process. Different binding energies of the species in process can be an explanation for this effect. The dissociation enthalpy of a C-C bond (607 kJ/mol) is higher than the dissociation enthalpy of Si-C (451.5 kJ/mol) or Si-Si (326.8 kJ/mol) bonds. Therefore only a high carbon concentration can lead to a substantial increase in SiC formation. For small carbon concentration most of it is bound in C-C bonds.

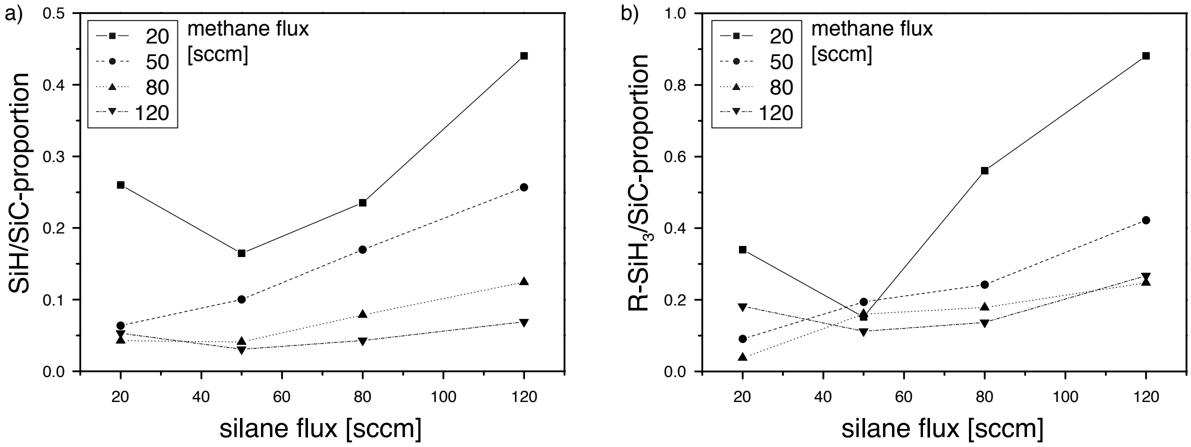

Figure 5.4: Proportion of SiC to SiH bonds. a) Integrated SiC (755 cm^{-1}) peak divided by the sum of the 6 integrated SiH peaks (2000–2363 cm^{-1}); b) Integrated SiC peak divided by the integrated SiH_3 peak (650 cm^{-1}).

The second graph dealing with Si-H bonds is shown in figure 5.4b. It shows the proportion between Si-C bonds and the Si-H bonds in an R-SiH3 connection. This peak has been used because of its relatively important surface. It shows a very similar behavior as the sum of the 6 other SiH peaks, namely a decrease of Si-C bonds compared to Si-H bonds for silane fluxes higher than 50 sccm. With silane fluxes lower than 50 sccm the trends of the measurements are similar to those in figure 5.4a, except for 80 sccm of methane. Furthermore it is found that there are about 10 times less C-H bonds in the film than Si-H bonds.

The high concentration of hydrogen in the films is a hint of either a very porous film structure or the formation of very small crystal grains, leading to a higher concentration of grain boundaries, thus higher hydrogen concentration. SEM and TEM studies of different films have shown that depending on the gas mixture of silane and methane, one or both explanations are applicable. The SEM images shown in figure 5.5 are made by M. Kogelschatz on SiN films instead of SiC, but produced in similar conditions in the BAI reactor. The film shown in figure 5.5a has a cauliflower like structure, thus a high porosity, the film shown in figure 5.5b has a smoother structure. The crystal grains in both films have a size of less than 10 nm, which is smaller than the typical size for grains in microcrystalline films [47]. Apparently the fast deposition process with deposition rates up to 10 nm/s leads to a high density of crystalline grains growing in parallel.

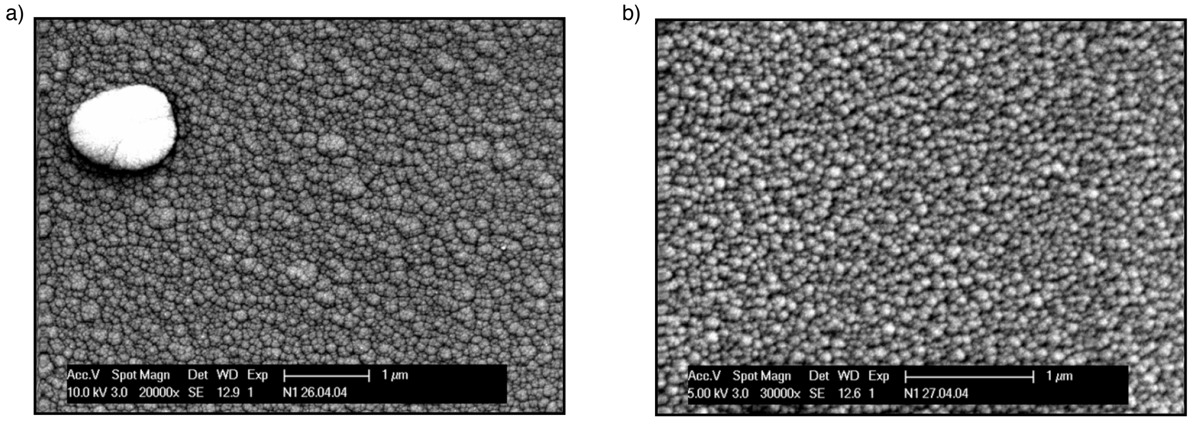

Figure 5.5: SEM images of films deposited in plasmas with different gas mixtures: a) in a $N_2/H_2/SiH_4$ plasma, showing a cauliflower like structure; b) in a NH_3/SiH_4 plasma, showing a smoother film.

The hydrogen concentration found from the SiH peaks as a function of the substrate temperature is shown in figure 5.6a. It was expected that with an increasing wafer temperature more hydrogen would diffuse to the film surface and be liberated as H_2 molecules. Instead the hydrogen concentration rises with higher substrate temperatures, to values of nearly 50 % for 20 sccm of methane. There are other effects than the wafer temperature playing a major role in the elimination of hydrogen in the film. In any case, the found hydrogen concentration is too high to obtain required hardness and films with good tribological properties have to be mono- or polycrystalline.

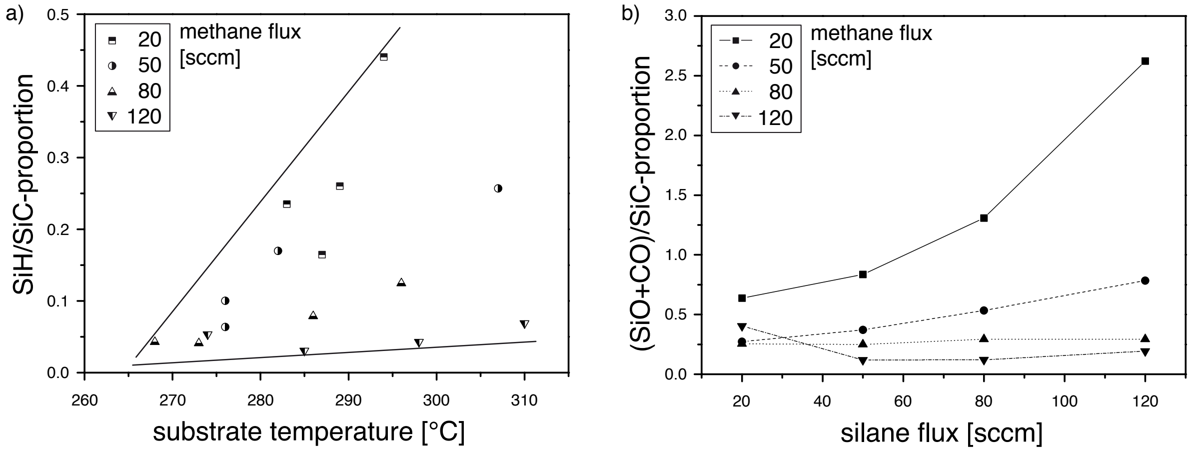

Figure 5.6: a) Hydrogen ratio depending on the substrate temperature; b) Oxygen ratio found in SiO and CO bonds compared to the SiC bonds.

Oxygen concentration in the SiC films

As a dominating impurity, oxygen is found in the films. The ratio of oxygen concentration found from Si-O and C-O bonds compared to the SiC concentration is given in Figure 5.6. Depending on methane and silane flux the oxygen concentration is up to two times higher than the hydrogen concentration. This is remarkable as oxygen is supposed to enter the process only through leaks or by degassing of the reactor walls. However, a look on the dissociation enthalpies H_{diss} of the above mentioned bonds may explain this high concentration of oxygen. H_{diss} of Si-O bonds (799.6 kJ/mol) and C-O bonds (1076.5 kJ/mol) is about two times higher than H_{diss} of Si-C bonds (451.5 kJ/mol). Nevertheless, compared to the hydrogen concentration this is still a minor problem, as with a more leakproof reactor and a better preliminary degassing process the oxygen concentration could be essentially decreased. The effect of a better outgassing of the reactor will be discussed in more detail in section 5.2.4, dealing with nc-Si:H films.

5.2 nc-Si:H and a-Si:H films for solar cell applications

In 1976 Wronski *et al.* [48] showed for the first time that efficient silicon solar cells can be fabricated from thin films of amorphous silicon. The initial efficiencies of the cells were about 1–2 % with a strong degradation under light exposure, known today as the *Staebler-Wronski effect*. The work of Wronski *et al.* led to the development of various techniques and methods for the deposition of thin film silicon solar cells [49]. One widespread method is plasma-enhanced chemical vapour deposition (PECVD). It can be used for the production of different types of silicon layers such as a-Si:H, μc-Si:H or even epitaxial silicon. The improvements in this domain led to a substantial increase of efficiency and long term stability of the solar cells. Table 5.2 gives an overview of different types of silicon solar cells, their conversion efficiencies, and whether they are produced in laboratory or industrial conditions.

solar cell type	efficiency [%]	
	laboratory	industrial
crystalline silicon	24.7 [50]	22.7 [51]
multicrystalline silicon	20.3	15.3 [51]
epitaxial silicon	19.2	13.8 [52]
micromorph tandem	13.7 [53]	11.7 [51]
amorphous silicon	10.1	10.4 [51]
microcrystalline silicon	9.1 [54]	–

Table 5.2: Efficiencies of different types of silicon solar cells.

Besides the cell efficiency it is important for cost effective production to have high deposition rates and good film uniformity. In large area RF reactors deposition rates of 1.3 nm/s have been reported for μc-Si:H [4] and in smaller devices deposition rates of more than 3 nm/s for μc-Si:H and 1.4 nm/s for micromorph silicon have been achieved [53].

In this section the results of investigations on the deposition of μc-Si:H using the BAI reactor are presented. The aim of these studies, realised in collaboration with Oerlikon Solar, was to show that the BAI reactor is suitable for the high rate deposition of μc-Si:H films for use in solar cells. Therefore the produced material has to be dense, defect free and with low contamination. The silicon films were deposited on either Si wafers ($3 \times 3\,\mathrm{cm}^2$) or glass substrates ($5 \times 5\,\mathrm{cm}^2$), positioned inside the reactor on substrate holders as shown in figure 1.8. If not stated otherwise the discharge current was fixed at 120 A with an arc voltage varying between 35–50 V and a magnetic field of 60 G was applied. Additional to the silane used as precursor gas, a 100 sccm argon flux is set directly into the ionisation source to protect the filament from chemical reactions. For the analysis of the process and the deposited films, several diagnostics were used during and after the deposition process. The temperature of the samples, typically around 200–300°C, was measured with a thermocouple. The growth rate was measured with an ex-situ alpha-step device. SEM imaging gave an idea of the film structure and an estimation of the crystallite size. For detailed crystallinity measurements a Micro-Raman system (cf. section 2.3.1) was used. With FTIR measurements the contamination of the films with oxygen was analysed. Finally the Fourier transform photocurrent spectroscopy (FTPS) technique was used to measure absorption spectra of the films and to compare them with typical c-Si, a-Si:H and μc-Si:H films. [55]

5.2.1 Homogeneous deposition rate along the plasma column

The process gas injection in the BAI module is made through a ring shaped showerhead with a diameter of 34 cm and an inner tube diameter of 2 cm. It is positioned in the top part of the chamber. The gas is injected in the chamber through 8 holes ($\varnothing = 2\,\mathrm{mm}$) placed symmetrically and directed in an outer-down direction with an angle of 45°. This configuration of the gas injection apparently had no effect on the process at pressures in the millibar range [10, 1]. At a gas pressure in the range of 10^{-3}–10^{-2} mbar however, an important inhomogeneity in growth rate is found along the plasma column.

In order to increase the vertical homogeneity of the Si film growth rate a linear gas injection system is installed, parallel to the plasma arc. Furthermore the number of holes is increased and their size decreased. The new showerhead consists of 16 holes with a diameter of 0.5 mm. A detailed study to find the optimal number and size of holes using a 3D-model is given in the following.

Gas flow model for optimal showerhead configuration

A numerical simulation of the gas flow through a linear gas injection using COMSOL's Navier-Stokes package for an incompressible gas was developed. This model was used to give answers to the following two questions: How many holes are needed, assuming a constant back pressure, to get a homogeneous gas flux along the plasma column? What is the maximum size of the holes to guarantee the constant back pressure?

Technically it is easier to produce a showerhead with a circular cross section and with circular holes. However for the modelling a square cross section for tube and holes is

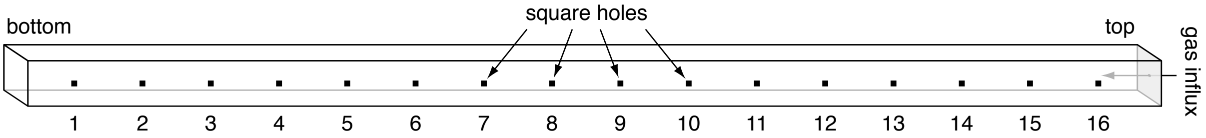

Figure 5.7: Schematic view of the 3D model showerhead tube.

assumed. A schematic view of the model tube with a width of $w = 2\,\mathrm{cm}$ and a length of $l = 50\,\mathrm{cm}$ is given in figure 5.7.

The equation to be solved is the Navier-Stokes equation for an incompressible fluid ($\nabla \cdot \mathbf{v} = 0$):

$$\frac{\partial \mathbf{v}}{\partial t} + (\mathbf{v} \cdot \nabla)\mathbf{v} = -\nabla p + \frac{\eta}{\rho}\Delta \mathbf{v} + \mathbf{F}$$

where η is the dynamic viscosity of the gas, ρ the gas density and $\mathbf{F}$ the volume forces. The gas is taken as a Newtonian fluid, so the viscosity is taken as constant: $\eta_{\mathrm{gas}} = 2 \cdot 10^{-5}\,\mathrm{Pa\,s}$. Since no variation of the resulting flux and pressure profile depending on the density can be found, the density is taken as a constant value: $\rho_{\mathrm{gas}}(0.01\,\mathrm{mbar}/200°\mathrm{C}) = 1.03 \cdot 10^{-5}\,\mathrm{kg\,m^{-3}}$. The time dependent term is set to zero as a stationary solution is required. The volume forces, mainly due to gravity, can be neglected in the pressure range used here.

The boundary conditions are defined by the given gas flux into the tube and the pressure in the reactor, defining the pressure at the holes. To avoid irregularities close to the in-flux boundary, the gas velocity distribution on this surface is defined as:

$$\mathbf{v}(x, y) = f \cdot 36[(s_1(1 - s_1) \cdot s_2(1 - s_2)] \tag{5.1}$$

where f is the total in-flux and $s_1 = x/w = [0, 1]$ and $s_2 = y/w = [0, 1]$ are two boundary coupled variables giving the relative position of a point (x, y) of the square surface boundary. Equation 5.1 leads to a velocity profile equal to zero at the surface boundary edges, respecting the zero velocity at the inner tube walls given by Navier-Stokes. The pressure defining the boundary condition at the out-flux holes is given by the pressure measured in the reactor at the corresponding gas flux.

In figure 5.8a the integrated gas fluxes through holes with different size and a total gas in-flux of 300 sccm are shown. It can be seen that with holes having a side length of $w = 0.5\,\mathrm{mm}$ a mainly homogeneous flux distribution is found with a homogeneity of $h = 1.3\%$. Furthermore this value of homogeneity rather depends on small fluctuations of the simulation and not on real flux variation from top to bottom position.

In figure 5.8b the pressure profiles found with four different total in-fluxes and holes with $w = 0.5\,\mathrm{mm}$ are given. The pressure varies by less than 1 ‰ from top to bottom in the tube with all in-fluxes analysed. Therefore it seems to be adequate to produce a tube with an inner diameter of 2 cm and 16 equally spaced holes with a diameter of 0.5 mm.

Growth rate homogeneity improvement with linear gas injection

In figure 5.9 ex-situ growth rate measurements made on several glass and Si wafer samples are shown positioned at 7 cm from the reactor axis. In the case of a circular gas

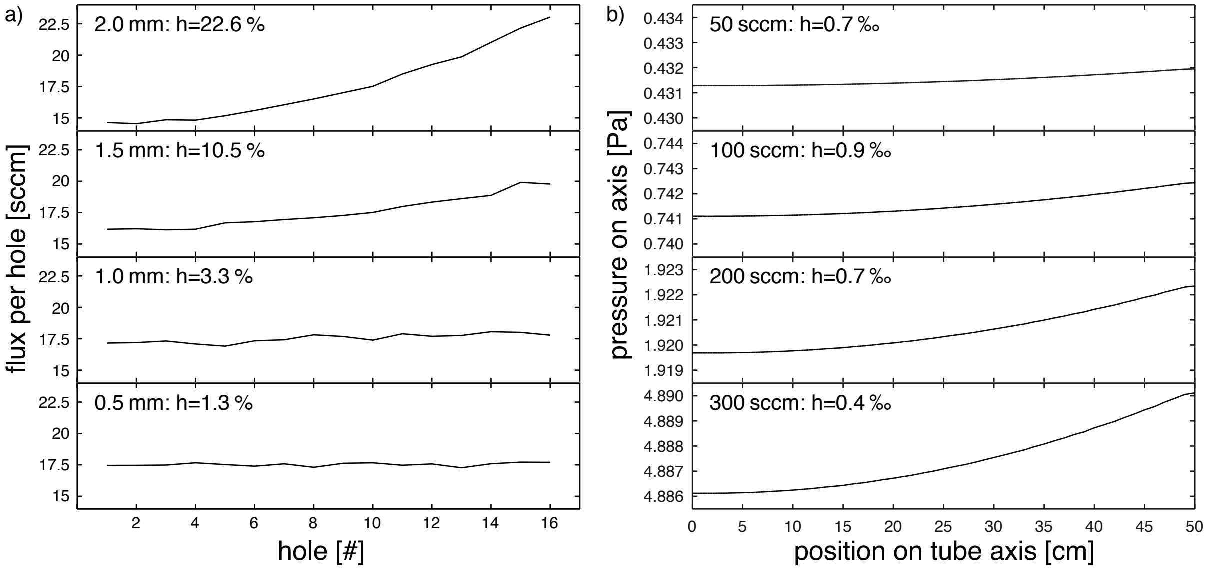

Figure 5.8: Simulation results for the hole out-flux and the pressure on tube axis: a) Reducing the size of the holes leads to a homogeneous flux distribution along the linear showerhead; b) With a hole side length of $w = 0.5\,\text{mm}$ a pressure variation of less than 1 % is found for different total influxes.

injection, the deposition rate for high silane fluxes ($\phi_{\text{SiH}_4} \geq 150\,\text{sccm}$) decreases strongly with distance from the position of gas injection (cf. figure 5.9a). In section 4.3.2 it was shown, that the concentration of Si^+ ions decrease for a $\phi_{\text{SiH}_4} > 100\,\text{sccm}$. This effect is also due to the use of a circular gas injection, as the OES measurements were performed at a height of 30 cm (cf. figure 5.9a) where the deposition rate also shows a saturation.

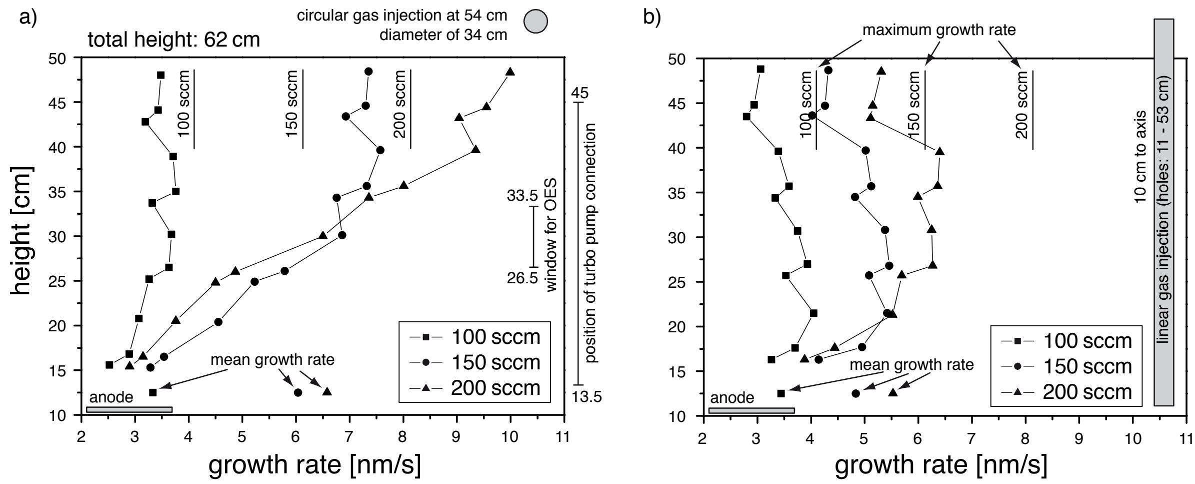

Figure 5.9: Ex-situ growth rate measurements with an alpha-step device in the case of a) circular gas injection in the upper part of the reactor and b) linear gas injection along the plasma column. The mean growth rates as well as the theoretical maximum growth rates are indicated.

With a linear gas injection (figure 5.9b) the deposition rate is much more uniform vertically, except in the case of $\phi_{\mathrm{SiH}_4} = 100\,\mathrm{sccm}$, where neither the homogeneity nor the mean growth rate has been substantially changes. Nevertheless the results show clearly that the linear gas injection is the only way to get homogeneous high deposition rates. The indicated maximum growth rates are calculated by assuming a total and homogeneous deposition of the injected silane on a cylinder with a radius of 7 cm. Comparing these calculated maxima with the actually measured growth rates, shows that 20–30 % of the silane is not deposited and lost to the pumps. Therefore other reactor improvements are necessary for a more efficient use of the precursor gas.

The measured maximum growth rates of about 6.5 nm/s measured in the linear case are more than two times higher than other reported deposition rates of μc-Si:H [53]. Even higher rates are imaginable when the silane influx is further increased. However, with an increasing silane flux the pressure in the reactor increases strongly (cf. also section 5.4). This then leads to a shortening of the plasma column, which affects the vertical homogeneity of the deposition rate. Figure 5.10 shows again the growth rate measurements with the linear gas injection together with photos of the plasma flame for 100 sccm, 150 sccm and 200 sccm of silane, respectively. In the case of 200 sccm of silane the pressure rose to 0.021 mbar and the plasma column ends around a height of 20 cm, showing a waisted shape. This is exactly at the position where the deposition rate strongly decreases. The plasma just above the anode apparently has not the same efficiency in silane decomposition than the column above the waist.

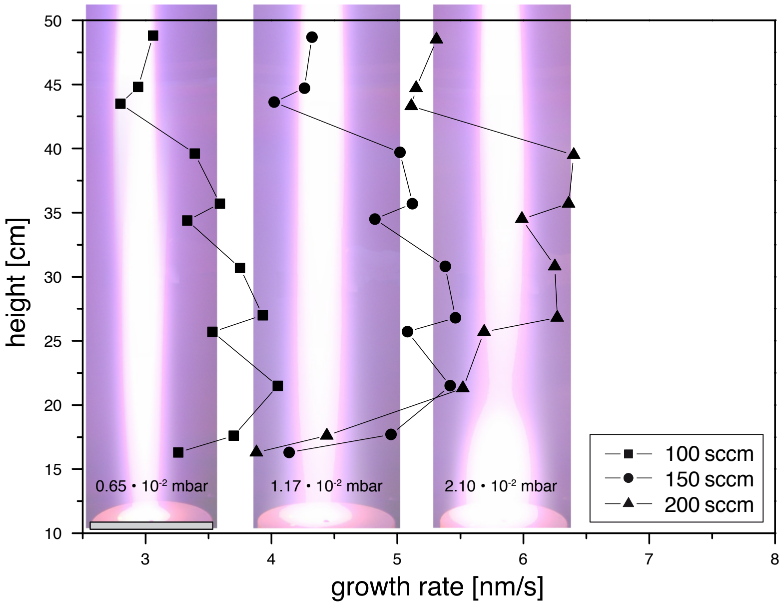

Figure 5.10: Ex-situ growth rate measurements in the case of a linear gas injection along the plasma column. The photos of the plasma flames correspond to the three different silane fluxes.

To study the effect of the gas pressure on the plasma column length, the lengths of several types of plasma and at variable pressure were measured. The results are shown in figure 5.11. The indicated maximum length is the distance between electron source and anode. The first interesting result to mention is that regardless of the gases used, the column lengths measured follow the same trend.

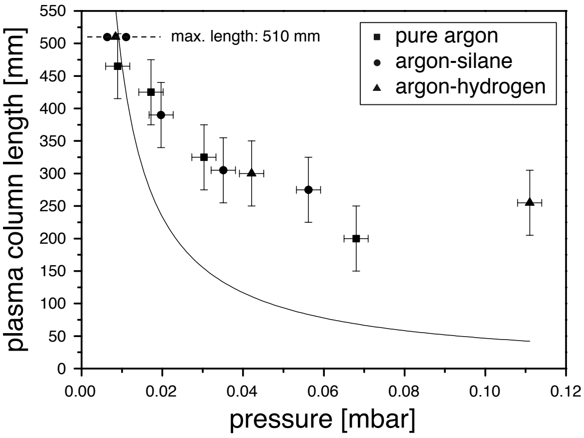

Figure 5.11: Plasma column length depending on gas pressure in the reactor. The indicated curve represents the simple model of a length depending only on the mean free path as a function of pressure ($\lambda = \lambda(p)$)

The indicated curve passing below the measured points is the attempt to find a dependence of the column length and the pressure dependent mean free path of the fast electrons produced in the electron source. The electron density at a certain distance from the ionisation source can be calculated as

$$n_{\mathrm{e}}(x) = n_{\mathrm{e},0} \exp\left(-\frac{x}{\lambda(p)}\right), \tag{5.2}$$

where x is the distance to the electron source, $\lambda(p) = kT/p\sigma$ is the mean free path and σ is the electron-neutral collision cross section. To find the length of the plasma column, the end of the column is defined as to point where only 1 % of the initial electron density is found. So equation 5.2 can be written as

$$\ln\left(\frac{n_{\mathrm{e}}(L)}{n_{\mathrm{e},0}}\right) = \ln\left(\frac{1}{100}\right) = -\frac{Lp\sigma}{kT},$$

and finally the length of the flame is found as

$$L(p) = -\frac{kT}{\sigma}\ln\left(\frac{1}{100}\right)\cdot\frac{1}{p}.$$

Obviously the plasma column length depends not only on electron loss due to electron-neutral collisions. It is very likely that the magnetic field, not included in the above mentioned calculations, is the reason for the discrepancy between measurements and fit.

5.2.2 Growth rate dependence on other system parameters

To get a better understanding of the deposition process, the dependence of the deposition rate of silicon on several system parameters was also investigated: Distance to the reactor axis, magnetic field strength and discharge current. All the measurements presented in this section were made with the circular gas injection and the substrates placed at a height of 28 cm.

In figure 5.12a the measured growth rate as a function of the sample's distance to the reactor axis is presented. The positions 1 and 3 refer to the bars at different angular positions for attaching the substrate holders (cf. figure 1.8). A flux of 200 sccm of silane was injected. The indicated theoretical maximum is calculated by assuming a total and homogeneous deposition of the injected silane on a cylinder with a given radius, leading to a $1/r$-dependence. The fact that the more distant samples reach this limit or even pass it, is principally due to the vertical inhomogeneity coming from the circular gas injection. Nevertheless the calculated theoretical maximum represents relatively well the measured growth rates, except for the samples very close to the plasma. Comparing the films produced (cf. figure 5.12b), it is observed that the films deposited close to the plasma are milky, which indicates that they are very porous, whereas the films deposited with at least two centimeters of gap to the plasma are of a good structural quality. The samples close to the plasma are exposed to a flux of electrons, radicals and ions highly energetic and reactive, counteracting the deposition process by etching away the film. This shows that is difficult to find a good balance between high deposition rate close to the plasma and a silicon film useful in solar cell technology.

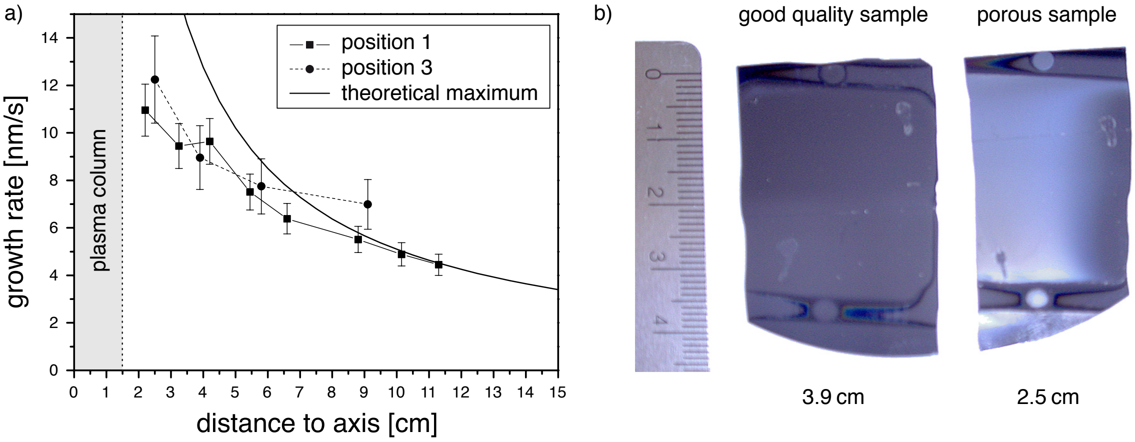

Figure 5.12: a) Growth rate as a function of the radial distance to the reactor axis for two different angular positions (cf. figure 1.8); b) Photos of two different films deposited at different distances to the axis. The sample on the right has a milky appearance, indicating a high film porosity.

The second parameter studied was the applied magnetic field. As shown in section 4.2, the magnetic field has an important effect on the shape, namely the radius of the plasma column. The deposition rate itself directly depends on the amount of radicals produced in the plasma and diffusing towards the sample. So when having more primary electrons trapped by the magnetic field in a narrower plasma column, the collision frequency will rise and lead to a higher ion and radical density, used for the deposition process.

In figure 5.13a the growth rate measured as a function of the magnetic field is presented, using 200 sccm of silane. It shows a strong increase of the growth rate between 30 and

45 G and a tendency to saturate with higher field strengths. This, and the fact that for the samples positioned at 9 cm the saturation is slightly stronger than for those at 5.5 cm, justifies the explanation of the above-mentioned oppositional effects.

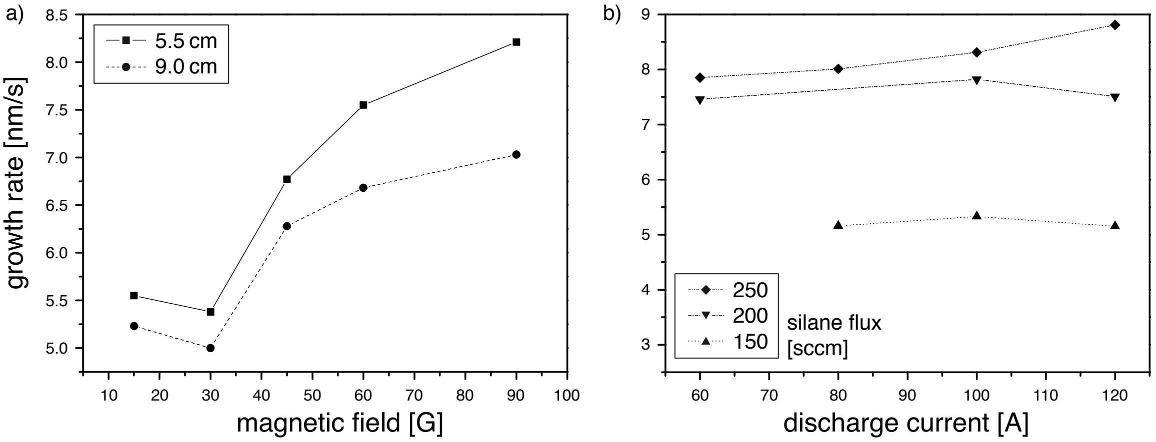

Figure 5.13: a) Deposition growth rate as a function of the applied magnetic field at two different radial distances; b) Deposition growth rate as a function of the discharge current in the plasma for various silane fluxes.

The third parameter studied was the discharge current. In figure 5.13b the growth rate is given as a function of the applied current for three different silane flow rates. It can be seen that the deposition rate is nearly constant for 150 and 200 sccm of silane and rises by only 12 % for 250 sccm when doubling the current. This proves the results presented in section 4.3 showing the very high efficiency of the studied plasma to dissociate the silane molecules. An advantage of this near independence of the discharge current is the opportunity to vary the discharge current in order to control other film properties, such as crystallinity, without losing growth rate.

5.2.3 Crystallinity and Si film structure

For single junction μc-Si:H solar cells as well as for a-Si:H/μc-Si:H tandem cells Vetterl *et al.* [56] found a maximum conversion efficiency with a microcrystalline layer near the transition to a-Si:H. So a Raman crystallinity of 40–60 % is assumed to be optimal for highly efficient solar cells. However, if a PECVD system is able to deposit silicon films with a wider range of crystallinity, this can be very useful for industrial applications. Especially for the production of tandem cells, where a-Si:H and μc-Si:H films are needed, it is favorable to have only one system producing both types of layers at elevated deposition rate. The results presented in this section show that with a high current DC arc plasma it is possible to produce silicon films with Raman crystallinity from 0–80 %. Furthermore the films produced are found to consist of crystallites with a size less than 10 nm, therefore they are rather nc-Si:H.

Like the growth rate, the Raman crystallinity ϕ_c was studied under different system parameter changes, such as silane flux, discharge current, radial distance to the reactor axis and the use of different gas injection. In figure 5.14a the ϕ_c as a function of discharge current and silane flux is shown. The silicon films were deposited on silicon wafers positioned at 6 cm from the axis and at a height of 28 cm on position 1. The graph principally shows that it is possible, by adapting the parameters concerned, to deposit silicon films from 100 % amorphous to μc-Si:H with $\phi_c \approx 60\,\%$. On the other hand it shows also that it is probably not possible to deposit amorphous silicon with high deposition rates as ϕ_c is constantly high for 250 sccm of silane.

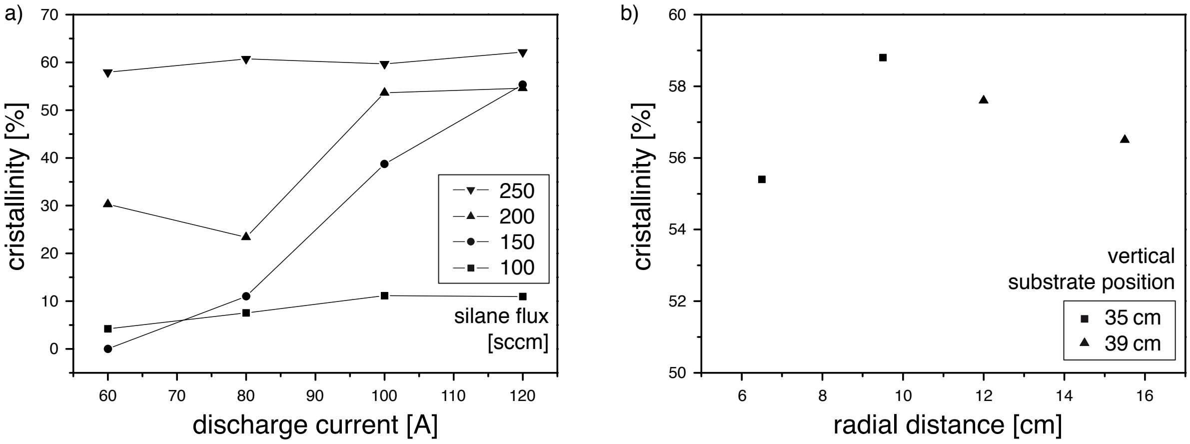

Figure 5.14: a) Raman crystallinity as a function of discharge current and various silane fluxes; b) Raman crystallinity as a function of radial distance to the reactor axis.

In the last section the strong dependence of the film growth rate on the radial position of the substrate was presented. Figure 5.14b shows that for the Raman crystallinity this is not the case. The films measured were deposited with 120 A discharge current and 200 sccm of silane. The variation of 4 % in crystallinity along the radial position is small compared to the variation of about 30 % for the same silane flux and a variable discharge current.

A homogeneous crystallinity is as important as a homogeneous film thickness for a marketable solar cell. The maximum variation for both must not exceed 10 %. In figure 5.15 the measured crystallinity along the plasma column for both types of gas injections is presented. The silicon wafer substrates (filled symbols) and the glass substrates (empty symbols) used for the deposition are installed at position 1, 7 cm from the axis. Unlike the growth rate, ϕ_c shows an absolute variation of less than 20 % for any given silane flux and substrate type, and there is no important difference between the two types of injections. A further comparison with the growth rate measurements shown in figure 5.9 reveal the opposite behaviour: when the deposition rate for a circular gas injection increased by more than a factor of three in the top region of the reactor but is found to be nearly constant near the anode, then the crystallinity proportionally increases by about 75 % near the anode but only by about 20 % at the top. In the case of the linear gas injection a similar behaviour is observed. The maximum crystallinity of 80 % is found in the lower part of the reactor and for very high silane flux, the conditions where the growth rate shows a strong decrease in figure 5.9b.

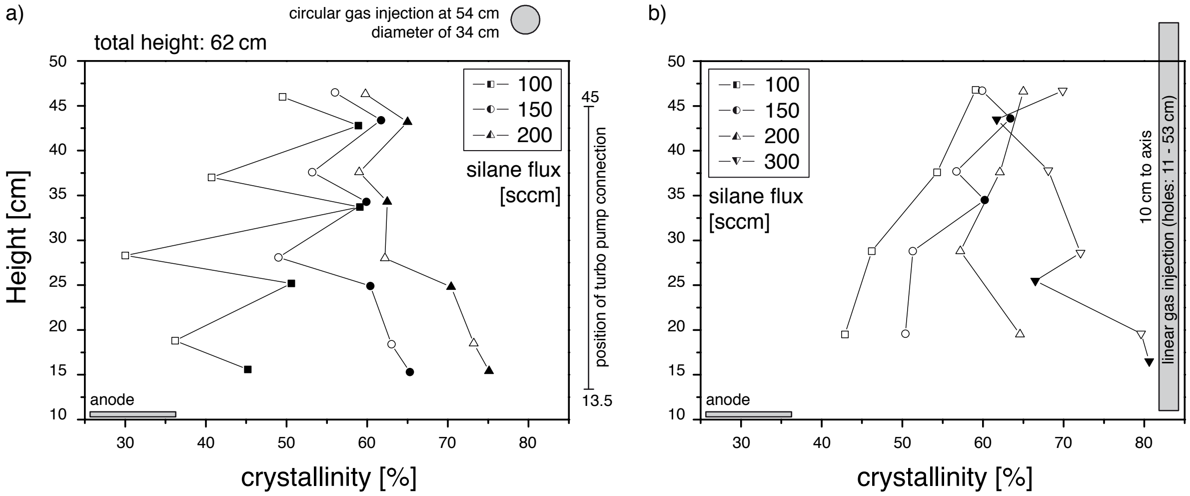

Figure 5.15: Vertical profiles of Raman crystallinity measured on silicon wafer (•) and glass (◦) substrates and for various silane fluxes. a) With a circular gas injection; b) with a linear gas injection.

All this indicates that the deposition rate and the Raman crystallinity of the deposited silicon films depend on each other. So an improvement in the vertical homogeneity of one would most likely improve the homogeneity of the other. Further reactor improvements in terms of homogeneity are presented in section 5.3.

The Raman crystallinity measurement with the Micro-Raman spectroscopy gives only a general estimation of the microcrystalline proportion of the total film volume. Therefore TEM images of the silicon films were made for a more profound knowledge of the film structure. Figure 5.16 (already presented in section 2.2.1) shows a TEM image of a typical μc-Si:H film deposited on a silicon wafer. The crystallites found in the microcrystalline layer have a width of about 10 nm. Therefore the film is rather nanocrystalline than microcrystalline, which is reported to be an interesting material for photovoltaic applications [50].

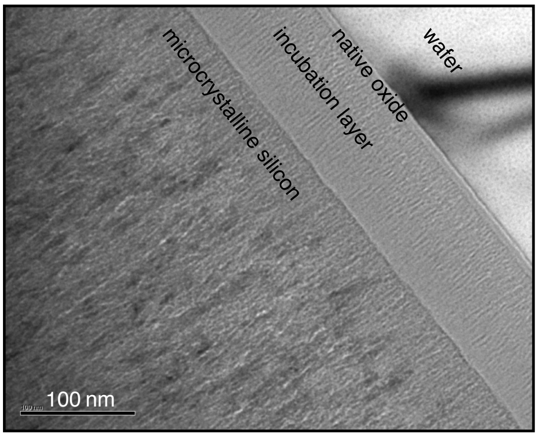

Figure 5.16: TEM image of a silicon film showing four different layers: The silicon wafer substrate, a native oxide layer, an incubation layer deposited during the substrate heating process and the microcrystalline layer.

5.2.4 FTIR analysis for quantification of impurities

As already discussed for the hard SiC coatings in section 5.1.2, one of the major problems was the incorporation of oxygen in the deposited films during the process. The BAI reactor is non-UHV and is used now for more than 15 years in a variety of projects. Therefore a complete leak test and cleaning of the reactor was performed, leading to a final base pressure of $p_\mathrm{b} < 10^{-6}$ mbar and a pressure rise of about $5 \cdot 10^{-5}$ mbar/min when the valve to the pumping system is closed.

After these first improvements of the system, FTIR measurements have shown that oxygen can still be found after the film deposition, and that the concentration increases strongly in time. Figure 5.17a shows three FTIR absorption spectra, one measured immediately after the deposition process (EPFL), one measured after several days (Neuchâtel) and one measured on a nearly oxygen free film ("O_2-free"), when an intense outgassing is performed (EPFL). In order to eliminate as much as possible the oxygen incorporation in the deposition process, two modifications were made: (1) The samples were not only heated to about 300°C in an argon plasma before the deposition was started, but the reactor was outgased during at least six hours while heated with a hydrogen plasma and (2) for the exchange of the coated samples with clean ones, the reactor was vented with nitrogen instead of air as before. The result of these efforts is shown in figure 5.17a as an FTIR spectrum of a nearly oxygen-free silicon film measured immediately after deposition.

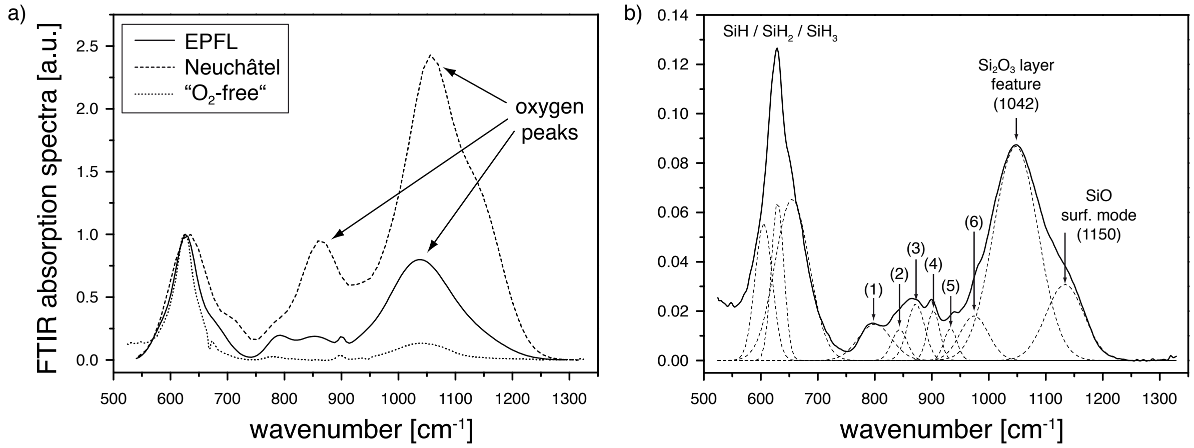

Figure 5.17: a) FTIR absorption spectra measured immediately after the deposition process (EPFL and "O_2-free) and after several days (Neuchâtel); b) Typical FTIR spectrum of an oxidised Si:H film showing different peaks related to Si-H (2, 3) and Si-O (1, 4–6) vibrations.

However, the increase of oxygen concentration in time is still observed and it would lead to a strong degradation of a solar cell made out of these films. Furthermore this increase of oxygen concentration in the film is a sign of a porous structure, having a density too low for good solar cell applications. The SEM images presented in figure 5.18 show the fine columnar structure of the microcrystalline films deposited on a silicon wafer. Compared to films deposited in the same reactor but at pressures of 1.5 mbar and higher temperatures by David Franz [57], the surface of the film shows a low surface roughness

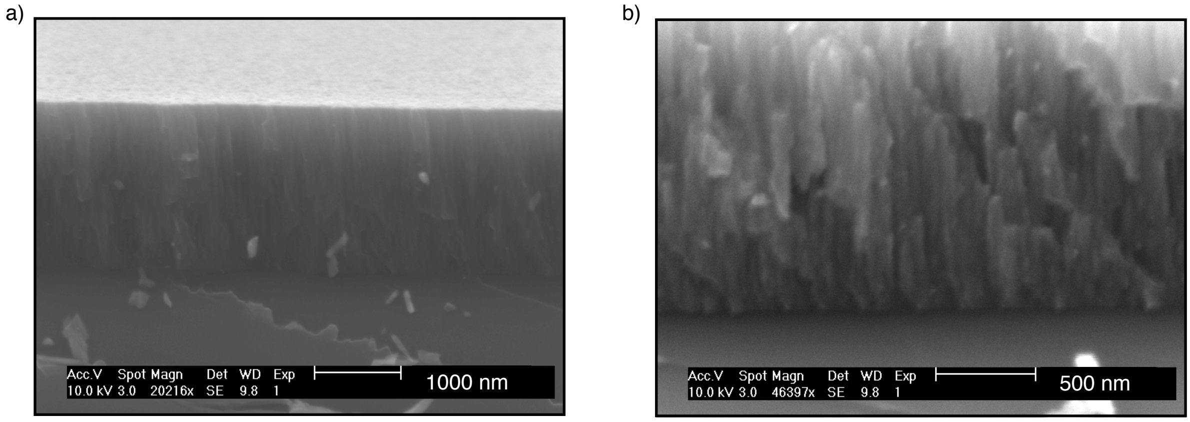

Figure 5.18: SEM images of a film deposited with $I_{\mathrm{lp}} = 120\,\mathrm{A}$ and $\phi_{\mathrm{SiH_4}} = 200\,\mathrm{sccm}$. a) SEM image of the columnar crystal structure and the smooth surface of the film; b) SEM image showing a high number of cracks between the cylindrical crystallites, which makes the film susceptible to degradation due to oxygen penetrating into the film.

(cf. figure 5.18a). The pressure in our process, lower by a factor of 100, prevents the silane radicals from forming clusters or powders before they are deposited on the substrate.

Figure 5.18b shows the porous structure of the microcrystalline film. The high number of cracks between the cylindrical crystallites lets oxygen penetrate into the film, leading to a degradation. Therefore a study of the oxygen concentration in different films was made by analysing the evolution of oxygen related FTIR peaks. For a deconvolution and integration of the oxygen peaks, the absorption spectra had to be corrected from the interference fringes background as already explained in section 5.1.2. A corrected and deconvoluted spectrum is shown in figure 5.17b. The study on relative oxygen concentration was made by summing the integrated Si_2O_3 peak ($1042\,\mathrm{cm^{-1}}$) and the SiO surface mode peak ($1150\,\mathrm{cm^{-1}}$) [58]. The three peaks around $650\,\mathrm{cm^{-1}}$ and peak 2 and 3, related to SiH vibrations, were not changing in time. Peaks 1 and 4–6, found between 800–$1000\,\mathrm{cm^{-1}}$, represent different vibrations of SiO bonds. Those were not taken into account for the estimation of oxygen concentration in the silicon films.

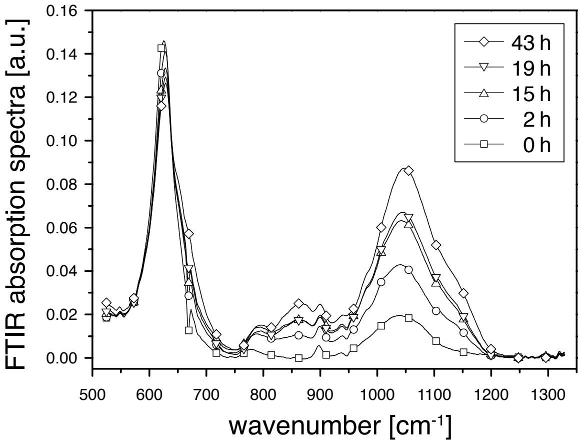

Figure 5.19: Evolution in time of FTIR absorption spectra measured immediately after the deposition and after 2, 15, 19 and 43 hours respectively. Strong increases in peak size for the Si_2O_3 peak ($1042\,\mathrm{cm^{-1}}$) and the SiO peak ($1150\,\mathrm{cm^{-1}}$) were found.

Figure 5.19 shows five absorption spectra measured immediately after the deposition and 2, 15, 19 and 43 hours after the deposition respectively. They show a strong increase in peak size for the Si_2O_3 peak ($1042\,cm^{-1}$) and the SiO peak ($1150\,cm^{-1}$). In figure 5.20 the sums of the integrated peaks, measured on two different types of samples and normalised to the initial value, are presented. Sample 103 is a nc-Si:H film, produced in standard plasma conditions ($I_{pl} = 120\,A$, $p = 0.012\,mbar$, $\phi_{SiH_4} = 150\,sccm$). Sample 113 was produced under the same conditions, but after the first layer of nc-Si:H the plasma current was reduced to 60 A in order to deposit an amorphous cover layer with a thickness of about 300 nm. The amorphous cover layer should prevent the oxygen from penetrating into the microcrystalline film.

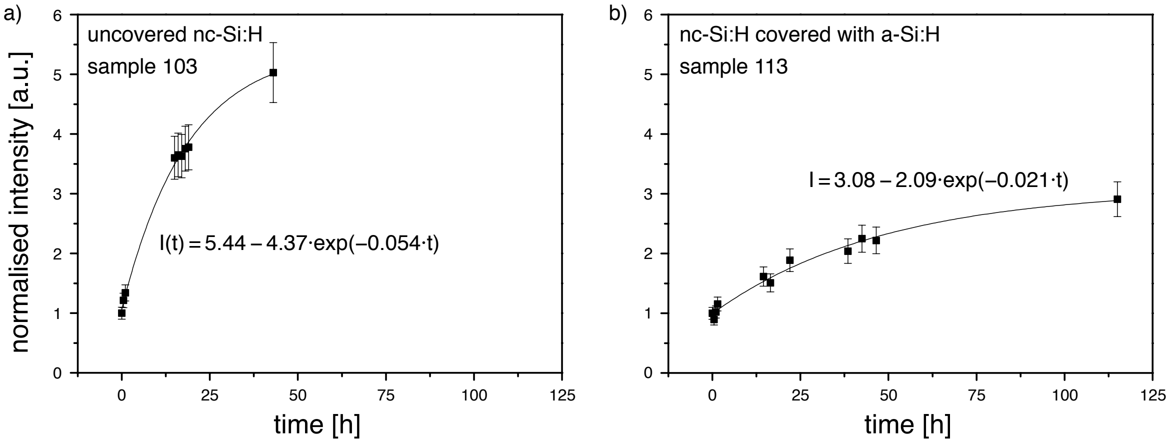

Figure 5.20: Normalised evolution of oxygen concentration measured with FTIR on a) an uncovered nc-Si:H film and b) a nc-Si:H film with a 300 nm amorphous cover. An error of 10 % is assumed due to the background elimination, the spectra deconvolution and the peak interpolation.

An exponential fit of the two measured curves show a reduction of 45 % in the capacity to absorb oxygen and the process of absorption is slowed down. However, an increase of more than a factor of three from a starting value, which is already too high, is not acceptable for technical applications. Further technical improvements would be necessary to increase the film density in order to prevent oxygen absorption from the start.

Nevertheless, the improvements described in this section lead to a substantial improvement in the film quality. Figure 5.21 shows three glass samples with silicon deposits of different quality and approximately the same thickness. Sample 98 was deposited without the long outgassing procedure and the same process conditions as sample 103. Sample 106 was deposited in conditions like sample 113, with an amorphous cover of 300 nm. The colour of the three samples indicates that the reduction of oxygen has substantially improved the capacity of light absorption.

Fourier-transform photocurrent spectroscopy (FTPS) [55] was used to measure the optical absorption coefficient α arising from the electronic transition in three different silicon films. The samples analysed were deposited in conditions comparable to no. 98, with 100 sccm, 150 sccm and 200 sccm of silane respectively for samples 100, 101 and

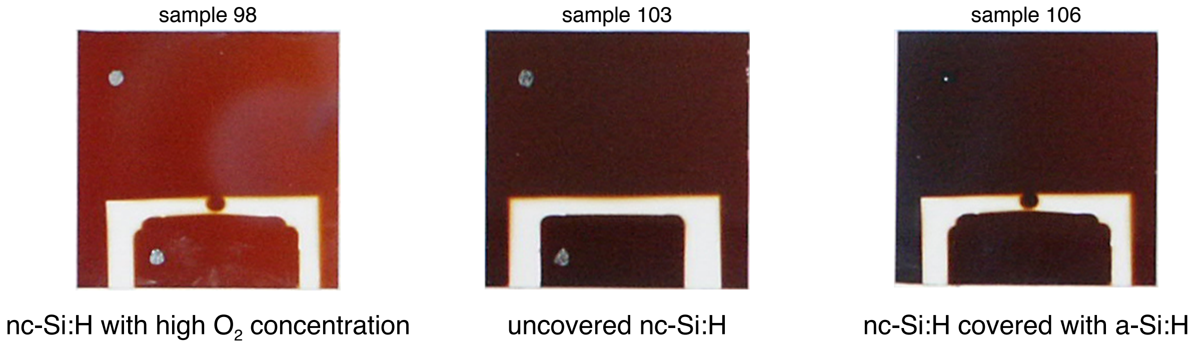

Figure 5.21: Three samples of nc-Si:H films: sample 98 shows a film with a high O_2 concentration due to a too short outgassing procedure, sample 103 shows an uncovered nc-Si:H film and sample 106 a nc-Si:H film covered with a 300 nm amorphous layer.

102. The normalised FTPS spectra given in figure 5.22 show an absorption characteristic comparable to crystalline silicon for photon energies higher than 1.2 eV. The main problem of the three studied films is the high absorption coefficient below 1.0 eV. The value of the optical absorption coefficient at photon energy $E = 0.8\,\text{eV}$ scales roughly with the density of dangling bonds. $\alpha(0.8)$ of the three films is one to three orders of magnitude higher than in typical microcrystalline films, indicating a high defect density and leading to electron losses in recombination. Therefore this type of material is not compatible for use in microcrystalline silicon solar cells, and the question remains if it is possible to produce dense, defect free nc-Si:H or μc-Si:H films with low contamination with a high current DC arc plasma.

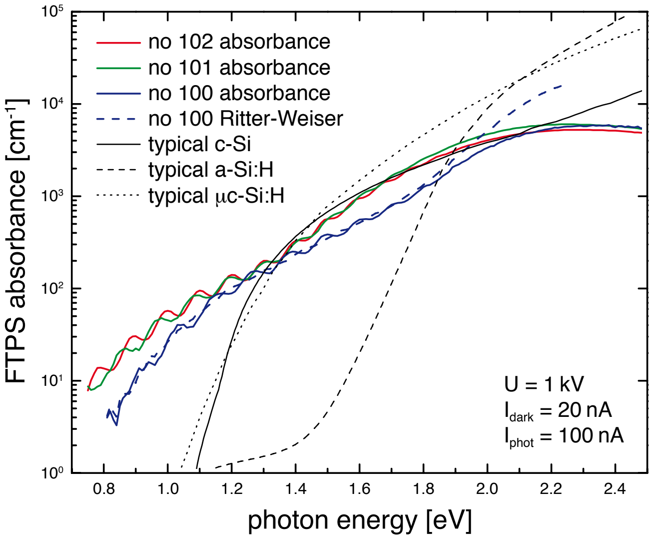

Figure 5.22: Normalised FTPS spectra measured on three different samples. For comparison the spectra of typical c-Si, a-Si:H and μc-Si:H are also plotted.

5.3 Deposition on large size glasses (37 × 47 cm^2)

Up to now the various silicon films had always been deposited on small samples, either silicon wafers or glass substrates. For an industrial application it is necessary to deposit large size substrates. Therefore the BAI reactor was used to studied its ability to deposit silicon films on large size glasses (37 × 47 cm^2), having the same size as the glasses used in the KAI-S system [4].

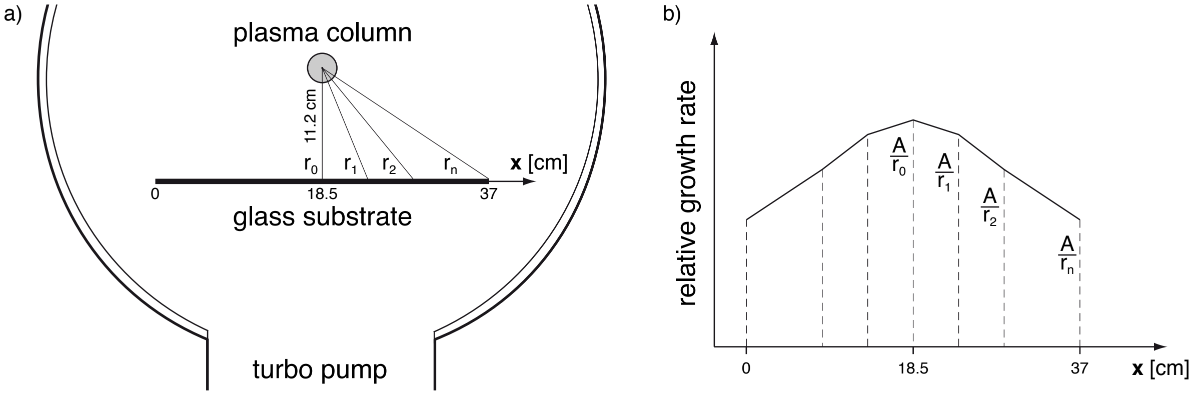

Figure 5.23: a) Schematic of the glass position in the reactor for the growth rate calculation depending on the distance to the plasma column; b) Relative growth rate calculated from the growth rate measurement in the center of the glass ($x = 18.5\,\mathrm{cm}$)

The first silicon deposition on large size glasses was made with glasses installed at position a (cf. figures 1.8 and 5.23) and a distance of 11.2 cm from the reactor axis. The plasma parameters were: $I_{\mathrm{pl}} = 100\,\mathrm{A}$, $p = 0.006\,\mathrm{mbar}$ and $\phi_{\mathrm{SiH_4}} = 100\,\mathrm{sccm}$. The deposited film showed a thickness inhomogeneity in both horizontal and vertical direction. Figure 5.24a presents the growth rate measurements performed with a NanoCalc 2000, a spectroscopic reflectometer from Micropack. The horizontal variation of the profile shown is assumed to be an effect of increasing distance to the plasma column, explained in figure 5.23. Different points on a horizontal line on the glass have variable distances to the plasma (r_0, r_1, …, r_n). As shown in section 5.2.2 the deposition rate shows a $1/r$-dependence, then the deposition rate decreases for increasing distance to the plasma (cf. figure 5.23b).

By using in the calculation the measurements along the line at $x = 16\,\mathrm{cm}$ and calculating the growth rate with the method explained above for the complete surface, the contour plot given in figure 5.24b is found. The calculated profile is quite similar to the measured one, which proves that the horizontal variation of the growth rate is mainly determined by the geometry of the reactor. The only solution to overcome this inhomogeneity would be to move the substrate horizontally beside the plasma column, or to install several plasma columns in parallel.

The inhomogeneity in vertical direction however, has another source, it originates from diffusive effects due to deposition and therefore losses of silicon on the upper and lower cover of the BAI reactor. For a detailed analysis of these effects a simple 3D model for diffusion of one species was developed with COMSOL.

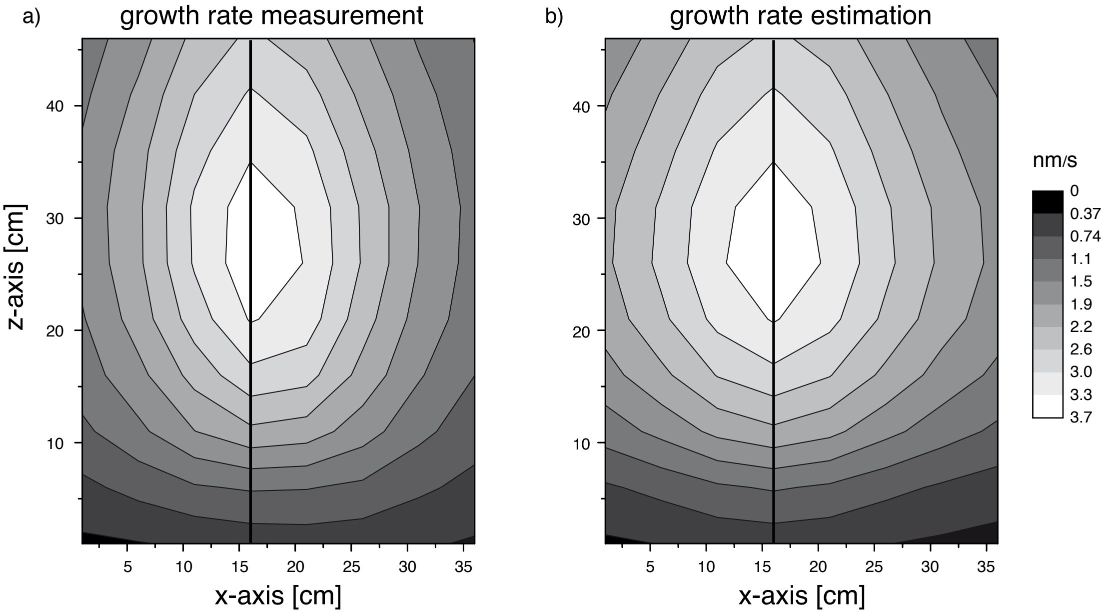

Figure 5.24: a) Growth rate measurement on a large size glass at position a (cf. figure 1.8) using interferometry; b) Estimation of the growth rate in horizontal direction using a $1/r$-dependence. Parameters: $\phi_{\mathrm{SiH_4}} = 100\,\mathrm{sccm}$, $I_{\mathrm{pl}} = 100\,\mathrm{A}$, distance from reactor center to glass: 11.2 cm.

5.3.1 Diffusive gas flow model and comparison with large surface depositions

The dependent variable in this model is the concentration c and the mass transport equation to be solved in a nonconservative case with an incompressible fluid is given as

$$\nabla \cdot (-D\nabla c) = -\mathbf{u} \cdot \nabla c$$

where D is the diffusion coefficient and $\mathbf{u}$ the velocity. The model geometry consists of a large cylinder closed at the top and bottom representing the reactor and a narrow cylinder representing the plasma column, which produces the silicon radicals for deposition (cf. figure 5.25). The boundary conditions in general are given by a zero concentration at the reactor walls, simulating the loss of the particles by deposition, and a constant outflux at the plasma column border. The simulation was used to see the effects that a large size glass or an additional volume limiting wall can have on the concentration c and the diffusive flux ϕ_{d}. It is also used to see the influence of the top and bottom cover of the reactor on ϕ_{d} along the z-axis.

The simulation presented in figure 5.25 shows a decrease of ϕ_{d} towards the top and bottom ends of the wall. This inhomogeneity along the vertical axis of the wall (red line) is caused by diffusive losses on the top and bottom surfaces of the reactor. In figure 5.26a the profiles of diffusive flux ϕ_{d} along this axis are presented for three different distances between the plasma column and the volume limiting wall. On a wall with a distance of 5 cm to the plasma the flux is constant between 20–50 cm, neglecting the noise produced by the simulation. By increasing the distance the profile of ϕ_{d} gets more and

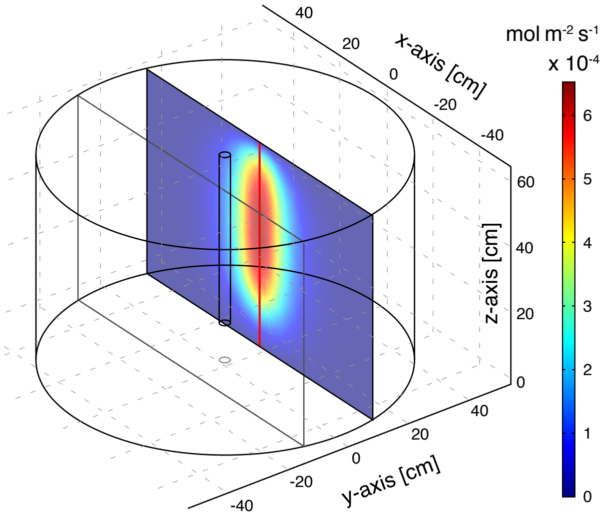

Figure 5.25: Schematic of the COMSOL model for convection and diffusion. A 2D profile of the resulting diffusive flux is presented in the case when two volume limiting walls are added with a distance of 11.2 cm to the central axis.

more inhomogeneous and the absolute value of ϕ_{d} decreases. In practice this leads to a decrease of the deposition rate because a higher proportion of the radicals, driven by diffusion, are lost to the top and bottom ends of the reactor by deposition.

The influence of the top and bottom surface of the reactor on the diffusion can be demonstrated with a change in the boundary condition. When the boundary condition on the top surface is changed from a zero concentration boundary to a symmetric boundary, which represents a semi-infinitely high reactor, the diffusive flux is constant close to this surface. In figure 5.26b the profile of ϕ_{d} for the two different top boundary conditions are presented, showing the expected behaviour.

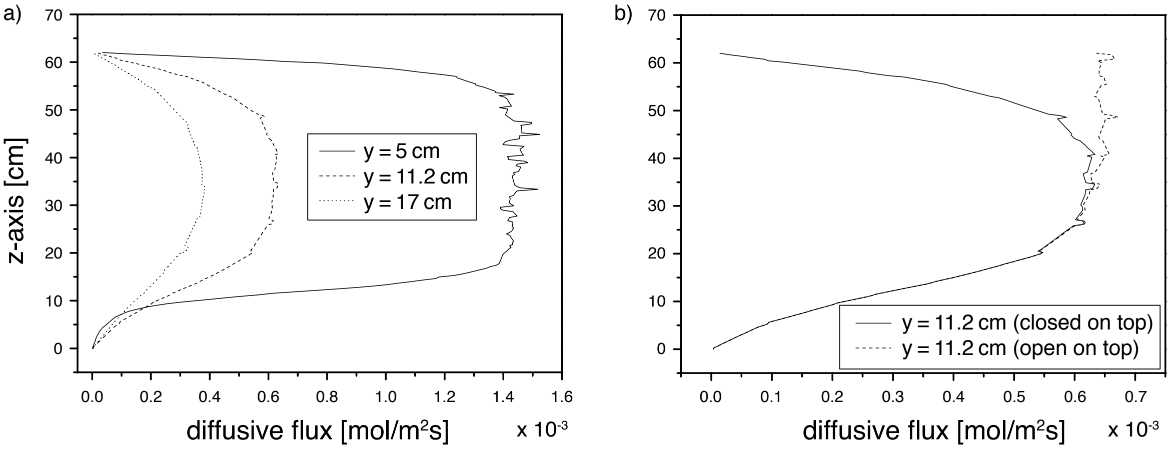

Figure 5.26: Simulation results of the diffusive flux. a) For three different distances of the volume limiting walls; b) Showing the difference between a top cover with zero concentration boundary or with an open wall boundary.

Comparing the growth rates measured on the large size glasses with the simulated diffusive flux, it can be shown that these are strongly correlated. Figure 5.27a shows the simulated diffusive flux on a virtual glass with the typical dimensions and set at position a, 11.2 cm from the plasma column. Except for the top region of the glass, the 2D profile are comparable to the growth rate measurement given in figure 5.24a. Figure 5.27b shows the comparison between growth rate and diffusive flux along central vertical axis (red line), adjusted on an axis with arbitrary units. The four different simulated profiles are found with (a) a typical glass as shown in figure 5.27a, (b) a larger glass with a size of $80 \times 55\,\mathrm{cm}^2$, (c) a glass separating the reactor completely into two halves (cf. figure 5.25) and (d) without any glass. The three profiles simulated with a glass substrate have the same shape as the measured growth rate profile, except for a position of $z > 35\,\mathrm{cm}$. The increase of the glass size partially corrects this gap between growth rate and ϕ_d, as the border effects found are shifted to a position out of interest. For the part between 0 and 35 cm the simulated diffusive flux shows the same shape as the growth rate measurements. The simulated diffusive flux in a reactor without any glass shows a profile which is flatter and does not decrease to zero for $z = 0\,\mathrm{cm}$.

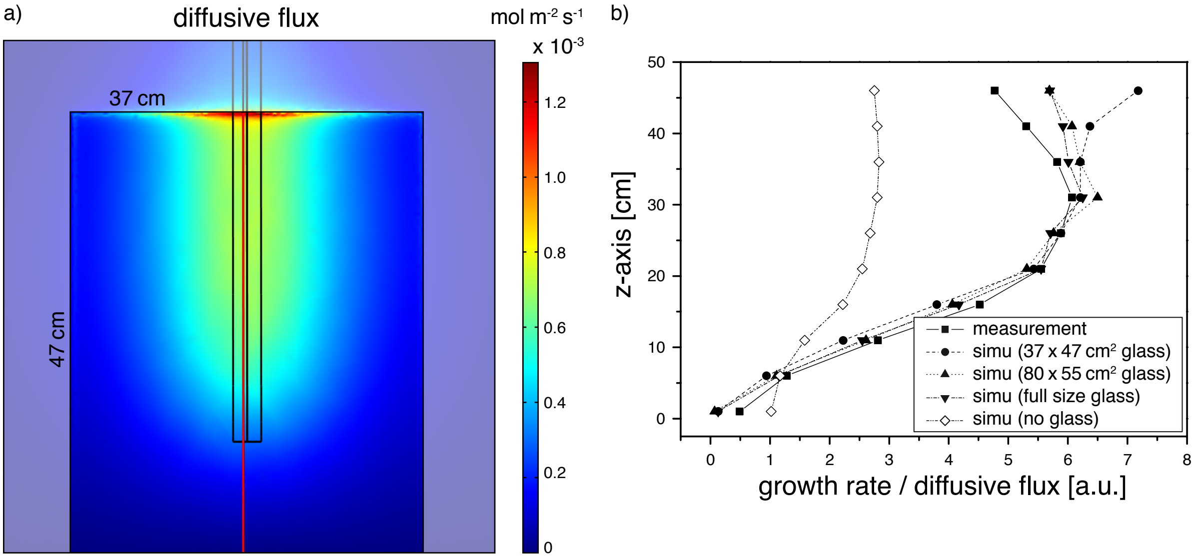

Figure 5.27: a) Simulation of diffusive flux with a large size glass set in the reactor at 11.2 cm from the axis; b) Central vertical profiles of measured growth rate and simulated flux showing the strong correlation between these two.

5.3.2 Reactor modification and deposition rate improvements

The simulations presented in the last section showed that for a maximum homogeneity in vertical direction it is necessary to set the substrates as close as possible to the plasma column and to decrease the dead volume of the reactor. Therefore a steel cage was designed and installed in the BAI reactor (cf. figure 5.28), acting simultaneously as a substrate holder for two glasses and as a volume limiting wall. The cage ranges from top to bottom of the reactor, letting the gas exit only through the slit on the left side towards the pumps. The chosen distance of 10 cm for the substrates to the reactor center

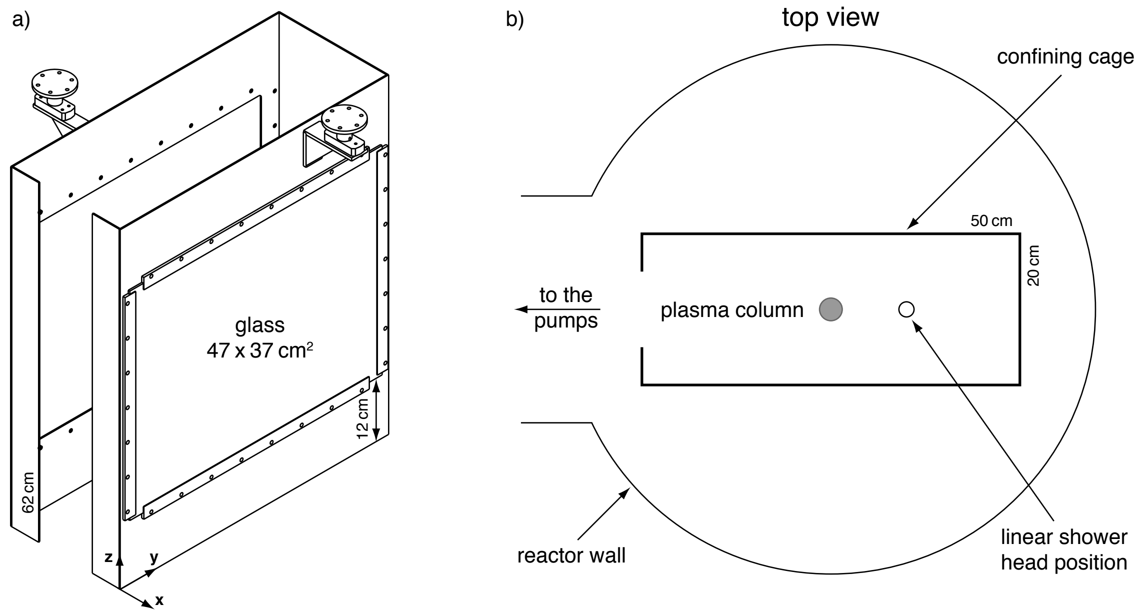

Figure 5.28: Cage reducing the dead volume and acting as a substrate holder for the large surface glasses ($47 \times 37\,\mathrm{cm}^2$).

is a compromise between good vertical homogeneity and protection of the glasses from breaking due to strong and irregular heating through the plasma.

In figure 5.29 the growth rate on a large size glass held by the cage is shown. The plasma used had the following parameters: $I_{\mathrm{pl}} = 100\,\mathrm{A}$, $p = 0.02\,\mathrm{mbar}$ and $\phi_{\mathrm{SiH_4}} = 200\,\mathrm{sccm}$. The maximum growth rate of 6.5 nm/s is comparable to the measurements pre-

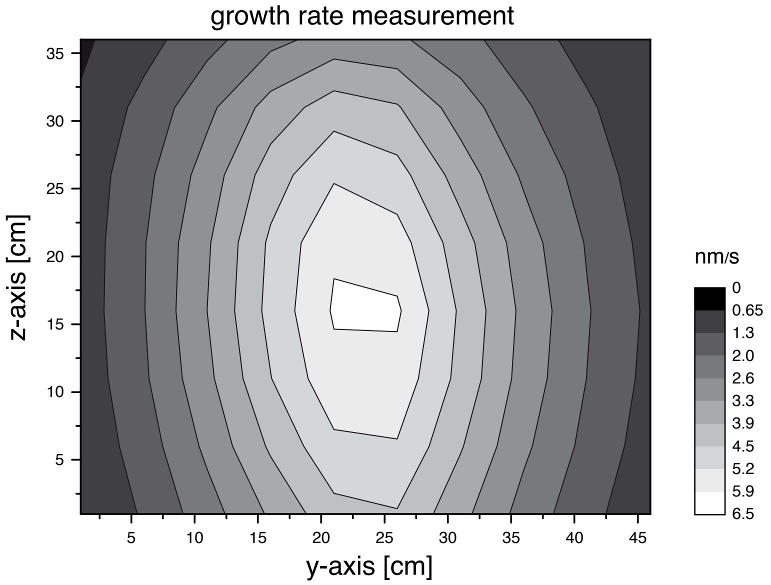

Figure 5.29: Growth rate measurement on a large size glass fixed in the cage using interferometry. The growth rate in horizontal direction strongly decreases to the borders.

sented in section 5.2.1 for the linear shower head with the same silane flux (cf. figure 5.9b). With the given distance of 10 cm to the reactor axis the growth rate profile measured in vertical direction is found as expected from the simulation shown in figure 5.26a. However, in horizontal direction the growth rate profile is more strongly peaked than in the measurements shown in figure 5.24a.

By using the method to calculate the radius depending growth rate from the measurements at $y = 23.5\,\mathrm{cm}$, the 2D profile as presented in figure 5.30a is found. This profile does visibly not fit the measured growth rate profile and decreases only by 55 % from the center to the left and right border whereas the measured growth rates decreases by 85 %. In figure 5.30b another growth rate estimation is shown. For its calculation the $1/r$ dependence of the growth rate was replaced by a $1/r^2$ dependence. The found 2D profile well fits the growth rate measurement profile shown in figure 5.29. This shows that with the cage the growth rate also depends on diffusive effects in horizontal direction, in contrast to the case of a single glass positioned in the reactor (cf. figure 5.24).

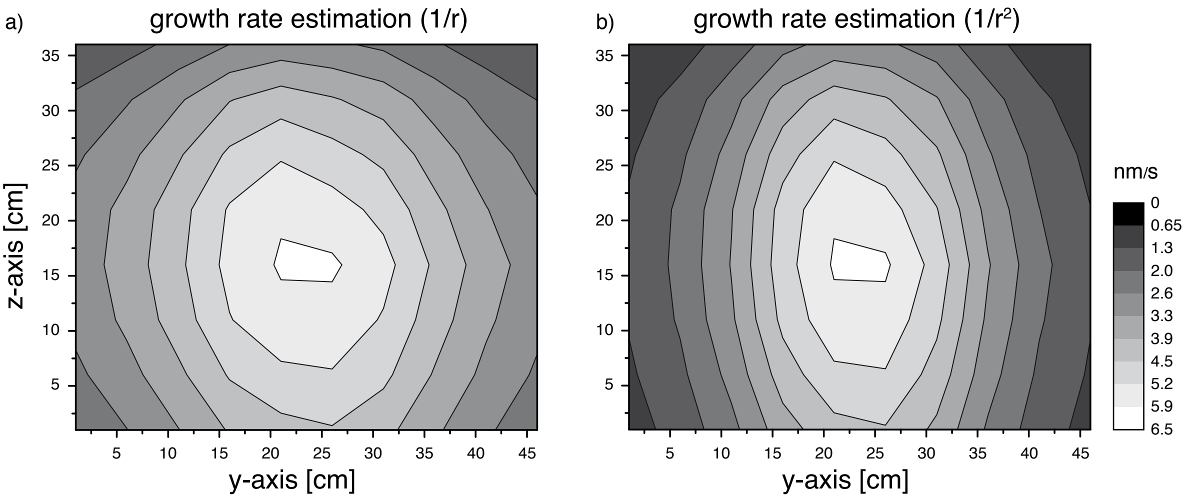

Figure 5.30: a) Growth rate estimation using a growth rate depending as $1/r$ from the distance to the plasma; b) Growth rate estimation using a growth rate depending as $1/r^2$ from the distance to the plasma.

5.4 Plasma efficiency estimation by simple pressure measurements

In this section a simple but powerful method to measure the silane dissociation efficiency of the DC plasma in the BAI reactor is presented. It will be shown that the DC plasma has a very high dissociation efficiency.

The starting point for the results presented in this section was a simple pressure measurement. In the BAI reactor, when used with silane for silicon depositions, it was observed that with a plasma switched on, the gas pressure increases non-linearly with increasing silane flux, but linearly when the plasma is switched off (cf. figure 5.31a). The reason for this important pressure difference is found in the turbo pump's selectively bad pumping of the light hydrogen molecules, produced by the dissociation of SiH_4. Figure 5.31b shows the strongly increasing pressure depending on the hydrogen flux. The pressure is measured with a Baratron pressure gauge connected to the 90°-angle valve, thus at the gas output of the reactor and away from the plasma. These hydrogen measurements show nearly no difference between the two cases studied, one without plasma and one with a plasma having a 120 A discharge current. In all these measurements a flux of 100 sccm of argon was set to the reactor, giving the base pressure of about 0.002 mbar without SiH_4 or H_2 flux.

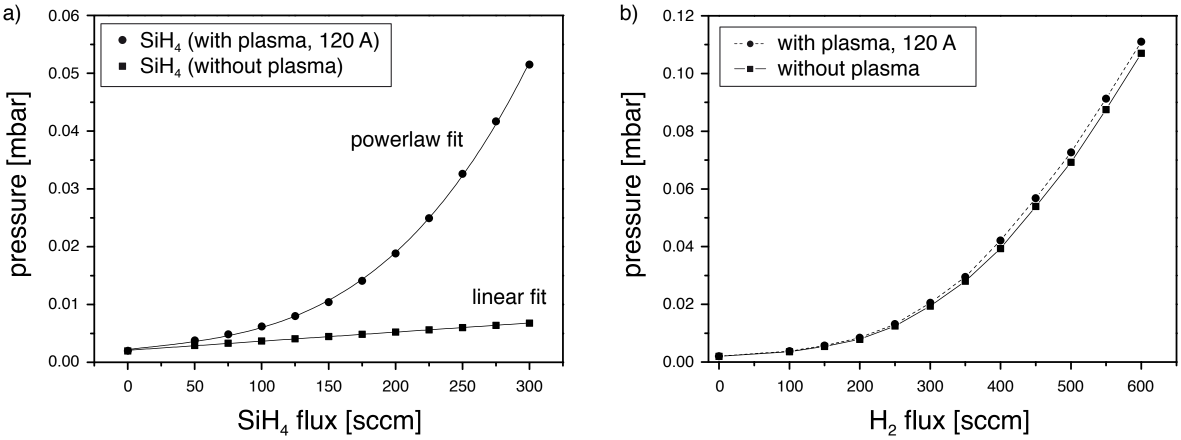

Figure 5.31: a) Large pressure difference in the BAI reactor, with and without a plasma respectively, for silane; b) Negligible pressure variation with and without a plasma when using hydrogen.

5.4.1 Depletion definition and method of measurement

With the assumption that the pumping speed of silane, $S_{\mathrm{SiH_4}}$, and argon, S_{Ar}, is much higher than for hydrogen, $S_{\mathrm{H_2}} \ll S_{\mathrm{SiH_4}} \simeq S_{\mathrm{Ar}}$, the partial silane and argon pressure will always be much less than the partial hydrogen pressure and the total pressure is given as

$$p = p_{\mathrm{Ar}} + p_{\mathrm{SiH_4}} + p_{\mathrm{H_2}} \simeq p_{\mathrm{H_2}}.$$

The silane depletion is defined in terms of the fraction of silane flow which is dissociated and not lost to the pumps. The conservation of silane leads to

$$\Phi^{\mathrm{in}}_{\mathrm{SiH_4}} = (kn_{\mathrm{e}} + S_{\mathrm{SiH_4}})p_{\mathrm{SiH_4}},$$

where $\Phi^{\mathrm{in}}_{\mathrm{SiH_4}}$ is the input flowrate, $S_{\mathrm{SiH_4}}p_{\mathrm{SiH_4}} = \Phi^{\mathrm{pump}}_{\mathrm{SiH_4}}$ is the pump loss rate and $kn_{\mathrm{e}}p_{\mathrm{SiH_4}} = \Phi^{\mathrm{in}}_{\mathrm{SiH_4}} - \Phi^{\mathrm{pump}}_{\mathrm{SiH_4}} = \Phi^{\mathrm{diss}}_{\mathrm{SiH_4}}$ is the dissociation rate of silane. As no additional hydrogen is set to the reactor and two H_2 molecules are produced per totally dissociated SiH_4, the hydrogen conservation is defined as a balance between production rate and loss rate to the pumps:

$$2kn_{\mathrm{e}}p_{\mathrm{SiH_4}} = S_{\mathrm{H_2}}p_{\mathrm{H_2}} \quad \Leftrightarrow \quad \Phi_{\mathrm{H_2}} = 2\Phi^{\mathrm{diss}}_{\mathrm{SiH_4}},$$

where $\Phi_{\mathrm{H_2}}$ is the hydrogen production rate from the dissociated silane. When $\Phi_{\mathrm{H_2}} = 2\Phi^{\mathrm{in}}_{\mathrm{SiH_4}}$, all silane is totally depleted. The pressure curve corresponding to this case is the one measured in a pure hydrogen plasma (cf. figure 5.31b). The depletion can now be defined as the ratio between silane dissociation flowrate and total input flowrate:

$$D = \frac{\Phi^{\mathrm{diss}}_{\mathrm{SiH_4}}}{\Phi^{\mathrm{in}}_{\mathrm{SiH_4}}} \tag{5.3}$$

Figure 5.32 explains how to calculate the dissociation flow rate from the measured pressure curves for a given input flowrate. If $\Phi^{\mathrm{in}}_{\mathrm{SiH_4}}$ gives pressure p (1), then the same pressure on the total depletion curve (2) gives $\Phi^{\mathrm{diss}}_{\mathrm{SiH_4}}$ (3), the equivalent totally depleted silane flux.

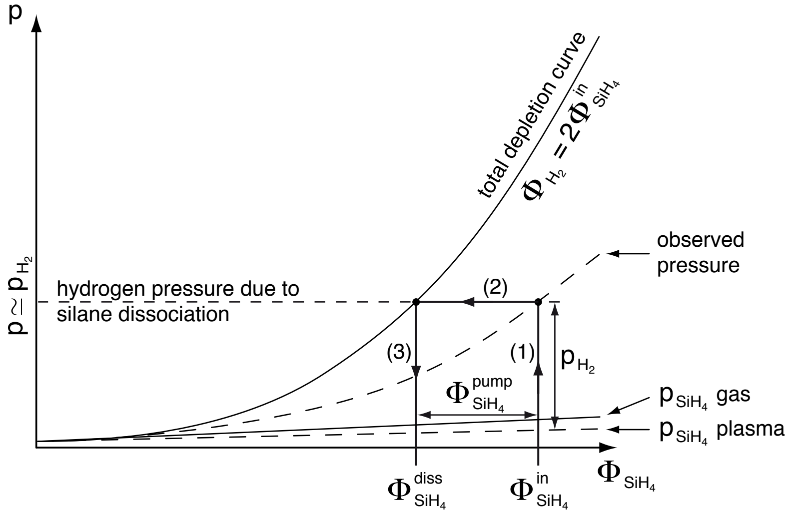

Figure 5.32: Method for the depletion calculation. $\Phi^{\mathrm{in}}_{\mathrm{SiH_4}}$ is the given silane flux into the reactor, $\Phi^{\mathrm{diss}}_{\mathrm{SiH_4}}$ is the equivalent totally depleted silane flux leading to the same pressure.

A comparison of the depletion definition in equation 5.3 with the depletion definition used for large area RF reactors shows the principle difference between these two. For RF plasmas the higher pressure and the use of displacement pumps, means that the silane and hydrogen mixture is pumped with a common convective flow speed. For this diffusive case the silane depletion is defined by the relative partial pressure of depleted $\mathrm{SiH_4}$ and is obtained by

$$D = \frac{p_{\mathrm{g}} - p_{\mathrm{pl}}}{p_{\mathrm{g}}},$$

where p_{pl} and p_{g} are the partial pressures of $\mathrm{SiH_4}$ with and without plasma respectively [59]. In order to find the partial silane pressures, FTIR or optical spectra of the plasma have to be measured, which can be very time-consuming.

In the case of the DC plasma the depletion is basically defined the same way, namely in terms of the fraction of dissociated silane. However, due to the dominance of the hydrogen pressure in this experimental situation, the simple pressure method can be used to estimate D. The relative partial pressure of silane could still be measured by FTIR, although high sensitivity would be required because of the low silane pressure, but the pressure method is very simple and convenient and can be rapidly achieved, even though it gives only an estimation of the depletion.

5.4.2 Depletion dependence on discharge current

The above described method of depletion estimation was used to analyse the dissociation efficiency of the plasma with increasing discharge current. In figure 5.33 the pressure measurements and their corresponding depletion calculations are shown. The measurements were made in the BAI reactor with original configuration (circular gas injection, no cage). For low silane fluxes the depletion is complete. The calculated value of more than 100 % is due to measurement uncertainty at these low pressures. With increasing silane flux the depletion decreases to about 75–80 % at 200 sccm and than stays nearly constant. Only in the case of a discharge current of 180 A the depletion shows again a slight increase. These depletion calculations show that for high silane fluxes about 20–25 % of the silane put into the reactor is directly pumped and thus is not used in deposition process. This gives a non-maximal efficiency, especially in the interesting cases of high silane fluxes, where the deposition rate is high enough to compete against other deposition systems. For a substantial increase of efficiency it is not useful to simply increase the power of the reactor. An increase of the discharge current of 50 % leads to an increase of depletion of only 10 %. Nevertheless it is possible to increase the dissociation efficiency. In the next section it is shown that a modification of the reactor geometry can lead to the goal by reducing the relative silane loss to the pumps.

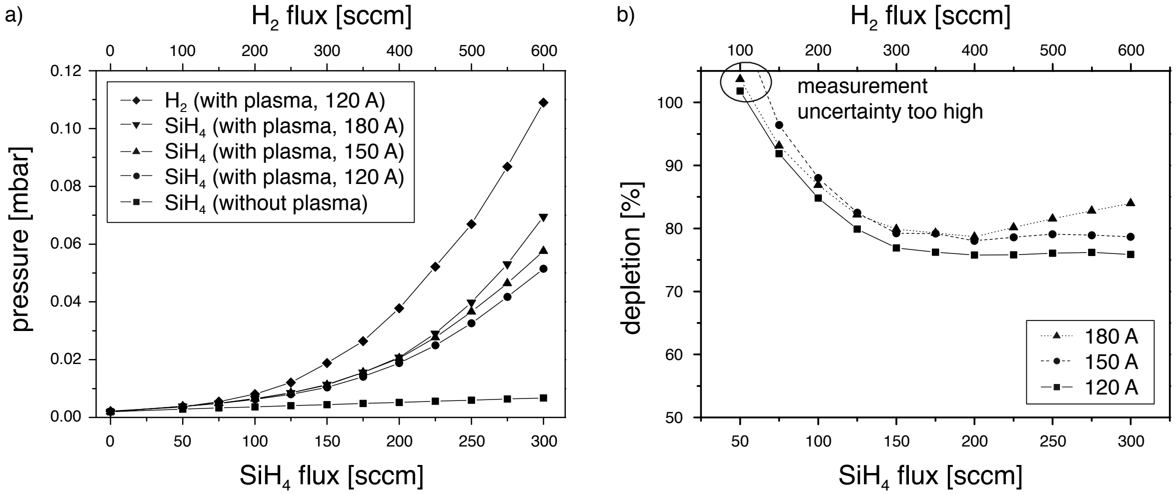

Figure 5.33: Pressure measurements (a) and depletion calculation (b) for three different plasma discharge currents with a circular gas injection. The pressure measurement uncertainty is about $\Delta p = 5 \cdot 10^{-4}$ mbar, the error bars are omitted for clarity.

5.4.3 Changes in dissociation efficiency

In section 5.2.1 the use of a linear gas injection was discussed. The vertical homogeneity of the growth rate was substantially increased, but the mean growth rate was constant or even lower than with the circular injection. In figure 5.34 the pressure measurements and depletion calculations made in a reactor with a linear gas injection are shown. The measurements show no important differences between the two types of gas injection, although the gas inflow is aligned towards the plasma column. This is in good agreement with the constant mean growth rate, the linear injection does not change the dissociation efficiency of the reactor.

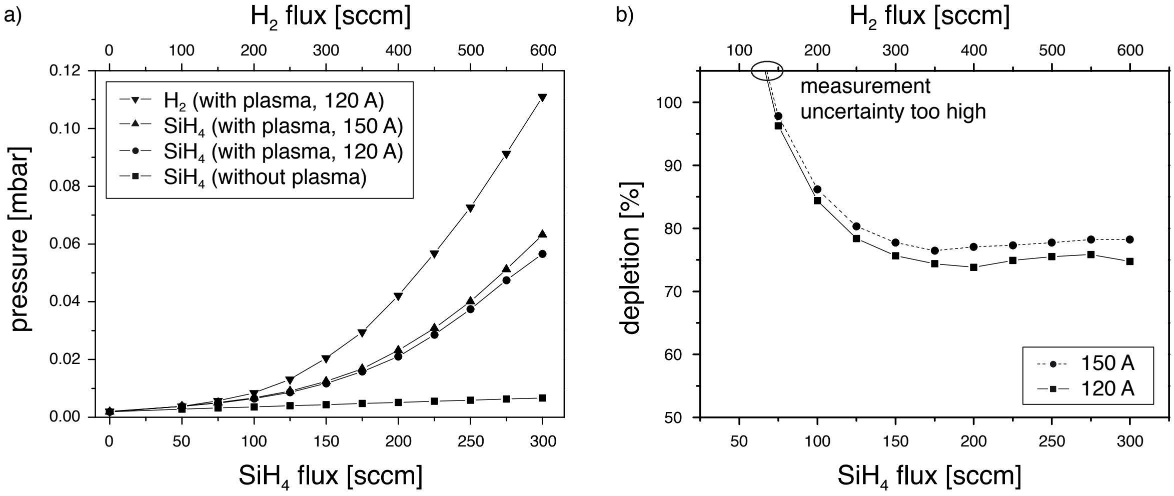

Figure 5.34: Pressure measurements (a) and depletion calculation (b) for three different plasma discharge currents using a linear gas injection.

In section 5.3 a second modification of the BAI reactor was presented: the installation of a volume limiting cage. The hydrogen pressure measurements in this third configuration showed an important difference to the measurements presented before. In figure 5.35 the effect of the cage on the pressure and thus on depletion is shown. The depletion still is complete for low silane fluxes but drops only to about 92 % for silane fluxes higher than 150 sccm. This strong gain in dissociation seems to be contradicted by the comparison of maximum growth rate on large size glasses in the cage (cf. figure 5.29) and on small samples used for vertical homogeneity studies (cf. figure 5.9), both indicating a growth rate maximum of 6.5 nm/s with $\phi_{SiH_4} = 200$ sccm. This discrepancy can be explained by the fact, that the small samples act like sinks, attracting the silane radicals for deposition. Therefore the deposition rate is overestimated when using only some small samples for deposition.

It turns out that this simple pressure measurement is a strong tool to analyse the depletion efficiency of different reactor configurations. The measurements are easily made in short time and give a rough but meaningful indication on the utility of a certain configuration change.

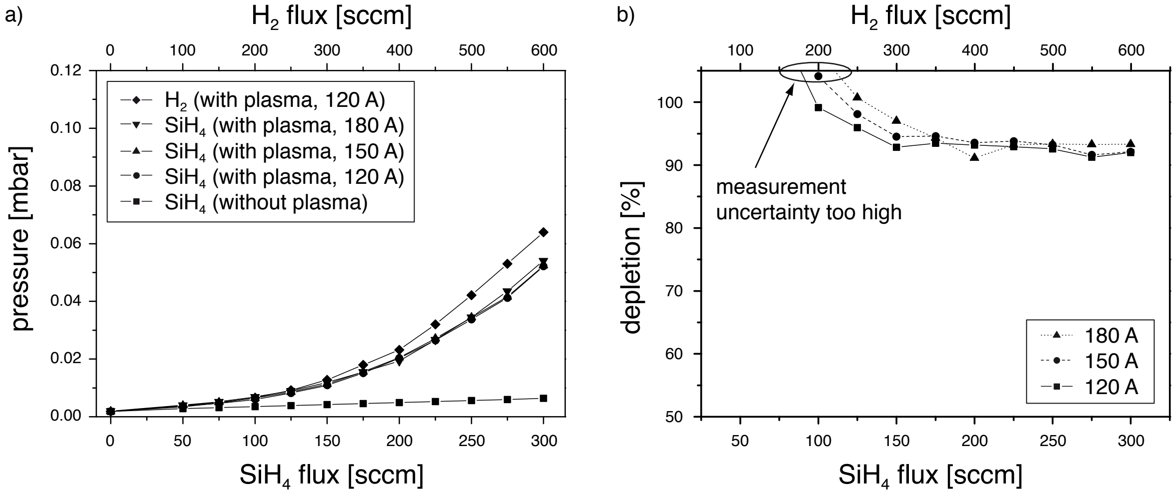

Figure 5.35: Pressure measurements (a) and depletion calculation (b) for three different plasma discharge currents using a linear gas injection together with the confining cage.

5.5 Conclusion

The deposition process of silicon carbide films on silicon wafers were studied, showing growth rates up to 9 nm/s, with an increasing tendency for increasing silane flux and a decreasing tendency for increasing methane flux. The SiC films showed high impurity concentrations of hydrogen and oxygen, making the films inappropriate for the use of hard covers.

For solar cell applications nc-Si:H films deposited on silicon wafers and glass substrates were analysed in detail. For a homogeneity increase of the deposition rate along the plasma column, a new linear gas injection was designed and constructed. The maximum deposition rate found with 200 sccm of silane influx was 6.5 nm/s. An analysis of other system parameters showed a strong dependence of the growth rate on the applied magnetic field but very little on the applied discharge current. With Micro-Raman spectroscopy the crystallinity of the silicon films was measured, showing that it is possible to use the BAI reactor for the deposition of amorphous and nanocrystalline silicon films with crystallinity up to 80 %. The crystalline structure of the nc-Si:H films is found to be porous, seen on SEM images of the films. This leads to high oxygen concentration, either deposited during the process in the non-UHV module or absorbed when exposed to the air. An amorphous caping was used to reduce the absorption effect, but not solving the porosity problem.

Silicon depositions on large size glasses ($37 \times 47\,\mathrm{cm}^2$) showed a diffusive effect along the plasma column, leading to an inhomogenious growth rate. By using a numerical diffusion model a solution to this was found: by reducing the dead volume in the reactor and approaching the glass substrate to the plasma column, the diffusive effect can be minimised. Therefore a steel cage was constructed, acting as substrate holder and reducing the volume of the cylindrical reactor.

For an estimation of the plasma efficiency in dissociating the silane gas, a simple pressure measurement method was developed. As the turbo pump has very different pumping rates for light hydrogen molecules and other particles, the pressure in the reactor is mainly dominated by the hydrogen produced in the dissociation of silane molecules. By comparing the pressure of a silane plasma with the pressure of a pure hydrogen plasma, the flux of dissociated silane $\Phi_{\mathrm{SiH_4}}^{\mathrm{diss}}$ can be found. The depletion is then defined as the ratio of dissociated silane to the total silane influx. With this method the plasma efficiency in three different reactor configurations was estimated, showing a remarkable increase of efficiency from 75 % to 92 % with the volume limiting cage.

Final conclusions and outlook

In the framework of this thesis the properties and the potential use of a high current DC arc plasma source for silicon and silicon carbide film deposition were investigated. The search for an optimal deposition process brought up several fundamental changes in the geometry of both reactors used for this thesis, the LEP and the BAI reactor.

A multi-Langmuir probe was used in the LEP reactor configuration, where a circular anode is used, to measure the ion density at the substrate position. These measurements were repeated for different plasma parameters, such as gas pressure and external magnetic field, in order to find the influence of these parameters on film thickness homogeneity. Furthermore a dynamic wobbling magnetic field, produced by four solenoids, and also a static cusp field, produced by strong permanent magnets fixed around the reactor vessel have been investigated to increase the homogeneity of the film thickness.

Optical plasma observations showed different types of instabilities: a) weak and strong flickering, b) plasmas attaching to one or several points on the circular anode, appearing as a bright glow, or c) plasmas jumping irregularly between these current attachment points. Therefore a detailed instability and non-uniformity characterisation of the plasma was made by using several types of probes. The instability of 50 Hz and its harmonics was found to be induced by the AC heating current in the filament, whereas a subharmonic instability was related to the observed flickering induced by the circular anode. Furthermore a novel type of probe was developed, based on a Hall sensor, to measure the magnetic field induced by the discharge current. By comparing magnetic field measurements with a 2D model of the current density distribution in the reactor, the bright glowing plasma attachment spots were shown to correlate directly with the path the discharge current takes. The installation of a cusp field did not solve the problem that the current preferably attaches to certain points on the circular anode. As a conclusion the circular anode arranged in the LEP reactor has been abandoned in favour of a conical point anode, and also a stronger external magnetic field of 45 G instead of 5.4 G, produced by larger Helmholtz coils, has been installed. This brought the LEP reactor back to the geometry already used in a previous version of the BAI reactor.

A multi-Hall probe was used to measure the current density distribution inside the columnar plasma, created in the modified reactor. These measurements showed a strongly peaked current density profile at an external magnetic field of 45 G. Fitting the profile with a Gaussian distribution showed that the total current of 70 A passes along the plasma column on the central axis of the reactor. With the external magnetic field switched off, the current density profile gets wider, as the plasma loses completely its columnar shape, and it was found that 22 A of the 70 A current passed elsewhere than in the discharge column. No perturbation of the multi-Hall probe onto the plasma has been found. Finally the measured current density profiles were also used, together with ion saturation current density measurements from a Langmuir probe, to estimate the electron temperature to be about 4 eV inside the plasma column.

Optical emission spectroscopy (OES) was applied to study the argon-silane plasma used in the BAI reactor for silicon deposition. The intensity spectra are strongly dominated by lines of silicon and argon ions as well as by excited hydrogen atoms. This proves that the HCDCA plasma operated in the low pressure regime has a much higher dissociation rate compared to large area RF plasmas. Furthermore, depending on pressure and discharge current, the OES measurements were used to show differences in the electron thermalisation. In a plasma with $I_{\mathrm{pl}} = 120\,\mathrm{A}$ and $\phi_{\mathrm{SiH_4}} = 100\,\mathrm{sccm}$ the primary electrons are not thermalised with the background low energy electron population. However, if the discharge current is reduced to 40 A or if the silane flux is increased to 200 sccm, leading to a pressure increase by a factor of four, the primary electrons are completely thermalised. This indicates that, depending on the applied discharge current and the gas pressure in the reactor, the primary electrons thermalise at variable position in the plasma column.

Finally, the potential of the HCDCA plasma source for two different applications was investigated: 1) The deposition of silicon carbide (SiC) films and 2) the production of nanocrystalline silicon (nc-Si:H) films for solar cell applications. In situ reflectometry was used for the measurement of the SiC film growth rates, reaching up to 9 nm/s. FTIR analysis of the deposited SiC films unveiled high impurity concentrations of oxygen and hydrogen, making the films inappropriate without further optimisation to be used as hard layers. A more detailed analysis was done for the nanocrystalline silicon films. Ex situ growth rate measurements with an alpha-step system showed two sources for inhomogeneity of the film thickness: 1) The process gas injection and 2) the geometry of the reactor itself. By installing a linear gas injection a first improvement in the film homogeneity along the plasma column was achieved. A numerical gas diffusion model showed that it is necessary to reduce the reactor volume and to approach the substrate to the plasma column in order to minimise diffusive effects along the column. Growth rate measurements on large surface glass substrates, deposited before and after the installation of a volume-reducing cage, were used to prove the model predictions. Micro-Raman spectroscopy was used to measure the crystallinity of the deposited films, showing that with this type of plasma it is possible to deposit amorphous and nanocrystalline silicon with a crystallinity up to 80 %.

A simple method based on pressure measurements was developed in order to analyse the dissociation efficiency of the plasma in various configurations of the reactor. The basic principle of this measurement bases on the low pumping rate of the turbo pump for light hydrogen molecules, compared to the pumping rate of other particles. Therefore the gas pressure in the reactor is dominated by the hydrogen produced during the dissociation of silane molecules. A comparison between the gas pressure of a silane plasma and the gas pressure of a pure hydrogen plasma gives the flux of dissociated silane. The depletion is then defined as the ratio of dissociated silane to the total silane influx. With this simple method it was shown that the depletion increased from 75 % to 92 % when using the volume-reducing cage.

This work has shown that at present only a few rules exist for the design of a new deposition system, but no ready-to-use plasma reactor design can be found in textbooks on the subject of plasma physics. Because of the wide variety of plasma source types and applications each reactor has to be designed on a case-by-case basis. This makes the implementation of plasmas for industrial applications difficult. In the process of reactor optimisation in order to meet industrial demands, the geometry of the reactor was shown to be important. Examples presented in this work are the stability problems with the circular anode and the diffusive effects in the deposition process. The studies performed were useful to establish simple plasma diagnostics and some general designing rules for the shape of the anode, the gas injection and the reactor for a HCDCA plasma.

Bibliography

[1] T. Delachaux, *Etude d'un procédé de nitruration de la zircone tétragonale massive assisté par un plasma à arc à haut courant continu*, Ph.D. thesis, Ecole Polytechnique Fédérale de Lausanne (2003)

[2] I. Langmuir, *Oscillations in ionized gas*, Physics **14** 627–637 (1928)

[3] G. L. Rogoff, *Special Issue on Applications of Partially Ionized Plasmas*, IEEE Trans. Plasma Sci. **19** 989–990 (1991)

[4] B. Strahm, *Investigation of radio-frequency, capacitively coupled large area industrial reactor: cost-effective production of thin film microcrystalline silicon for solar cells*, Ph.D. thesis, Ecole Polytechnique Fédérale de Lausanne (2007)

[5] M. Gindrat, *Characterization of supersonic low pressure plasma jets*, Ph.D. thesis, Ecole Polytechnique Fédérale de Lausanne (2004)

[6] A. Descoeudres, *Characterization of electrical discharge machining plasmas*, Ph.D. thesis, Ecole Polytechnique Fédérale de Lausanne (2006)

[7] K. A. Polzin et al., *Thrust stand for electric propulsion performance evaluation*, Rev. Sci. Instrum. **77** 105108–1–9 (2006)

[8] J.-S. Chang, *Recent development of plasma pollution control technology: a critical review*, Sci. Technol. Adv. Mater. **2** 571–576 (2001)

[9] M. Pedrazzini, *Investigations of high current density arc plasmas for diamond deposition*, Ph.D. thesis, Ecole Polytechnique Fédérale de Lausanne (1996)

[10] D. Franz, *Déposition assistée par un plasma à arc à haut courant continu de couche minces de Nitrure de Bore et de Silicium microcristallin hydrogéné*, Ph.D. thesis, École Polytechnique Fédérale de Lausanne, CRPP, PPB, CH-1015 Lausanne (1999)

[11] C. Rosenblad et al., *Silicon epitaxy by low-energy plasma enhanced chemical vapor deposition*, J. Vac. Sci. Technol. A **16** (5) 2785–2790 (1998)

[12] H. M. Buschbeck et al., *Production-ready dry cleaning and deposition processes for low-temperature Si and SiGe epitaxy*, Appl. Surface sci. **224** (1-4) 36–40 (2004)

[13] C. Rosenblad et al., *Low-temperature heteroepitaxy by LEPECVD*, Thin Solid Films **318** (1-2) 11–14 (1998)

[14] C. Rosenblad et al., *Epitaxial growth at high rates with LEPECVD*, Thin Solid Films **336** (1-2) 89–91 (1998)

[15] C. Rosenblad et al., *Low temperature epitaxial growth by LEPECVD*, J. Cryst. Growth **188** (1-4) 125–130 (1998)

[16] M. A. Liebermann and A. J. Lichtenberg, *Principles of Plasma Discharges and Materials Processing*, John Wiley & Sons, Inc., pp. 154–190, 2nd edition edition (1994)

[17] I. H. Hutchinson, *Current density measurement in Tokamak-type devices by longitudinal Thompson scattering: a proposal*, J. Phys. D: Appl. Phys. **10** L11–L16 (1977)

[18] F. A. Karelse et al., *Current density measurements with tangential Thomson scattering in plasmas with peaked and hollow temperature profiles*, in *25th EPS Conf. on Controlled Fusion and Plasma Phys.*, European Physical Society (1998)

[19] G. A. Collins et al., *Central mass and current density measurement in tokamaks using the discrete Alfvén spectrum*, Plasma Phys. Control. Fusion **29** (3) 232–239 (1987)

[20] H. Soltwisch, *Current distribution measurement in a tokamak by FIR polarimetry*, Rev. Sci. Instrum. **57** (8) 1939–1944 (1986)

[21] A. J. H. Donné, *Diagnostics for current density and radial electric field measurements: overview and recent trends*, Plasma Phys. Control. Fusion **44** B137–B158 (2002)

[22] V. Korepanov and F. Dudkin, *Comparative analysis of current density meters operating in space plasmas*, Adv. Space Res. **23** (8) 1541–1544 (1999)

[23] Sentron AG, 6300 Zug - Switzerland, *CSA-1V - Current sensor* (2004)

[24] M. A. Green and M. J. Keevers, *Optical properties of intrinsic silicon at 300 K*, Prog. Photovoltaics: Res. & Appl. **3** (3) 189–192 (1995)

[25] H. Scheer et al., editors, *Nanotextured thin film silicon solar cells: optical model*, 16th European Photovoltaic Solar Energy Conference, Glasgow, UK (2000)

[26] G. Hass, M. Francombe and J. Eastman, *Physics of Thin Films, Advances in Research and Development*, Academic Press, New York, volume 10, pp. 167–226 (1978)

[27] D. A. G. Bruggemann, *Berechnung verschiedener physikalischer Konstanten von heterogenen Substanzen. I. Dielektrizitätskonstanten und Leitfähigkeiten der Mischkörper aus isotropen Substanzen*, Annalen der Physik **146** (7) 636–664 (1935)

[28] R. McCreery, *Chemical Analysis*, in *Raman spectroscopy for chemical analysis*, Wiley, volume 157 (2000)

[29] C. Droz et al., *Relationship between Raman crystallinity and open-circuit voltage in microcrystalline silicon solar cells*, Sol. Energy Mater. Sol. Cells **81** 61–71 (2004)

[30] S. Mukhopadhyay, C. Das and S. Ray, *Structural analysis of undoped microcrystalline silicon thin films deposited by PECVD technique*, J. Phys. D: Appl. Phys. **37** 1736–1741 (2004)

[31] P. A. Miller and K. E. Greenberg, *Period-doubling bifurcation in a plasma reactor*, Appl. Phys. Lett. **60** (23) 2859–2861 (1992)

[32] N. Hayashi and Y. Kawai, *Observation of bifurcation phenomena in an electron beam plasma system*, Phys. Plasmas **3** (12) 4440–4445 (1996)

[33] T. Mausbach, T. Klinger and A. Piel, *Chaos and chaos control in a strongly driven thermionic plasma diode*, Phys. Plasmas **6** (10) 3817–23 (1999)

[34] H. Takekida and K. Nanbu, *Particle modelling of plasma confinement by a multipolar magnetic field*, J. Phys. D: Appl. Phys. **37** 1800–1808 (2004)

[35] P. Raizer, Yuri, *Gas Discharge Physics*, Springer Verlag (1991)

[36] M. Chesaux, *Deposition de silicium microcristallin par plasma DC a haut courant d'arc*, Master's thesis, Ecole Polytechnique Fédérale de Lausanne (2007)

[37] A. G. Gaydon and R. W. B. Pearse, *The identification of molecular spectra*, John Wiley & Sons, Inc. (1950)

[38] J. Reader et al., *Wavelengths and Transition Probabilities for Atoms and atomic Ions*, U.S. Departement of Commerce/National Bureau of Standards (1980)

[39] D. Tamburrino, *Etude par spectroscopie d'émission optique de l'écoulement supersonique d'un jet de plasma issu d'une torche DC opérée à basse pression*, Master's thesis, EPFL (2003)

[40] A. K. Costa et al., *Characterization of ultra-hard silicon carbide coatings deposited by RF magnetron sputtering*, Thin Solid Films **377-378** 243–248 (2000)

[41] F. Liao et al., *High-rate chemical vapor deposition of nanocrystalline silicon carbide films by radio frequency thermal plasma*, Mater. Lett. **57** 1982–1986 (2003)

[42] G. Leggieri et al., *Laser reactive ablation deposition of silicon carbide films*, Appl. Surface sci. **69-98** 866–869 (1996)

[43] N. Rajan et al., *Fabrication and Testing of Micromachined Silicon Carbide and Nickel Fuel Atomizers for Gas Turbine Engines*, Microelectromechanical Systems, Journal of **8** (3) 251–257 (1999)

[44] O. Leroy et al., *Two-dimensional modelling of SiH_4-H_2 radio-frequency discharges for a-Si:H deposition*, Plasma Sources Sci. Technol. **7** 348–358 (1998)

[45] P. Kae-Nune et al., *Mass spectrometry detection of radicals in* SiH_4*-*CH_4*-*H_2 *glow discharge plasmas*, Plasma Sources Sci. Technol. **4** 250–259 (1995)

[46] H. Kojima, H. Toyoda and H. Sugai, *Observation of* CH_2 *radical and comparison with* CH_3 *radical in a RF methane discharge*, Appl. Phys. Lett. **55** (13) 1292–1294 (1989)

[47] K. Yamamoto et al., *A high efficiency thin film silicon solar cell and module*, Solar Energy **77** 939–949 (2004)

[48] C. Wronski, D. Carlson and R. Daniel, *Schottky-barrier characteristics of metal-amorphous-silicon diodes*, Appl. Phys. Lett. **29** 602–605 (1976)

[49] A. Matsuda, *Microcrystalline silicon. Growth and device application*, J. Non-Cryst. Solids **338-340** 1–12 (2004)

[50] A. Shah et al., *Microcrystalline silicon and 'micromorph' tandem solar cells*, Thin Solid Films **403-404** 179–187 (2002)

[51] R. W. Miles, G. Zoppi and I. Forbes, *Inorganic photovoltaic cells*, Materials Today **10** (11) 20–27 (2007)

[52] G. Beaucarne et al., *Epitaxial thin-film Si solar cells*, Thin Solid Films **511-512** 533–542 (2006)

[53] Y. Nakano et al., *High-deposition-rate of microcrystalline silicon solar cell by using VHF PECVD*, Thin Solid Films **506-507** 33–7 (2006)

[54] A. H. M. Smets, T. Matsui and M. Kondo, *Infrared analysis of the bulk silicon-hydrogen bonds as an optimization tool for high-rate deposition of microcrystalline silicon solar cells*, Appl. Phys. Lett. **92** 033506 (2008)

[55] M. Vanecek and A. Poruba, *Fourier-transform photocurrent spectroscopy of microcrystalline silicon for solar cells*, Appl. Phys. Lett. **80** (5) 719–721 (2002)

[56] O. Vetterl et al., *Intrinsic microcrystalline silicon: A new material for photovoltaics*, Sol. Energy Mater. Sol. Cells **62** 97–108 (2000)

[57] D. Franz et al., *Rapid deposition of hydrogenated microcrystalline silicon by a high current DC discharge*, Thin Solid Films **383** (1-2) 11–14 (2001)

[58] C. Hollenstein et al., *Silicon oxide particle formation in RF plasmas investigated by infrared absorption spectroscopy and mass spectrometry*, J. Phys. D: Appl. Phys. **31** 74–84 (1998)

[59] B. Strahm et al., *Plasma silane concentration as a determining factor for the transition from amorphous to microcrystalline silicon in* SiH_4/H_2 *discharges*, Plasma Sources Sci. Technol. **16** 80–89 (2007)

Aknowledgement

Just before the end of this thesis maybe the most pleasant part for me to write. This work was supported by a lot of people in many different ways and now it's the time for me to thank them all. For this I will now switch to French and later on to German.

Tout d'abord j'aimerais remercier Christoph, mon directeur de thèse et chef du groupe des plasmas industriels. Merci de m'avoir accueilli dans ton groupe depuis mon premier TP jusqu'à ces quatre années inoubliables de thèse. Merci aussi pour la confiance que tu m'a témoignée pendant ce projet, même après deux inondations du labo et un oscilloscope grillé.

Merci aussi aux membres de mon jury de thèse, les Professeurs Robert Schaller, Jörg Winter et Philipp Rudolf von Rohr et le Dr. Ulli Kroll, pour leur temps consacré à juger mon travail.

Je tiens à remercier tous les autres membres actuels et passés du groupe des plasmas industriels, et particulièrement Alan qui était toujours attentif à mes problèmes tout au long de ce projet et qui a accepté de faire une première correction de ce manuscrit. Merci aussi à Jean-Luc et Laurent pour leur support technique et théorique, respectivement. Je remercie Thierry pour son introduction à la "Grossmutti" et Michaël pour sa contribution au chapitre consacré à la spectroscopie optique. Merci spécialement aux doctorants actuels et passés, notamment à Ben pour les nombreuses discussions stimulant, au labo, à Sat ou au diable vauvert (salutations de Bonatchiesse), et à Boris et Marina pour leur aide dans mes premiers pas en italien, grazie mille, et enfin à Samantha pour son soutien moral au moment du sprint final.

Comme ce travail était aussi un défi technique du début jusqu'à la fin, je tiens aussi à remercier les personnes des différents ateliers, notamment Roger et Roby qui ont fait parfois un boulot magique avec leurs fraises et autres outils, Christian et Gilbert qui ont du réanimer plusieurs fois la "Grossmutti", Christian, le chef des tuyaux et de la soudure, et enfin le groupe des électroniciens pour la construction de ma multi-sonde de Hall. Merci aussi à Pierre qui m'a résolu (presque) tous les problèmes informatiques, et aux secrétaires pour leur support administratif.

En dehors du CRPP j'ai aussi été soutenu par les différents groupes de Unaxis/Oerlikon. Je tiens tout particulièrement à remercier le Dr. Matthias Kummer et son équipe de Trübbach pour leurs nombreux conseils dans la résolution du puzzle que constituait le LEP désassemblé, le Dr. Stéphane Bourdais et son équipe de Montbonnot près de Grenoble pour l'accueil chaleureux dans leurs labos, et enfin le Dr. Jochen Hötzel pour son enthousiasme quant à ce projet.

Nun noch der Wechsel ins deutsche für die Familie und all meine deutschschweizer

Kollegen. Einen Dank zuerst an die Vario-Gang für all die gemütlichen Stunden in Olten. Speziell die Sonntagabende waren immer wieder eine Quelle der Motivation. Ebenfalls danken möchte ich all meinen bis heute insgesamt zwölf Mitbewohnern in Lausanne und St-Sulpice für all die Küchenschlachten, Fernsehabende, Salatpartys und Erlebnisse in den Walliser Alpen, trotz Reifenpanne. Die Zeit in Lausanne wird mir, insbesondere dank euch, immer in bester Erinnerung bleiben.

Einen Dank richte ich an Ursi und Claude für ihre unzähligen Einladungen zum Nachtessen im schönen Jongny. Ich fühlte mich während meines nun über zehn Jahre dauernden Aufenthalts in der Romandie immer willkommen bei euch und verspreche der Westschweiz nicht ganz den Rücken zu kehren.

Zum Abschluss möchte ich meinen grössten Dank an meine Familie richten, meine Eltern Renata und Franz, meine Schwester Anna und mein Bruder Benjamin. Ihr habt es mir erst möglich gemacht dieses "Experiment Westschweiz" zu erleben. Ich spürte immer euren Halt, wenn ich an den Wochenenden oder in letzter Zeit, Politik sei dank, auch mal unter der Woche in Olten vorbeigeschaut habe.

Curriculum Vitae

Lukas DERENDINGER

Originaire de Lüterkofen (SO)
Né le 15 janvier 1978 à Baden (AG)

FORMATION

1985 - 1993	**Ecole primaire et secondaire** à Olten (SO)
1993 - 1998	**Maturité ès sciences** et **certificat de maturité-type C** Kantonsschule Olten, Olten (SO)
1998 - 2004	Ecole Polytechnique Fédérale de Lausanne **Diplôme d'ingénieur physicien** Travail de diplôme effectué au Centre de Recherches en Physique des Plasmas (CRPP)
2004 - 2008	Ecole Polytechnique Fédérale de Lausanne **Assistant-doctorant** dans le groupe des plasmas industriels au Centre de Recherches en Physique des Plasmas (CRPP) Encadrement d'un travail de diplôme (2006-2007) Assistant de Travaux Pratiques IV (2007)